AALBORG UNIVERSITY

Design of Slip-based Active Braking and Traction Control System for the Electric Vehicle QBEAK

Board of Studies of Energy

Title:	Design of Slip-based Active Braking and Traction Control System for the Electric Vehicle QBEAK
Semester:	10
Semester theme:	Master's Thesis
Project period:	01.02.12 to 14.06.12
ECTS:	30
Supervisor:	Hans-Christian Becker Jensen
Project group:	MCE4-1024

Mads Hellegaard Andersen

Rune Wiben

SYNOPSIS:

A slip control system is designed for the QBEAK electric vehicle developed by ECOmove ApS. The controller is based on a dynamic model describing the planar motion of the vehicle. An integral sliding mode control structure is chosen to ensure robustness to changes in vehicle parameters, drag and rolling resistance and road surface conditions. Through simulations it is shown that the control system effectively reduces vehicle braking distance, increases traction and improves maneuverability. The system is furthermore tested experimentally. Oscillatory slip responses are observed in the tests due to a 240 $[ms]$ delay in the data communication of the test setup.
It is concluded that the communication delay must be reduced to ensure satisfactory closed-loop dynamics. The simulation results however conclude that the slip control system can improve acceleration and braking performance of the QBEAK vehicle.

Copies:	5
Pages, total:	157
Appendix:	45
Supplements:	CD

By signing this document, each member of the group confirms that all participated in the project work and thereby all members are collectively liable for the content of the report.

Preface

This report is part of the master's thesis project by the group MCE4-1024 at the Institute of Technology, Aalborg University. The project is developed in collaboration with ECOmove ApS and would not have been possible without the test setup and prototype vehicle supplied by this company. A special thanks is therefore given to the employees at ECOmove ApS for their help and guidance during the entire project.

Summary

The Danish company ECOmove ApS is currently developing the concept electric vehicle QBEAK. This project is concerned with the design of an active braking and traction control system for this vehicle.

The main forces responsible for braking, accelerating and maneuvering a vehicle are developed at the contact point between the tires and the road as a result of the difference in vehicle velocity and tangential wheel velocities. The normalized difference in vehicle and tire velocity is called slip and determines the magnitude of these tractive forces. The active braking and traction control system is therefore based on controlling the slip to maximize the tractive forces during braking and acceleration.

The slip control system is based on a dynamic model of the QBEAK vehicle and is designed to be robust to uncertainty in vehicle parameters and road conditions. An integral sliding mode control structure is chosen and a robust control law is derived guaranteeing exponential slip error convergence without the reaching phase normally encountered in sliding mode control.
The control law is modified by the addition of a boundary layer around the sliding surface in which the control gain is reduced. The implementation of the boundary layer effectively reduces the slip oscillations caused by the digital implementation of the controller. This is achieved at the expense of reduced guaranteed tracking accuracy of the system. The slip tracking error limits imposed by the addition of the boundary layer are 0.1 $[\cdot]$ at the front wheels and 0.06 $[\cdot]$ at the rear wheels.

An observer is designed to estimate the tractive friction forces affecting the vehicle and tires. The observer is based on sliding mode control theory and the estimated force is used in the slip controller to increase the robustness to unknown road conditions. The observer is tested in simulations and experiments.
The estimate of the friction force is also used to estimate the friction characteristics of the road surface during simulated driving using a recursive least squares algorithm. The estimated friction characteristics permits the calculation of an optimal slip reference to the controller.
Simulations indicate that the friction characteristics are very accurately estimated at constant road conditions. It is however concluded that estimation accuracy is insufficient for changing road conditions and a suboptimal constant slip reference is therefore used to increase the robustness of the controller.

The torque limitation of the electric driveline of the QBEAK vehicle is shown to cause actuator saturation when accelerating at high friction surfaces. An anti wind-up scheme is therefore developed as the control system involves integration of the slip error. The proposed anti wind-up algorithm involves switching between two sliding surfaces depending on whether the actuators saturate or not. Simulations indicate that the proposed algorithm significantly improves the performance of the slip controller in situations where actuator saturation occurs.

The electric driveline of the QBEAK vehicle permits the use of regenerative braking. The aforementioned torque limitations does however necessitate a hydraulic braking system in order to achieve sufficient braking torque needed in hard braking maneuvers. A torque distribution system is therefore designed to utilize the fast dynamics of the electric motors in combination with the high braking torque of the hydraulic brakes. Simulations show that improved dynamic response can be achieved by letting the electric motors act on the high frequency content of the desired braking torque which cannot be supplied by the hydraulic brakes. This is achieved without saturating the electric actuators.

The slip control system is tested through a series of simulations showing that the system is robust to variations in road condition, vehicle load, tire radius and rolling and drag resistance. Furthermore the system is shown to increase maneuverability and decrease the braking length in extreme driving conditions compared to an uncompensated system.

The slip control system is also tested experimentally on a single wheel test setup. The tests showed unacceptable slip responses which was shown to be caused by a 240 [ms] delay in the data communication. It is therefore concluded that this delay should be reduced to permit effective slip control. The simulation results however conclude that the slip control system can improve acceleration and braking performance of the QBEAK vehicle if the implementation issues can be resolved.

Abbreviations

ABS	Anti-Lock Braking System
BFF	Body Fixed Frame
BJT	Bipolar Junction Transistor
CoM	Center of Mass
DAQ	Data Acquisition
DoF	Degrees of Freedom
EC	European Commission
EEC	European Economic Community
EPP	Expanded Polypropylene
EV	Electric Vehicle
FWD	Front Wheel Drive
FWS	Front Wheel Steering
ICE	Internal Combustion Engine
4WD	4 Wheel Drive
IF	Inertial Frame
nLTO	nano Lithium Titanate
ODE	Ordinary Differential Equation
PMSM	Permanent Magnet Synchronous Machine
PDO	Process Data Object
RLS	Recursive Least Squares
RSW	Road Simulation Wheel
RWD	Rear Wheel Drive
SDO	Service Data Object
DVT	Shiroko Design Verification Test System
TCS	Traction Control System
UN	United Nations
WFF	Wheel Fixed Fram

Contents

1 Introduction

1.1 Electric Vehicles - The Competitive Alternative

The potential of electrically driven cars is currently being investigated by car manufacturers around the world [34], [13], [21], [8], [26], [25]. One of the reasons being the recent increase in oil prices [29] which motivates the need for a change to more economically beneficial - and environmentally friendly - alternatives. Today, Electric Vehicles (EVs) will travel longer than vehicles driven by an Internal Combustion Engine (ICE) for the same amount of money [23, p.48]. It travels longer as the electric motors are more efficient than the ICEs and the electricity required to drive a specific distance in an EV costs less than the amount of gasoline or diesel required to drive the same distance in a vehicle driven by an ICE [7].

Apart from economic benefits, recent legislative and regulatory actions[1] has favored the market for EVs and motivated the technological progress and competition in the field of EVs.

1.2 ECOmove ApS - QBEAK

Figure 1.1: The second QBEAK prototype.

The Danish company ECOmove ApS situated in Horsens is currently developing an electric vehicle called QBEAK (seen in figure 1.1). Two prototypes have been built so far and the third prototype is under construction. The QBEAK is a concept vehicle that distinguished itself from most of todays electric vehicles in several ways.

[1]Examples of legislative and regulatory actions are The European Union Regulation No 443/2009, which limits the CO_2 emission of a passenger car to 95 [g/km] from 2020 [27] and the Directive 2009/33/EC, stimulating the development of a market for clean and energy-efficient vehicles [28].

The design of the QBEAK is optimized to fit an electrical driveline as the design is not based on previously designed vehicles which is often the case when well established car manufacturers develop EVs. The design of the vehicle is therefore very different compared to other EVs on the market. An illustration of the chassis with driveline is seen in figure 1.2. The illustration shows that very little space is occupied by the driveline leaving a lot of free cabin space.

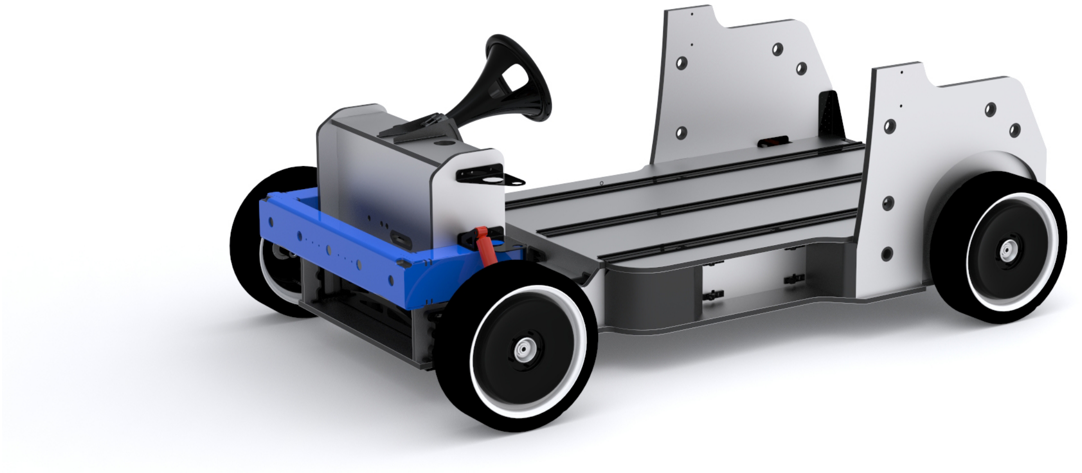

Figure 1.2: Illustration of QBEAK chassis and driveline.

The QBEAK is constructed using lightweight materials (aluminum and reinforced Expanded Polypropylene (EPP)). The vehicle mass is therefore extremely low compared to its passenger capacity. The mass of the unloaded vehicle is only 400 $[kg]$ while the cabin is able to fit six individual seats. The vehicle dimensions are:

- Length: 3 $[m]$
- Width: 1.75 $[m]$
- Height: 1.65 $[m]$

The QBEAK is driven by Permanent Magnet Synchronous Machines (PMSMs) mounted in the wheel suspension as illustrated in figure 1.3 and 1.4. The PMSMs can each deliver a torque of 13 $[N \cdot m]$ continuously and for short time loads a peak torque of up to 19.1 $[N \cdot m]$. The PMSMs drive the wheels through a fixed gear with gearing ratio $n = 10.3675$ and are powered by 80 $[V]$ nano Lithium Titanate (nLTO) batteries placed in a fireproof compartment in the bottom of the chassis. Depending on customers choice the car can be build with FWD, RWD or 4WD and with 1 to 6 battery modules corresponding to an approximate range of 50 to 300 $[km]$ respectively [17, p.2]. The nLTO batteries produced by Altair Nano can be fully recharged in less than 6 minutes [5] - a quality that distinguishes the QBEAK from other EVs.

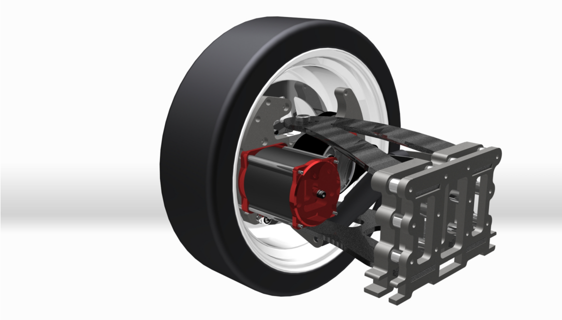

Figure 1.3: The front wheel suspension of the QBEAK vehicle.

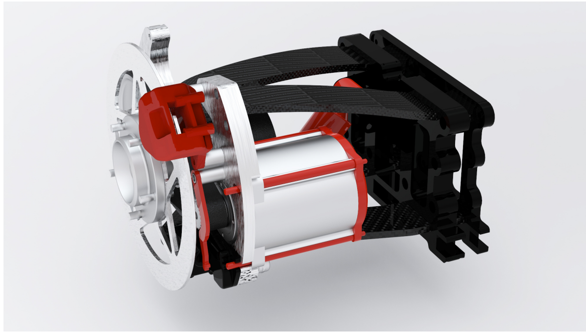

Figure 1.4: The stripped front wheel suspension of the QBEAK vehicle.

The PMSMs can be used as generators during braking to convert some of the kinetic energy of the vehicle into electrical energy in the batteries thereby extending the driving range. This is known as regenerative braking [40]. Besides the regenerative braking system the QBEAK is fitted with hydraulic disc brakes on each wheel (illustrated in figure 1.4) in order to supply sufficient braking torque required in emergency braking maneuvers.

The QBEAK is categorized as an M1-class vehicle [12] according to the EEC classification [4] and must comply with the safety requirements set by the UN/EEC and by the European Commission (EC). One of these requirements is that an Anti-lock Braking System (ABS) must be implemented [3]. ABS is a driver assistance systems designed to increase traction and maneuverability of the vehicle in severe braking situations by preventing the wheels from locking. This can significantly reduce the braking distance and ensure control of the lateral vehicle motion. A secondary function of many active braking systems is a Traction Control System (TCS) designed to prevent wheel spin during acceleration and driving on low friction road surfaces [36]. Again this increases the traction and aids the driver in maneuvering the vehicle.

1.3 ABS, TCS and Tire-Road Friction

The tractive forces responsible for accelerating and braking a vehicle is a result of friction between the road and the tires [15, p.5]. The friction occurs because the velocity of the road is slightly different from the tangential velocity of the wheels. However, if the difference in velocity is too large, some of the traction is lost and so is the ability to maneuver the vehicle sideways [35, ch.2], [22, ch.8]. The magnitude of the friction forces is a function of the normal force acting on the tire and the normalized velocity difference in the tire-road contact patch. This normalized velocity difference is called the *slip ratio* (or *slip*) λ_L and will be treated in detail in Section 2.5. The slip ratio can vary between -1 and 1 with a slip ratio of -1 corresponding to locked wheels, a slip ratio of 0 corresponding to pure rolling and a slip ratio of 1 corresponding to wheel spin. A sketch of a typical curve describing the longitudinal tire-road friction force as a function of slip ratio is seen in figure 1.5. Similarly the lateral friction force, which determines the maneuverability of the vehicle, is also a function of the slip ratio. A sketch of a typical curve of the lateral friction force is shown in figure 1.6. The friction curves will be treated in detail in Section 3.2.

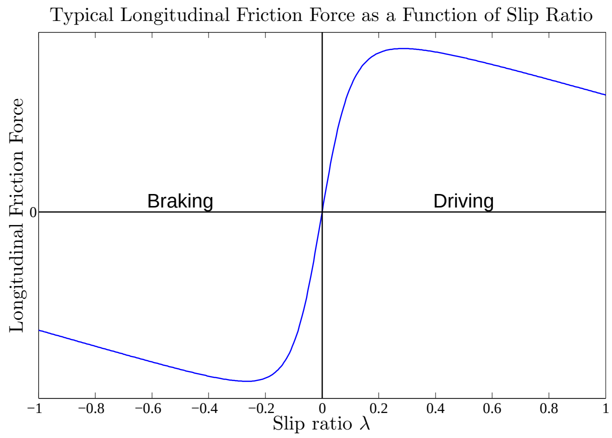

Figure 1.5: Sketch of a typical curve indicating longitudinal friction force as a function of slip ratio.

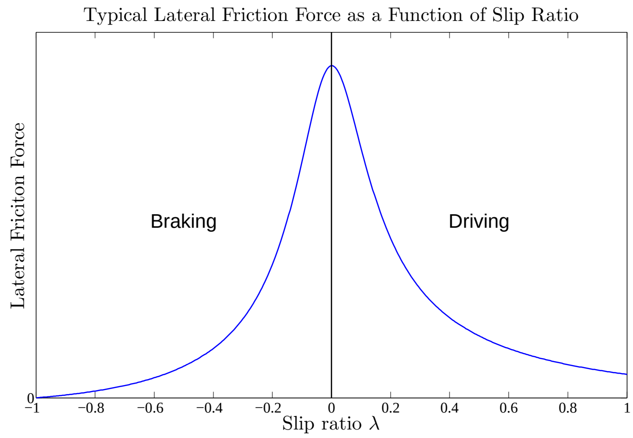

Figure 1.6: Sketch of a typical curve indicating lateral friction force as a function of slip ratio.

The curves plotted in figure 1.5 and 1.6 illustrates why ABS and TCS increase traction and maneuverability. It is seen that the magnitude of the longitudinal force peaks at relatively low magnitudes of slip ratio thus far from wheel spin or locked wheels. Equally important is it that the maneuverability (the lateral friction force) of the vehicle is significantly reduced during wheel spin and is complete lost if the wheels are locked. Preventing this from happening will therefore increase the driving safety.

Most commercially available ABS/TCS systems use the hydraulic brakes to prevent wheel spin and locked wheels by means of logic rule based algorithms [35, ch.1]. These algorithms typically react on the wheel acceleration rather than the slip ratio as this variable is easily measurable compared to the slip ratio which cannot be measured directly but must be estimated [35, ch.2]. However, recent development in the area of ABS and TCS has been focusing on slip ratio control, commonly referred to as *slip control* [35, ch.1], due to a range of desirable features over wheel acceleration control [35, p.60]:

- Slip control is more robust to changing and unknown road conditions compared to wheel acceleration control.
- Stability cannot be guaranteed for all slip values when using a fixed structure controller to control the wheel acceleration - even at a fixed road surface. The stability of the closed-loop system is dependent on the slope of the friction curve. Stability for all slip values can be guaranteed when using slip control.
- The open-loop dynamics of the wheel acceleration dynamics become non-minimum phase for slip values beyond the peak of the tractive force curve (figure 1.5). This limits the achievable closed-loop performance. Slip control does not suffer from this limitation.

Due to the advantages of slip control listed above it is desired to design the ABS and TCS based on slip control rather than conventional wheel acceleration control.

1.4 Braking and ABS Requirements

The Danish Transport Authority defines the technical requirements for road vehicles in Denmark. The directives are given in [39] and requires i.a. that road vehicles use functional brakes on all wheels and that the wheels do not lock during braking [39, p.50,pt.5.01.020-22]. The directives are based on regulations determined by UNECE.
The requirements for Braking and ABS are specified in "Regulation No 13-H - Uniform provisions concerning the approval of passenger cars with regard to braking" [1]. The paragraphs relevant to this project are listed below. All requirements are valid for braking on a high friction, straight and flat road.

- As stated in paragraph 5.1.2.1: *"The braking system of the vehicle must ensure driver maneuverability and stop the vehicle safely, effectively and rapidly at any speed, load and road gradient"*. This paragraph contains two main points; maneuverability during braking and safe, effective and rapid deceleration of the vehicle. In order to *"ensure driver maneuverability"* the wheels must be prevented from locking during braking - see figure 1.6. To *"safely, effectively and rapidly"* stop the vehicle the longitudinal friction force must be maximized when the driver desires hard braking.

- Paragraph 2.1 in appendix 3 states that the braking distance d_b of a passenger car on a high friction road surface must satisfy:

$$d_b \leq 0.1 \cdot v_i + 0.0060 \cdot v_i^2 \ [m] \tag{1.1}$$

  where v_i is the velocity of the vehicle (in $[{km}/{h}]$) as the braking maneuver is initiated. For $v_i = 100\ [{km}/{h}]$ the maximum braking length is thereby given as $d_{b,max} = 0.1 \cdot 100 + 0.0060 \cdot 100^2 = 70\ [m]$ on a high friction surface like dry asphalt.

The QBEAK vehicle must fulfill the braking requirements given above.

1.5 Initiating Problem Statement

The following initial problem statement outlines the scope of this project based on the previous sections.

A slip control system is to be designed for a FWD QBEAK vehicle. The system will be designed to utilize the maximum available friction between the tires and the road surface and ensure that:

- Maneuverability is not lost due to locked wheels during braking (ABS) or wheel spin during acceleration (TCS).
- Functionality is unaffected by different road conditions and vehicle loads.
- Stipulations regarding braking distance are met.

The control system will be designed on the basis of a mathematical model of the QBEAK vehicle. The model is derived from vehicle kinematics and vehicle dynamics and will be presented in the following sections.

Vehicle Kinematics 2

This chapter presents a kinematic model of the QBEAK vehicle that forms the basis for modeling of the vehicle dynamics. The kinematic model provides a mathematical description of the vehicle motion without considering the forces that affect the motion. These forces will be treated in Chapter 3

2.1 Coordinate Frames

A prerequisite for developing a mathematical model of the QBEAK vehicle is to define relevant coordinate frames [32]. In the following, three coordinate frames are defined: *The body fixed coordinate system*, *the inertial coordinate system* and *the wheel fixed coordinate system*.

The body fixed coordinate frame (BFF) has origin in the vehicle center of mass (CoM) , x^B-axis in the vehicle longitudinal direction, y^B-axis towards the left in the lateral direction of the vehicle and the z^B-axis completes the right hand rule pointing vertically upwards. Rotation around the x^B-, y^B- and z^B-axes is called roll φ, pitch θ and yaw ψ. The axes in the BFF are all marked with the superscript B. The coordinate system can be seen in figure 2.1.

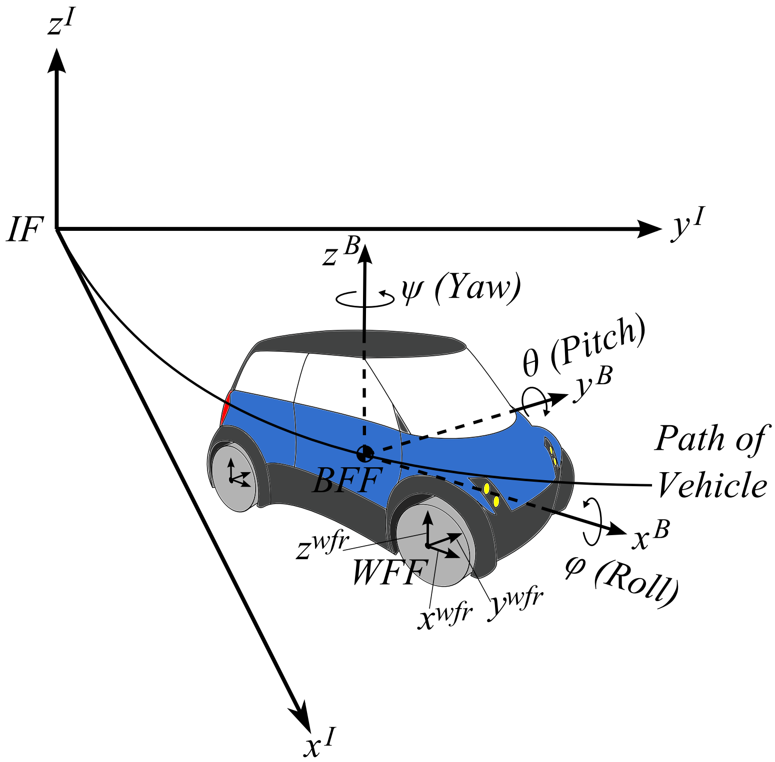

Figure 2.1: Turning vehicle in the inertial coordinate frame with body fixed- and a wheel fixed coordinate frame attached [16, p.583].

The wheel fixed coordinate frame (WFF) has origin in the center of each wheel. The y^w-axis coincides with the wheel axle and points in the direction of the y^B-axis if the vehicle is not turning. The z^w-axis points in the same direction as the z^B-axis. The x^w-axis completes the right hand rule. The coordinate frame rotates around the z^w-axis with the steering angle.
Since 4 WFF exists, the axes are each marked with the superscripts w for wheel, $i = \{f, r\}$ for front or rear position and $j = \{l, r\}$ for left or right side. The frame is shown on the vehicle of figure 2.1 and on the wheel of figure 2.4.

The inertial coordinate frame (IF) is a fixed frame, the origin can be placed freely but is usually defined so that it coincides with the body fixed frame when a vehicle maneuver - such as a turn - is initialized. The coordinate system is fixed and does not move or rotate. The fixed inertial coordinate system can also be seen in figure 2.1 - the axes are marked with the superscript I. The frame can be rotated to whatever initial angle makes the calculations simple - in the figure the x^I-, y^I- and z^I-axes are placed in the same direction as the BFF when the maneuver is initialized.

The three coordinate frames mentioned above will be used extensively throughout this report. It is of interest to transform the vehicle dynamics described in one coordinate frame to another coordinate frame. To do this the Euler angle rotation matrix is used. The matrix describes the rotational transformation from the BFF to the IF using a zxz-rotation sequence [32, p.22], [16, p.233]:

$$ {}^{I}\mathrm{R}_B = \begin{bmatrix} \cos(\varphi)\cos(\psi) - \cos(\theta)\sin(\varphi)\sin(\psi) & -\cos(\varphi)\sin(\psi) - \cos(\theta)\cos(\psi)\sin(\varphi) & \sin(\theta)\sin(\psi) \\ \cos(\psi)\sin(\varphi) + \cos(\theta)\cos(\varphi)\sin(\psi) & -\sin(\varphi)\sin(\psi) + \cos(\theta)\cos(\varphi)\cos(\psi) & -\cos(\varphi)\sin(\theta) \\ \sin(\theta)\sin(\psi) & \sin(\theta)\cos(\psi) & \cos(\theta) \end{bmatrix} \tag{2.1} $$

The opposite transformation from the IF to the BFF is found through the inverse of the matrix described in (2.1).

Under the assumption that the vehicle is a rigid body, moving in the xy-plane, and that the BFF is only revolving around the z-axis, the rotation matrix can be reduced to:

$$ \mathrm{R}_z = \begin{bmatrix} \cos(\psi) & -\sin(\psi) & 0 \\ \sin(\psi) & \cos(\psi) & 0 \\ 0 & 0 & 1 \end{bmatrix} \tag{2.2} $$

using that $\theta = 0$ and $\varphi = 0$.

Given the rotation matrix, the vehicle path can now be defined in the inertial coordinate frame.

2.1.1 Vehicle Path in Inertial Frame

When analyzing cornering maneuvers its useful to illustrate the vehicle path in the inertial frame. The path driven from an initial time t_i to a final time t can be obtained by integrating velocities in the IF with respect to time [16, p.594]. The velocities can be found by coordinate frame transformation from BFF to IF. If only planar motion is considered, then the velocity of the CoM in the BFF can be described as:

$$v^B = \begin{bmatrix} \dot{x} \\ \dot{y} \\ 0 \end{bmatrix} \tag{2.3}$$

The velocity can be transformed to the inertial frame using the Euler angle rotation matrix described in equation (2.2):

$$v^I = \mathrm{R}_z \cdot v^B = \begin{bmatrix} \dot{x} \cdot \cos(\psi) - \dot{y} \cdot \sin(\psi) \\ \dot{x} \cdot \sin(\psi) + \dot{y} \cdot \cos(\psi) \\ 0 \end{bmatrix} \tag{2.4}$$

The position of the vehicle in IF at time t is therefore [16, p.594]:

$$x^I(t) = x_0^I + \int_{t_i}^{t} (\dot{x} \cdot \cos(\psi) - \dot{y} \cdot \sin(\psi))dt \tag{2.5}$$

$$y^I(t) = y_0^I + \int_{t_i}^{t} (\dot{x} \cdot \sin(\psi) + \dot{y} \cdot \cos(\psi))dt \tag{2.6}$$

where x_0^I and y_0^I indicate the initial location of the BFF in the IF at t_i.

Plotting $x^I(t)$ and $y^I(t)$ shows the time varying position of the vehicle CoM in the IF.

The orientation of the BFF relative to the IF can be found as:

$$\psi(t) = \psi_0 + \int_{t_i}^{t} (\dot{\psi})dt \tag{2.7}$$

where ψ_0 is the initial yaw angle of the BFF relative to the IF and $\dot{\psi}$ is the yaw rate of the BFF.

Now that the basic coordinate frames have been defined, the kinematics and geometric relations of the QBEAK can be derived.

2.2 Geometry of QBEAK

A *Two Track Model* is used to describe the specific lengths and angles on the QBEAK. It refers to a 4 wheeled model of the vehicle seen from above, with lengths and angles as specified on figure 2.2. A situation where the vehicle is turning left is shown on the figure. As the QBEAK is a Front Wheel Steering (FWS) car, so is the two track model. It uses the front wheels to turn the car, while the rear wheels are always pointing in the longitudinal direction of the vehicle.

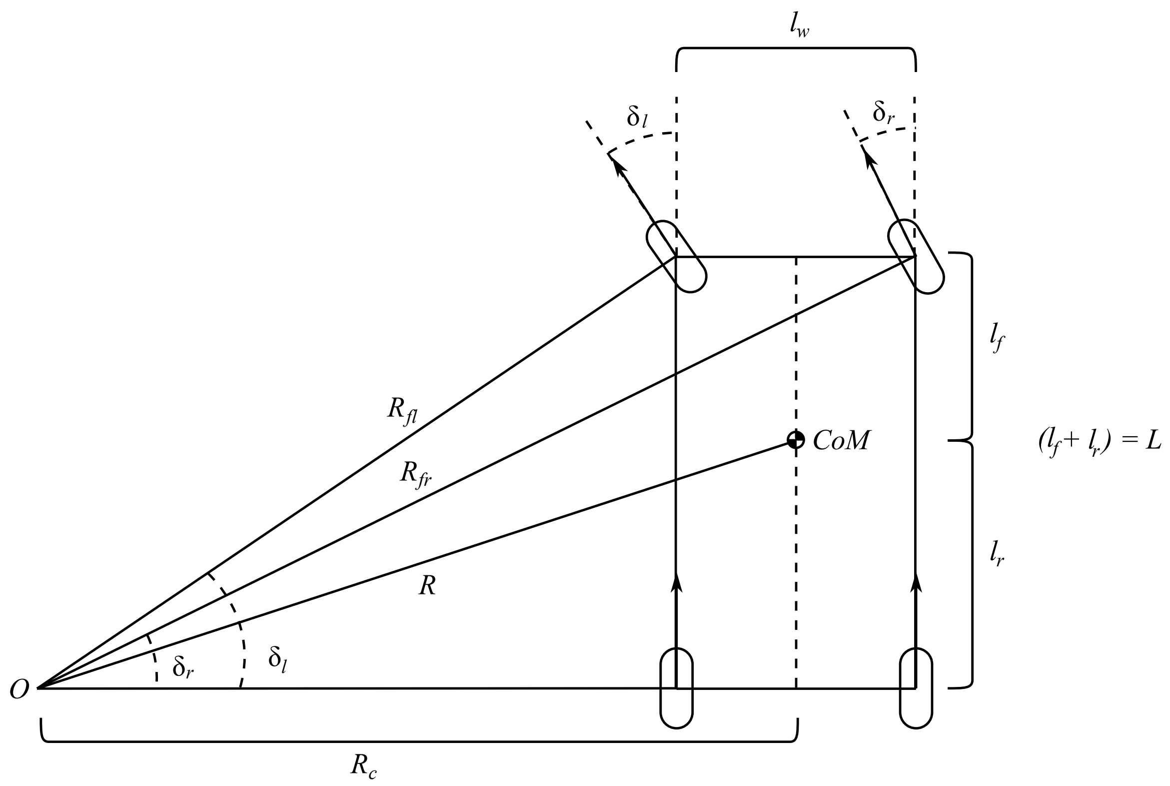

Figure 2.2: The Two track model of a vehicle turning left [16, p.379].

The two track model of the QBEAK is based on the assumption that the vehicle has a rigid body. Furthermore the vehicle is only assumed to have translatory movement in the $x^B y^B$-plane and rotation around the yaw-axis z^B. The rotation around the roll- and pitch-axes are neglected. The $x^B y^B$-plane is therefore projected to the ground and all distances are calculated in this plane.

The following distances and angles are shown in figure 2.2:

l_w : The width between the center of the left and right wheel, called the track width.
l_r : The longitudinal distance between the rear wheel axle and the projection of the CoM to the ground plane.
l_f : The longitudinal distance between the front wheel axle and the projection of the CoM to the ground plane.
L : The longitudinal distance between the front and rear wheel axles ($L = l_r + l_f$).
δ_i : The steering angle of the left or right front wheel.
O : The turn center of the vehicle.
R : The distance from the turn center to the vehicle CoM projection onto the ground plane. This distance is called the turn radius of the vehicle.
R_{fi} : The distance from front left or right wheel center to turn center.
R_c : The orthogonal distance from the longitudinal vehicle axis to the turn center.

The two track model is used calculate the geometric relations between the wheel velocity vectors and the vehicle velocity vector at the CoM. The model is also used to determine the individual steering angles at the front wheels.

2.3 Steering Kinematics

As a vehicle is turning, the turn radius is slightly different at the left and right front wheels and the steering angle at each front wheel must therefore be different. The driver of the vehicle can only specify one steering angle δ. This angle must be transformed to individual steering angles at the front wheels. The calculation of the individual steering angles is treated in this section.

2.3.1 Ackerman's Condition

A vehicle traveling at low speed can turn without developing lateral forces, i.e. the velocity vector at each wheel lie along the x^{wij}-axis and no slip is present - this is called the Ackerman condition [16, p.381], [15, p.196]. This situation is illustrated in figure 2.2.
For slip free turning the projection of the rear axle and the y^w-axes of the front wheels must cross at the turn center, O. If one of the y^w-axes does not cross through O the corresponding wheel will experience side slip [15, p.196] (see Section 2.5) and the Ackerman condition will be violated. This situation is illustrated in figure 2.3.
The steering angles of the left and right front wheel with respect to the longitudinal direction of the vehicle are denoted, δ_l and δ_r, respectively. The angles are shown in figure 2.2 for a vehicle turning left. The steering angles found in this section are therefore calculated for a vehicle turning left. For a vehicle turning right the calculations are simply switched so that the equations for the front left steering angle are used for the front right steering angle and opposite.
Using trigonometric relations the steering angles are shown to be the angles between the rear axle and R_{fl} or R_{fr} respectively. The angles are expressed as [16, 381]:

$$\tan(\delta_l) = \frac{L}{R_c - \frac{l_w}{2}} \qquad \tan(\delta_r) = \frac{L}{R_c + \frac{l_w}{2}} \tag{2.8}$$

The steering angle, δ, supplied by the driver is defined as [16, 381]:

$$\cot(\delta) = \frac{R_c}{L} = \frac{1}{2}(\cot(\delta_r) + \cot(\delta_l)) \tag{2.9}$$

and is called the Ackerman angle.

The steering angles of each front wheel are then related to the Ackerman angle by the following equations (during a left turn):

$$\begin{aligned} \delta_l &= \tan^{-1}\left(\frac{L}{L \cdot \cot(\delta) - {}^{l_w}/_2}\right) \\ \delta_r &= \tan^{-1}\left(\frac{L}{L \cdot \cot(\delta) + {}^{l_w}/_2}\right) \end{aligned} \tag{2.10}$$

The Ackermann condition is a static condition at zero velocity [16, p.381] and is therefore only suitable for analyzing low speed (parking lot maneuvers [15, p.196]). At higher vehicle velocities the cornering motion is a result of side slip which will be presented in Section 2.5. Side slip is dependent on the velocity vectors at each tire-road contact point and the angle between these vectors and the x^{wij}-axes. This angle is called the side slip angle. The calculation of the velocity vectors and side slip angles is presented in the following section.

2.4 Wheel Velocity Vectors and Side Slip Angle

Trigonometric relations will be used to transform the velocity vector at the CoM, along with the velocity contribution from the yaw rate around the CoM, into a velocity vector at the individual tire-road contact points [22, p.305].
The contact point velocity vectors should not be confused with the tangential velocity of the wheels. The difference in these velocities are responsible for the development of friction forces.

2.4.1 Velocity vectors

When the Ackermann condition is violated the velocity components at each wheel caused by the yaw rate are no longer orthogonal to the longitudinal direction of the vehicle. These velocity components are instead orthogonal to the line connecting the vehicle CoM ground projection and the tire-road contact point (r_{ij} shown in figure 2.3) [22, p.305].

In this model the tire-road contact point is assumed to be in the center of the wheel contact area as the misalignment of this point due to wheel caster- and camber angles are assumed negligible compared to the distances from the CoM to the wheel.

In figure 2.3 the distances from the turn center to the tire-road contact point of each wheel are denoted R_{ij}. These distances depend on the curvature of the turn. The velocity vector at each contact point is orthogonal to R_{ij} while the vehicle velocity in the CoM, v_{CoM}, is orthogonal to R. In the BFF the vehicle velocity vector can be divided into x^B- and y^B-components as:

$$v^B_{CoM} = \begin{bmatrix} \dot{x} \\ \dot{y} \end{bmatrix} \tag{2.11}$$

where $\dot{x}$ and $\dot{y}$ are the velocity components along the x^B- and y^B-axis respectively.

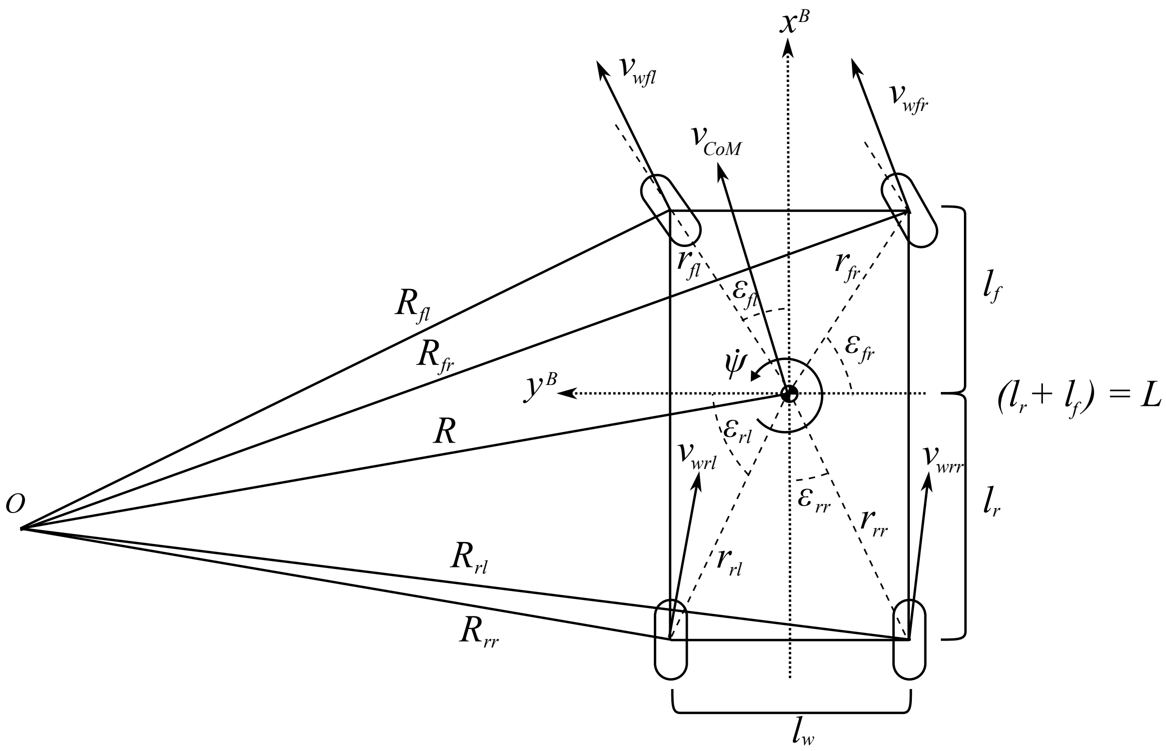

Figure 2.3: Vehicle seen from above as two track model. The geometrical relations between the velocity vectors of the individually wheels and the velocity at CoM are shown [22, p.310].

The main contribution to the individual contact point velocities is v_{CoM}^B but the yaw rate also contributes to the wheel velocity. The yaw rate is multiplied with the distance r_{ij} to get the corresponding linear velocity vector at each wheel. The x^B- and y^B-components of this vector can be found by geometric relations and using the angle ε_{ij} shown in figure 2.3. By summation of the yaw rate velocity components and v_{CoM} components, the velocity vectors for each wheel acting from the center of the tire-road contact patch can be found [22, p.309]:

$$v_{wfl}^B = \begin{bmatrix} \dot{x} - \dot{\psi} \cdot r_{fl} \cdot \sin(\varepsilon_{fl}) \\ \dot{y} + \dot{\psi} \cdot r_{fl} \cdot \cos(\varepsilon_{fl}) \end{bmatrix} \tag{2.12}$$

$$v_{wfr}^B = \begin{bmatrix} \dot{x} + \dot{\psi} \cdot r_{fr} \cdot \cos(\varepsilon_{fr}) \\ \dot{y} + \dot{\psi} \cdot r_{fr} \cdot \sin(\varepsilon_{fr}) \end{bmatrix} \tag{2.13}$$

$$v_{wrl}^B = \begin{bmatrix} \dot{x} - \dot{\psi} \cdot r_{rl} \cdot \cos(\varepsilon_{rl}) \\ \dot{y} - \dot{\psi} \cdot r_{rl} \cdot \sin(\varepsilon_{rl}) \end{bmatrix} \tag{2.14}$$

$$v_{wrr}^B = \begin{bmatrix} \dot{x} + \dot{\psi} \cdot r_{rr} \cdot \sin(\varepsilon_{rr}) \\ \dot{y} - \dot{\psi} \cdot r_{rr} \cdot \cos(\varepsilon_{rr}) \end{bmatrix} \tag{2.15}$$

where $\dot{\psi}$ is the angular velocity around the z^B-axis (yaw rate).

2.4.2 Side Slip Angle

The side slip angle α_{ij} is the angle between v_{wij} and the x^{wij}-axis. This is illustrated in figure 2.4. The angle η_{ij} in the figure relates the x^B- and y^B-components of the v_{wij} as

$$\eta_{ij} = \tan^{-1}\left(\frac{v_{ywij}}{v_{xwij}}\right) \tag{2.16}$$

thus the side slip angle can be expressed as

$$\alpha_{ij} = \delta_j - \eta_{ij} \tag{2.17}$$

where δ_j is the steering angle of the specific wheel. The subscript i is omitted as the steering angle is zero for the rear wheels. The calculation of the individual steering angles are treated in Section 2.3.

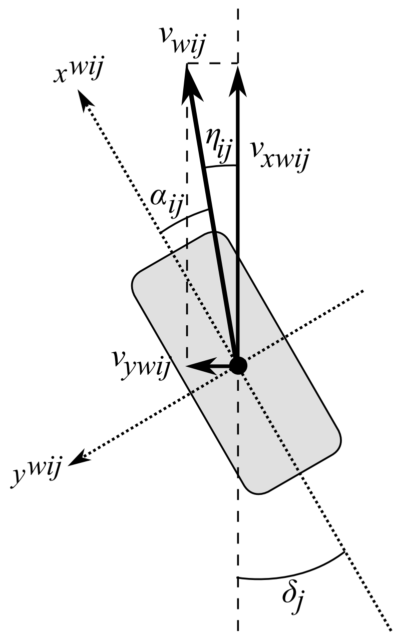

Figure 2.4: Sketch of a single wheel seen from above with the side slip angle shown.

Given the side slip angles, the slip introduced in Chapter 1 can now be defined.

2.5 Slip

Three kinds of slip exists; slip ratio (or longitudinal slip) λ_{Lij}, side slip λ_{Sij} and resulting slip $\lambda_{res,ij}$. In this section the three kinds of slip will be defined so they can be used in the calculation of friction forces and in the derivation of a slip control system.

The different slip directions are shown in figure 2.5.

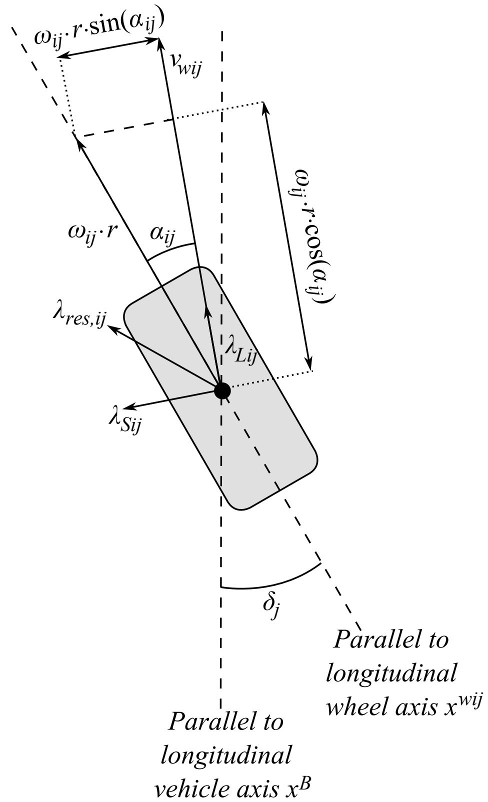

Figure 2.5: Wheel model showing direction of wheel velocity vector, tangential wheel velocity, slip ratio, side slip and resulting slip at the tire-road contact point [22, p.315].

The slip ratio is in the direction of the wheel velocity vector and the side slip is perpendicular to the slip ratio. The resulting slip is the geometric sum of the slip ratio and the side slip:

$$\lambda_{res,ij} = \sqrt{\lambda_{Lij}^2 + \lambda_{Sij}^2} \tag{2.18}$$

From figure 2.5 and [22, p.315] the slip ratio and side slip can be defined as:

	Braking $\omega_{ij} \cdot r \cdot \cos(\alpha_{ij}) \leq v_{wij}$	**Driving** $\omega_{ij} \cdot r \cdot \cos(\alpha_{ij}) > v_{wij}$
Slip ratio	$\lambda_{Lij} = \frac{\omega_{ij} \cdot r \cdot \cos(\alpha_{ij}) - v_{wij}}{v_{wij}}$	$\lambda_{Lij} = \frac{\omega_{ij} \cdot r \cdot \cos(\alpha_{ij}) - v_{wij}}{\omega_{ij} \cdot r \cdot \cos(\alpha_{ij})}$
Side slip	$\lambda_{Sij} = \frac{\omega_{ij} \cdot r \cdot \sin(\alpha_{ij})}{v_{wij}}$	$\lambda_{Sij} = \tan(\alpha_{ij})$

Table 2.1: Definition of slip ratio and side slip [22, p.315].

In table 2.1 ω_{ij} is the angular velocity of the wheel and r is the effective tire radius relating tangential and rotational velocity of the wheel.

The kinematics of the two track model has now been described and the three kinds of slip have been defined. This will be the foundation of the dynamic model derived in the following chapter.

3 Dynamic Vehicle Model

A dynamic vehicle model is developed in this chapter. The model is derived from force and torque equilibriums of the vehicle body and the individual wheels in Section 3.1. Section 3.2 to 3.7 then elaborates on each of the terms in the force- and torque equilibriums.
Variation and uncertainty of the parameters used in the model is treated in Section 3.8. Finally the implementation of the dynamic model in the MATLAB Simulink environment is described in Section 3.9.
The model will be the basis of the slip controller design in Chapter 5 and the MATLAB Simulink model will be used in simulations throughout the report.

3.1 Motional Dynamics

The dynamic model will be based on the two track model introduced in Chapter 2 and will be restricted to planar vehicle motion. The roll and pitch dynamics and vertical motion of the vehicle body is thus not modeled. The Degrees of Freedom (DoF) can thereby be reduced to 7: The longitudinal and lateral translatory motion, the yaw motion and the rotation of the 4 wheels.

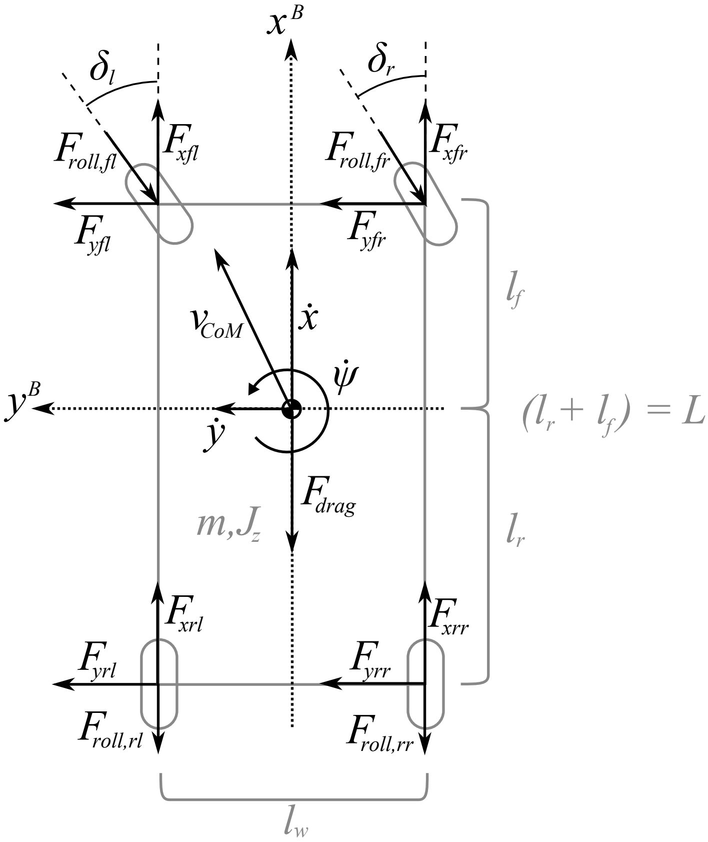

Figure 3.1: Force diagram of planar vehicle.

3.1.1 Vehicle Dynamics

The dynamics of the vehicle body is derived from force equilibriums in the x^B and y^B directions and a torque balance around the z^B-axis based on figure 3.1. The resulting equations describes the motion of the vehicle in the $x^B y^B$-plane.

The notations in figure 3.1 are explained below with $i = \{f, r\}$ for front or rear wheel and $j = \{l, r\}$ for left or right wheel:

m - The vehicle mass

J_z - The mass moment of inertia around the z^B-axis.

F_{xij} - The friction force acting on wheel ij in the direction of the vehicle longitudinal axis.

F_{yij} - The friction force acting on wheel ij in the direction of the vehicle lateral axis.

$F_{roll,ij}$ - The rolling resistance acting on wheel ij.

F_{drag} - The aerodynamic drag force due to wind resistance.

It is noted that the coordinate system used in figure 3.1 is non-inertial. The inertial acceleration in the x^B- and y^B-direction is then given by two terms; the acceleration along these axes and the centripetal acceleration [33, p.28+34+225]. The inertial acceleration in the BFF is therefore [33, p.225]:

$$\ddot{x}_{inertial} = \ddot{x} - \dot{\psi} \cdot \dot{y} \qquad \text{and} \qquad \ddot{y}_{inertial} = \ddot{y} + \dot{\psi} \cdot \dot{x}$$

Force balances in the x^B- and y^B-direction and torque balance around the z^B-axis can now be determined:

$$\boxed{\begin{aligned}
m\,(\ddot{x} - \dot{\psi} \cdot \dot{y}) &= \underbrace{\left(F_{xfr} + F_{xfl} + F_{xrr} + F_{xrl}\right)}_{F_x} - \underbrace{\left(F_{roll,fr} \cdot \cos(\delta_r) + F_{roll,fl} \cdot \cos(\delta_l) + F_{roll,rr} + F_{roll,rl}\right)}_{F_{roll,x}} - F_{drag} \\
m\,(\ddot{y} + \dot{\psi} \cdot \dot{x}) &= \underbrace{\left(F_{yfr} + F_{yfl} + F_{yrr} + F_{yrl}\right)}_{F_y} - \underbrace{\left(F_{roll,fr} \cdot \sin(\delta_r) + F_{roll,fl} \cdot \sin(\delta_l)\right)}_{F_{roll,y}} \qquad (3.1) \\
J_z \cdot \ddot{\psi} &= \frac{l_w}{2}\left(F_{xfr} + F_{xrr} - F_{xfl} - F_{xrl}\right) + l_f\left(F_{yfr} + F_{yfl}\right) - l_r\left(F_{yrr} + F_{yrl}\right)
\end{aligned}}$$

3.1.2 Wheel dynamics

The dynamics of the 4 wheels are described by a torque balance of each wheel based on the system seen in figure 3.2.

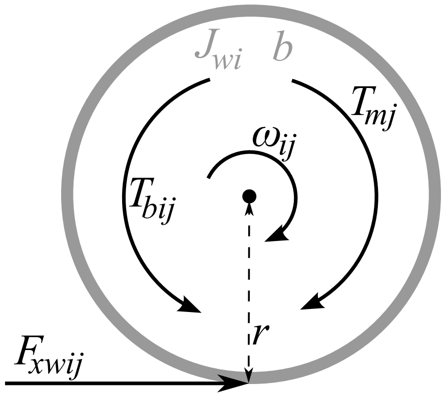

Figure 3.2: Free body diagram of one wheel.

The notations in figure 3.2 are explained below:

J_{wi} - The wheel inertia of a front or rear wheel. The inertia of the left and right side wheels are assumed equal, but the inertia of the PMSM rotors - acting on the wheel through the gear - causes unequal inertias of the front and rear wheels. The two motors are each connected to a front wheel with no possibility to mechanically disconnect. The equivalent rotor inertia on the wheel axle equals the actual rotor inertia multiplied with the gearing ratio squared [10, p.84-85].

b - The viscous friction coefficient at each wheel axle - assumed equal for all wheels.

T_{mj} - The torque transmitted through the gear by the PMSM at the front left or right wheel. This torque is zero for the rear wheels.

T_{bij} - The braking torque acting on wheel ij.

F_{xwij} - The friction force acting on wheel ij in the direction of x^{wij}-axis resulting from friction in the road-wheel contact patch.

The torque balance around the wheel center of rotation is:

$$\boxed{J_{wi} \cdot \dot{\omega}_{ij} = T_{mj} - T_{bij} \cdot \mathrm{sign}(\omega_{ij}) - b \cdot \omega_{ij} - r \cdot F_{xwij} \quad (3.2)}$$

The braking torque always counteracts the movement of the wheel, hence the sign-function in equation (3.2).

The dynamic vehicle model given by the equations of (3.1) and (3.2) describes the vehicle motion in the $x^B y^B$-plane. The following sections provide the expression of the torques and forces used in these equations.

3.2 Tire-Road Friction

The tire forces developed during driving mainly result from deformation of the tire. The deformation is a result of the elasticity of the tire material, the difference in velocities at the tire-road contact patch and the friction characteristics of the road surface. The tire-road friction force at each wheel is typically given as [35, 19]:

$$F_{\mu,ij} = F_{zij} \cdot \mu_{ij} \tag{3.3}$$

where μ_{ij} is the friction coefficient and F_{zij} is the vertical normal force acting on the wheel. The normal force is described in Section 3.7.
Different analytically derived models of the friction coefficient exist [33, ch.13], but the complexity of the force behavior, and the resulting simplifications made in the modeling approach, give rise to modeling inaccuracies. The analytical friction models typically yield accurate results at low slip but deviate in large slip or combined slip situations [33, p.421].
Several empirical friction models exist and some yield very accurate results in many operating situations. One of the most widely used is the *Burckhardt* tire model [35], [22], [9], [16], [42], [19], [30]. It models the friction coefficient as [22, p.319][1]:

$$\mu_{ij} = c_1 \cdot \left(1 - e^{-c_2 \cdot \lambda_{res,ij}}\right) - c_3 \cdot \lambda_{res,ij} \tag{3.4}$$

where $\lambda_{res,ij}$ is the resulting slip of equation 2.18 and c_1, c_2 and c_3 are road surface dependent coefficients given in table 3.1 for different road surfaces.

	c_1	c_2	c_3
Asphalt, dry	1.2801	23.99	0.52
Asphalt, wet	0.857	33.822	0.347
Concrete, dry	1.1973	25.168	0.5373
Cobblestone, dry	1.3713	6.4565	0.6691
Cobblestone, wet	0.4004	33.708	0.1204
Snow	0.1946	94.129	0.0646
Ice	0.05	306.39	0

Table 3.1: Road surface dependent coefficient of the Burckhardt tire friction model [22, p.322].

Because of its simplicity and well known coefficients the friction model will be used to model tire-road friction forces in this project.

A plot of the friction coefficient as a function of the resulting slip for different road surfaces is seen in figure 3.3. It is observed that the friction coefficient increases approximately linearly with slip at very low slip values. The friction coefficient then increases to a single peak value for each road surface before decreasing approximately linearly until $\lambda_{res,ij} = 1$. It is clearly seen from figure 3.3 that the maximum friction coefficient is highly dependent on the road surface, as is the corresponding slip value. Determining the unknown friction behavior, i.e. the unknown parameters c_1, c_2 and c_3, is one of the main difficulties when designing a slip control system. This problem will be treated in Section 5.5.

[1] An extended model which takes velocity and load effects into account is also given in [22, p.319]. This model will not be used due to the increased number of coefficients to be determined as well as increased nonlinearity in the coefficients.

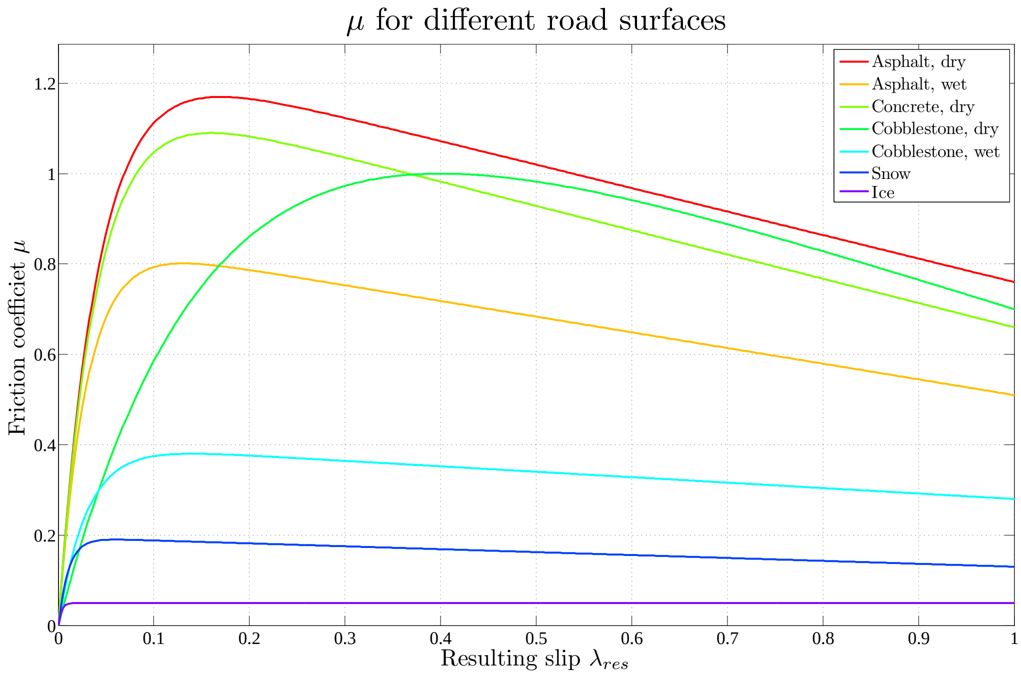

Figure 3.3: Friction coefficient as a function of resulting slip at different road conditions.

During vehicle motion with combined slip the friction coefficient will have a longitudinal component in the direction of the wheel velocity vector and a lateral component perpendicular to it. The components can be found as [22, p.321]:

$$\mu_{Lij} = \mu_{ij} \cdot \frac{\lambda_{Lij}}{\lambda_{res,ij}}$$
$$\mu_{Sij} = \mu_{ij} \cdot \frac{\lambda_{Sij}}{\lambda_{res,ij}} \tag{3.5}$$

and the corresponding longitudinal and lateral friction forces can be calculated as:

$$F_{Lij} = F_{zij} \cdot \mu_{Lij}$$
$$F_{Sij} = F_{zij} \cdot \mu_{Sij} \tag{3.6}$$

The longitudinal and lateral friction forces act in the same direction as the corresponding friction coefficient components. To calculate the friction forces F_{xij} and F_{yij} acting in the direction of the vehicle longitudinal and lateral axes figure 3.4 is considered.

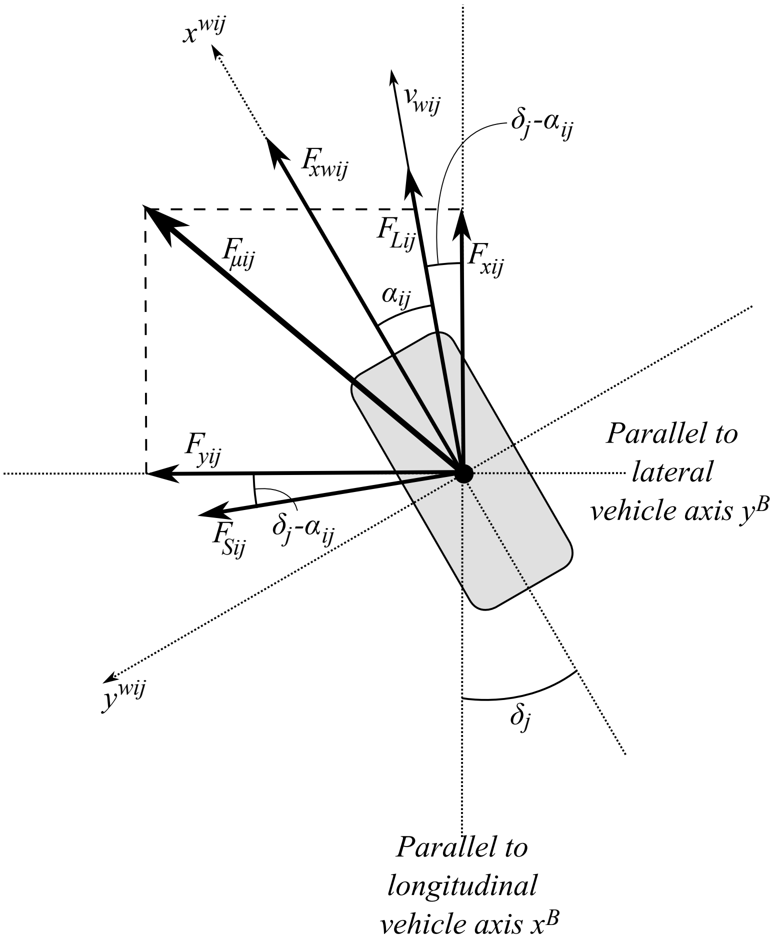

Figure 3.4: Projection of the friction force onto the vehicle longitudinal and lateral axes.

The F_{xij} and F_{yij} components of the friction force can be obtained by projecting F_{Lij} and F_{Sij} onto the x^B- and y^B-axis:

$$\begin{aligned} F_{xij} &= F_{Lij} \cdot \cos(\delta_j - \alpha_{ij}) - F_{Sij} \cdot \sin(\delta_j - \alpha_{ij}) \\ F_{yij} &= F_{Sij} \cdot \cos(\delta_j - \alpha_{ij}) + F_{Lij} \cdot \sin(\delta_j - \alpha_{ij}) \end{aligned} \tag{3.7}$$

Substituting equation (3.5) into (3.6) and inserting into equation (3.7) yields:

$$F_{xij} = F_{zij} \cdot \mu_{ij} \cdot \frac{\lambda_{Lij}}{\lambda_{res,ij}} \cdot \cos(\delta_j - \alpha_{ij}) - F_{zij} \cdot \mu_{ij} \cdot \frac{\lambda_{Sij}}{\lambda_{res,ij}} \cdot \sin(\delta_j - \alpha_{ij}) \qquad \Rightarrow$$

$$\boxed{F_{xij} = F_{zij} \cdot \frac{\mu_{ij}}{\lambda_{res,ij}} \left(\lambda_{Lij} \cdot \cos(\delta_j - \alpha_{ij}) - \lambda_{Sij} \cdot \sin(\delta_j - \alpha_{ij})\right)} \tag{3.8}$$

and

$$F_{yij} = F_{zij} \cdot \mu_{ij} \cdot \frac{\lambda_{Sij}}{\lambda_{res,ij}} \cdot \cos(\delta_j - \alpha_{ij}) + F_{zij} \cdot \mu_{ij} \cdot \frac{\lambda_{Lij}}{\lambda_{res,ij}} \cdot \sin(\delta_j - \alpha_{ij}) \qquad \Rightarrow$$

$$\boxed{F_{yij} = F_{zij} \cdot \frac{\mu_{ij}}{\lambda_{res,ij}} \left(\lambda_{Sij} \cdot \cos(\delta_j - \alpha_{ij}) + \lambda_{Lij} \cdot \sin(\delta_j - \alpha_{ij})\right)} \tag{3.9}$$

Equation (3.8) and (3.9) are used in the longitudinal and lateral force balance as well as the torque balance around the z^B-axis (see equation (3.1)).

The friction force F_{xwij} used in the wheel torque balance of equation 3.2 can be found in a similar manner as the projection of F_{Lij} and F_{Sij} onto the x^{wij}-axis. Observation of figure 3.4 shows that F_{xwij} can be found as:

$$\begin{aligned} F_{xwij} &= F_{Lij} \cdot \cos(\alpha_{ij}) + F_{Sij} \cdot \sin(\alpha_{ij}) \\ &= F_{zij} \cdot \mu_{ij} \cdot \frac{\lambda_{Lij}}{\lambda_{res,ij}} \cdot \cos(\alpha_{ij}) + F_{zij} \cdot \mu_{ij} \cdot \frac{\lambda_{Sij}}{\lambda_{res,ij}} \cdot \sin(\alpha_{ij}) \qquad \Rightarrow \end{aligned}$$

$$\boxed{F_{xwij} = F_{zij} \cdot \frac{\mu_{ij}}{\lambda_{res,ij}} \left(\lambda_{Lij} \cdot \cos(\alpha_{ij}) + \lambda_{Sij} \cdot \sin(\alpha_{ij})\right)} \tag{3.10}$$

3.2.1 Friction Characteristics

The maneuverability of the vehicle is most easily understood by analyzing the behavior of longitudinal and lateral friction coefficients μ_{Lij} and μ_{Sij}. The characteristics of the friction coefficients are therefore analyzed for different values of slip ratio and side slip.

During stable driving no side slip angle greater than 16° can occur [22, p.325]. The tire-road frictional behavior is therefore only considered for $\alpha_{ij} \leq 16°$. It is noted from equation (3.5) that there is a trade-off between longitudinal and lateral friction. This is illustrated in the graphs of figure 3.5 and 3.6. The graphs show plots of the lateral friction coefficient vs the longitudinal friction coefficient for braking and driving respectively. The two figures show similarities but are slightly different due to the fact that side slip depends on slip ratio during braking. The dotted curve in the plots indicates the maximum achievable friction corresponding to the peak of μ in figure 3.3. This limit is called the *friction circle* or *Kamm circle* as it resembles a circle with radius equal to the maximum achievable friction coefficient [22, p.321].

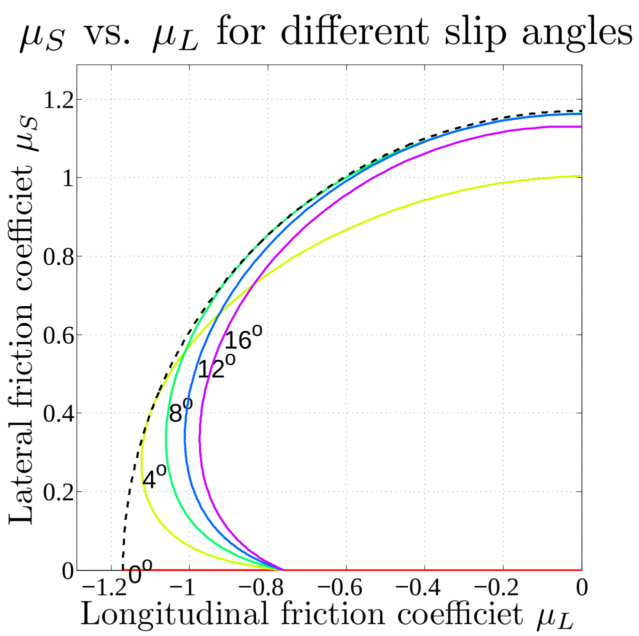

Figure 3.5: Lateral and longitudinal friction coefficient for different side slip angles during braking.

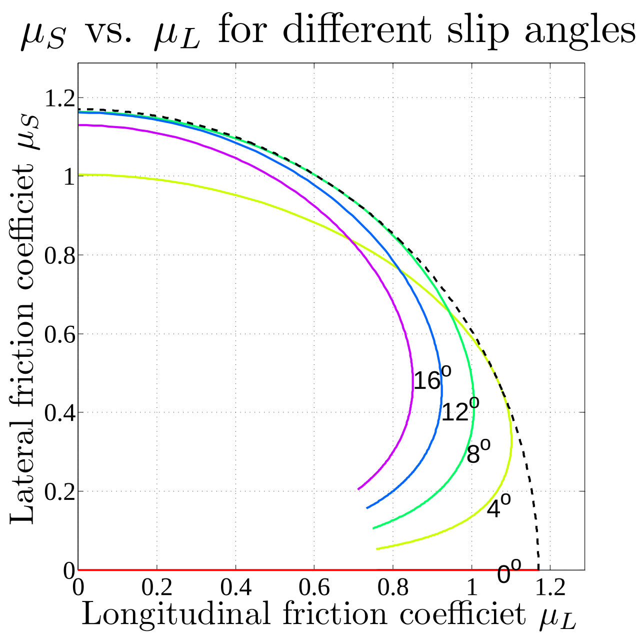

Figure 3.6: Lateral and longitudinal friction coefficient for different side slip angles during driving.

It is seen that for zero side slip angles all of the available friction is in the longitudinal wheel direction (x^{wij}). It is also seen that for all non-zero side slip angles the maximum lateral friction coefficient is achieved when the slip ratio is zero. An optimal trade-off between longitudinal and lateral friction is achieved when the curves in figure 3.6 and 3.5 reach the Kamm circle. At this slip combination the maximum tire-road friction is utilized. The resulting slip at this point is denoted $\lambda_{max,ij}$ - the subscript ij indicates the possible difference in road surfaces at the individual wheels. The resulting slip can always be kept equal to $\lambda_{max,ij}$ - as long as the side slip is less than or equal to $\lambda_{max,ij}$ - by adjusting the slip ratio according to:

$$|\lambda_{Lij}| = \sqrt{\lambda_{max,ij}^2 - \lambda_{Sij}^2} \tag{3.11}$$

The longitudinal and lateral friction coefficients dependency on slip ratio and side slip is illustrated on the graphs in figure 3.7 and 3.8. The graphs show the longitudinal and lateral friction coefficient as a function of slip ratio for different side slip angles. The plots correspond to a dry asphalt road surface, however the same qualitative results hold for other surfaces.

By observing the graph of figure 3.7 it is seen that increasing side slip angle reduces the longitudinal friction coefficient. Furthermore it is seen that increasing side slip angle shifts the peak of the curve to a higher (absolute) slip ratio value. It is also noted that the longitudinal friction coefficient only has one extremum value for braking and one for driving. On the other hand it is possible to find two different values of slip ratio corresponding to the same friction coefficient value. The friction coefficient directly affects the wheel acceleration, i.e. stabilization of the wheel acceleration does not necessarily result in stabilization of the slip at the desired value. This is a good motivation for controlling the slip ratio instead of the wheel acceleration.

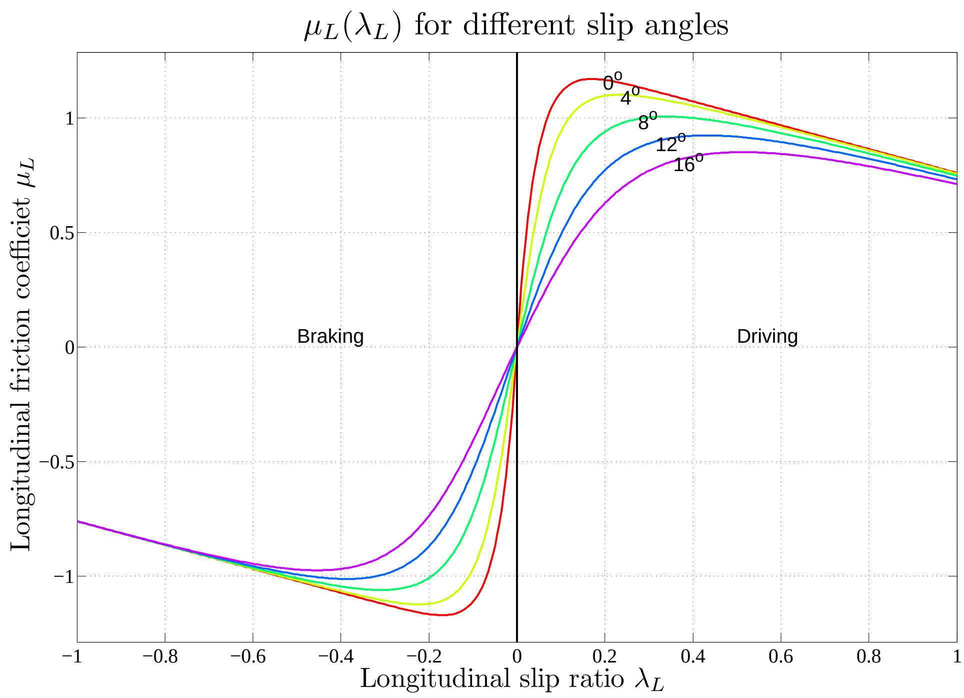

Figure 3.7: Longitudinal friction coefficient as a function of slip ratio for different side slip angles.

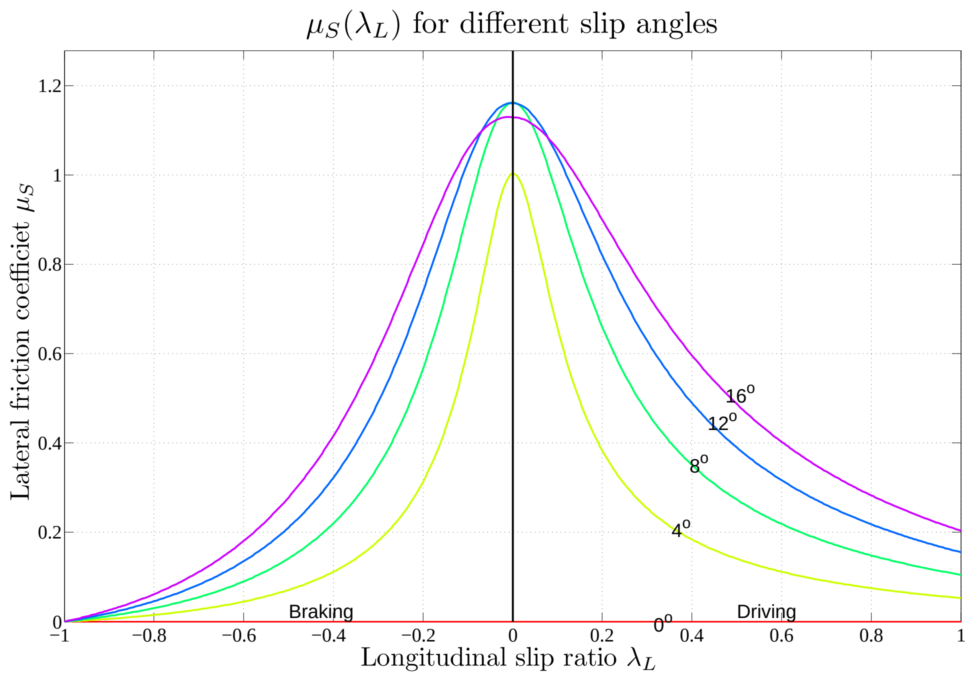

Figure 3.8: Lateral friction coefficient as a function of slip ratio for different side slip angles.

By observing the graph of figure 3.8 it is seen that increasing the (absolute) slip ratio value reduces the lateral friction coefficient from its maximum value at $\lambda_{Lij} = 0$ as expected. Furthermore it is seen that if the wheels lock during braking ($\lambda_{Lij} = -1$) no lateral friction force can be developed, i.e. the orientation of the velocity

vector cannot be altered and maneuverability is lost. The same cannot be concluded for $\lambda_{Lij} = 1$ although the lateral friction coefficient is reduced significantly.
Finally it is noted that increasing side slip angle does not necessarily increase the lateral friction coefficient as too much side slip will result in $\lambda_{res} > \lambda_{max}$.

The development of slip and thus the development of friction forces can only be controlled by varying the tangential wheel velocities relative to the velocity of the vehicle. The wheel dynamics are actuated by the PMSMs and the hydraulic brakes. These are described in the following sections.

3.3 Permanent Magnet Synchronous Machine

PMSM's on the QBEAK are controlled by two Sevcon Gen4 motor controllers using PI vector control.
A PMSM can be adequately modeled by transforming the voltage equations of the machine from the stationary 3-phase *abc*-frame to a 2-phase *dq*-frame rotating with the electrical frequency of the rotor ω_{re}[2]. The idea behind this reference frame transformation is that the position dependent inductances of the machine can be made position independent in the rotating frame. For a detailed description of *abc*-*dq* reference transformation and modeling of PMSM's the reader is referred to [6].

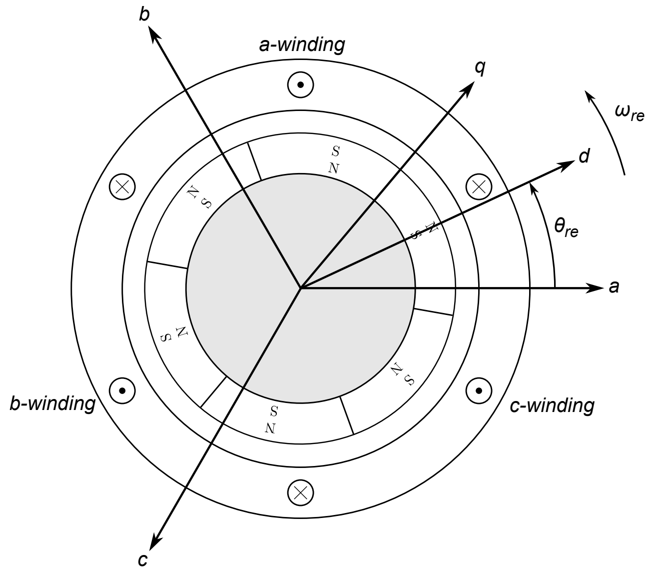

Figure 3.9: Cross sectional view of a PMSM with surface mounted rotor magnets. The *abc*-frame and the *dq*-frame are illustrated on the figure.

The resulting voltage equations described in the rotating *dq*-frame are [6, p.37]:

[2] The electrical frequency is equal to the mechanical rotational speed of the rotor multiplied by the number of pole pairs $\omega_{re} = \omega_{rm} \cdot n_{pp}$

$$
\begin{aligned}
v_d &= R_s \cdot i_d + \frac{d}{dt}\lambda_d - \overbrace{\omega_{re} \cdot \lambda_q}^{\text{coupling term}} \\
v_q &= R_s \cdot i_q + \frac{d}{dt}\lambda_q + \underbrace{\omega_{re} \cdot \lambda_d}_{\text{coupling term}}
\end{aligned}
\tag{3.12}
$$

where R_s is the phase resistance, v_d, v_q, i_d, i_q, λ_d and λ_q are the voltages, currents and flux linkages in the d- and q-axes respectively. The flux linkages λ_d and λ_q are given as:

$$
\begin{aligned}
\lambda_d &= L_d \cdot i_d + \lambda_{pm,max} \\
\lambda_q &= L_q \cdot i_q
\end{aligned}
\tag{3.13}
$$

where L_d and L_q are the d- and q-axis inductances[3] and $\lambda_{pm,max}$ is the peak value of the flux linkage from the permanent magnets.

The electromechanical torque produced by the motor is [6, p.39]:

$$
T_e = \frac{3}{2} \cdot n_{pp} \cdot (\lambda_d \cdot i_q - \lambda_q \cdot i_d) \tag{3.14}
$$

where n_{pp} is the number of pole pairs.
Inserting equation (3.13) into equation (3.14) and noting that $L_d = L_q$ yields:

$$
\begin{aligned}
T_e &= \frac{3}{2} \cdot n_{pp} \cdot (\lambda_{pm,max} \cdot i_q + L_d \cdot i_d \cdot i_q - L_q \cdot i_q \cdot i_d) \\
&= \frac{3}{2} \cdot n_{pp} \cdot \lambda_{pm,max} \cdot i_q
\end{aligned}
\tag{3.15}
$$

It is observed from equation (3.15) that the d-axis current does not contribute to the electromechanical torque developed by the motor. Thus the reference d-axis current is often controlled to zero. However, the Gen4 uses a flux weakening controller at high speed which involves injecting negative d-axis current to counteract the back-emf ε given by:

$$
\varepsilon = \omega_{re} \cdot \lambda_{pm,max}
$$

The negative i_d decreases λ_d [37, p.23,pt.6.3] - see equation (3.12) and (3.13). The term "vector control" derive

[3] L_d and L_q are equal in a surface mounted PMSM

from the fact that the d- and q-currents are controlled independently based on desired torque and flux.

Inserting equation (3.13) into (3.12), noting that $\frac{d}{dt}\hat{\lambda}_{pm} = 0$ and Laplace transforming yields:

$$
\begin{aligned}
i_d &= \frac{1}{L_d \cdot s + R_s} \cdot v_d + \frac{1}{L_d \cdot s + R_s} \cdot \overbrace{\omega_{re} \cdot L_q \cdot i_q}^{couplingterm} \\
i_q &= \frac{1}{L_q \cdot s + R_s} \cdot v_q + \frac{1}{L_q \cdot s + R_s} \cdot \underbrace{\omega_{re} \cdot (L_d \cdot i_d + \lambda_{pm,max})}_{couplingterms}
\end{aligned}
\tag{3.16}
$$

Thus the current of each of the dq-axes is a filtered combination of the applied voltage and the coupling terms. The current can therefore be controlled using the control structure illustrated in figure 3.10.

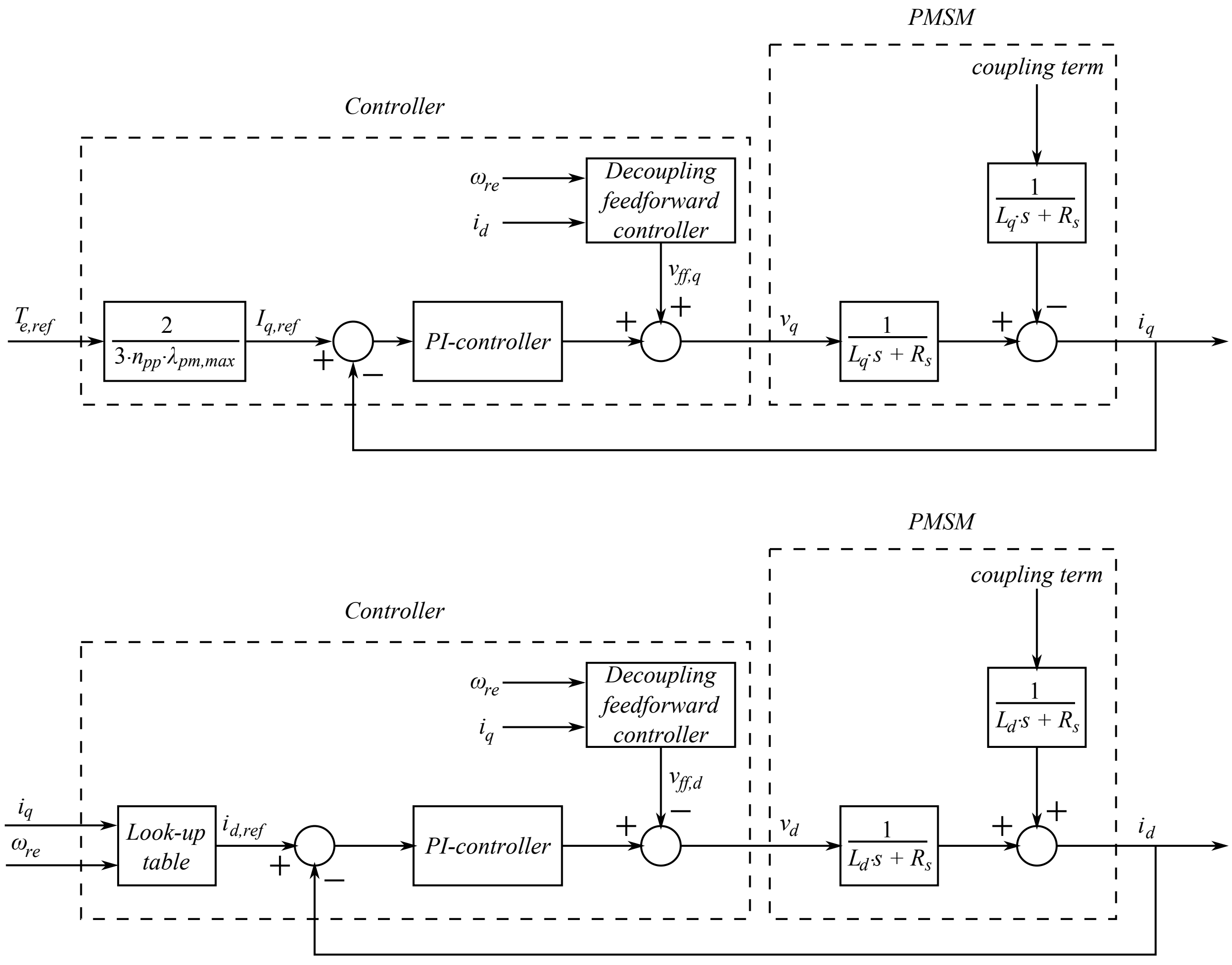

Figure 3.10: Block diagram of vector control system.

The decoupling feedforward control in figure 3.10 is used to decouple the phases using the following feedforward terms:

$$
\begin{aligned}
v_{ff,d} &= \omega_{re} \cdot L_q \cdot i_q \\
v_{ff,q} &= \omega_{re} \cdot \left(L_d \cdot i_d + \hat{\lambda}_{pm} \right)
\end{aligned}
\tag{3.17}
$$

The disturbances caused by the coupling terms are therefore compensated for.

In the further modeling of the PMSM's it is assumed that flux weakening control is not enabled, thus i_d is assumed equal to zero.
The torque developed by the PMSM's will be modeled as a transfer function represented by the closed-loop i_q-current control system combined with equation (3.15):

$$
T_e = \frac{K \cdot \frac{k_P \cdot s + k_I}{s} \cdot \frac{1}{L_q \cdot s + R_s}}{1 + K \cdot \frac{k_P \cdot s + k_I}{s} \cdot \frac{1}{L_q \cdot s + R_s}} \cdot T_{e,ref}
$$

where $K \cdot k_P$ is the proportional gain and $K \cdot k_I$ is the integral gain of the controller. The controller parameters are chosen so that they cancel the dynamics of the PMSM and thus reduce the open-loop dynamics of the motor to an integrator with gain K:

$$
\begin{aligned}
K &= 444.44 \\
k_P &= L_q = 45 \cdot 10^{-6} \\
k_I &= R_s = 3 \cdot 10^{-3}
\end{aligned}
$$

The closed-loop dynamics are then given as:

$$
T_e = \frac{1}{\frac{1}{K} \cdot s + 1} \cdot T_{e,ref} \tag{3.18}
$$

The torque developed at each front wheel axle T_{mj} is obtained by multiplying (3.18) by n for each wheel:

$$
T_{mj} = \frac{1}{\frac{1}{K} \cdot s + 1} \cdot n \cdot T_{ej,ref} = \frac{1}{\tau_m \cdot s + 1} \cdot T_{mj,ref} \tag{3.19}
$$

Thus, the motor torque is obtained as a first order filtering of the torque reference with a time constant of $\tau_m = 1/K = 2.3$ $[ms]$. This corresponds to a 2 % settling time of 9.0 $[ms]$.

It must be noted that the magnitude of the motor torque is not allowed to exceed $T_{ej,max} = 19.1$ $[N \cdot m]$ thus T_{mj} is limited as $|T_{mj}| \leq n \cdot T_{ej,max} = T_{mj,max} = 198.02$ $[N \cdot m]$.

3.4 Hydraulic Brakes

Data of the hydraulic braking system mounted on the QBEAK has not been available. A simplified dynamic model of the braking system is therefore used.
It is assumed that the brake pressure can be controlled by feedback resulting in a closed-loop braking system that will be modeled as a first order filter. The brake dynamics are then given as:

$$P_{bij} = \frac{1}{\tau_b \cdot s + 1} \cdot P_{bij,ref} \tag{3.20}$$

where P_{bij} is the braking pressure applied from the brake actuators, and $P_{bij,ref}$ is the reference brake pressure.

The braking pressure can be assumed proportional to the braking torque [33, p.229]. The braking torque is therefore modeled as:

$$\boxed{T_{bij} = \frac{1}{\tau_b \cdot s + 1} \cdot T_{bij,ref}} \tag{3.21}$$

The time constant of the braking dynamics is set to $\tau_b = 30$ $[ms]$ based on the transients observed for the feedback controlled hydraulic brake systems in [20] and [24]. This corresponds to a 2 % settling time of 117.4 $[ms]$.

The brake pressure will be limited in a real brake system. However, it is assumed that the brakes can deliver brake pressures high enough to lock the wheels at a high friction road surface, thus the limitation of the brake pressure is omitted in the model.

3.5 Wind Resistance

A moving vehicle will experience a wind resistance force due to the interaction between air stream and vehicle body. If the vehicle velocity vector is assumed to have the longest component in the longitudinal direction, then the wind resistance force vector will have the longest component opposite this direction. The wind resistance force opposing the vehicle longitudinal motion is called the aerodynamic drag force. The forces opposing lateral and vertical vehicle motion are called sideforce and lift. In this project only the aerodynamic drag force will be considered.
The drag force can be modeled as [15, p.97]:

$$F_{drag} = \frac{\rho}{2} \cdot A \cdot c_D \cdot v_{rel}^2 \cdot \mathrm{sign}(v_{rel}) \tag{3.22}$$

where c_D is the drag coefficient, ρ is the density of the air and A is the area of the vehicle perpendicular to the relative wind velocity v_{rel}. The relative wind velocity consists of two terms; the velocity of the vehicle and the velocity of the wind, i.e. $v_{rel} = \dot{x} + v_{wind}$. The wind velocity, v_{wind} is considered positive for headwind and negative for tailwind. The longitudinal vehicle velocity $\dot{x}$ is shown in figure 3.1.
The vehicle velocity is assumed to be much larger than the velocity of the wind according to [15, p.99]. The wind velocity will therefore be neglected resulting in $v_{rel} = \dot{x}$ and

$$\boxed{F_{drag} = \frac{\rho}{2} \cdot A \cdot c_D \cdot \dot{x}^2 \cdot \mathrm{sign}(\dot{x})} \tag{3.23}$$

The drag force mainly effects the vehicle motion at high speed due to the quadratic term $\dot{x}^2$. At low speed the force is often neglected in analyses [15, p.46+49].

3.6 Rolling Resistance

At low speed the main force resisting longitudinal motion is the rolling resistance of the tires. Generally the rolling resistance is the main resistive force for speeds up to approximately 80 to 95 $[km/h]$ where the aerodynamic drag force exceeds the rolling resistance in magnitude [15, p.110].

The rolling resistance is caused by at least seven different mechanisms [15, p.110]:

- Energy loss due to deflection of the thread elements.
- Energy loss due to deflection of the tire sidewall near the contact patch.
- Scrubbing of the tires in the contact patch.
- Slip ratio and side slip.
- Deflection of the road surface.
- Air drag on the tire.
- Energy loss on bumps.

The main contribution to the rolling resistance is the energy loss caused by deflection of the tire thread elements [33, p.104]. As the wheels are rolling, new tire material continuously enters the contact patch where it is deformed due to the normal force acting on it. The material is not purely elastic but contains internal damping. As a result, the energy spent in compressing the tire is not fully recovered when the tire is expanded to its original shape. This causes an asymmetrical distribution of the normal force acting on the tire as illustrated in figure 3.11.

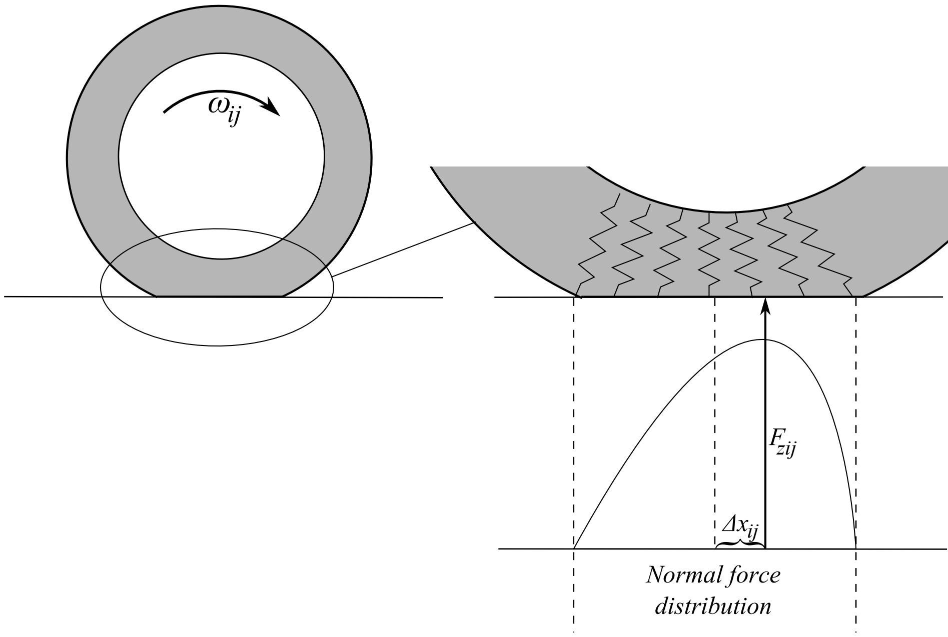

Figure 3.11: Illustration of normal force distribution when the wheel is rolling [33, p.105].

If the tire elements are considered as a finite number of individual springs, the asymmetric force distribution can be explained by the fact that the energy used to compress the springs in the first half of the contact patch is not fully recovered in the last half of the contact patch. Hence the resultant normal force is displaced forward by a distance Δx_{ij} when the tires are rolling. The torque created by this displacement around the wheel center is equal to $F_{zij} \cdot \Delta x_{ij}$ and must be balanced by the torque created by the rolling resistance given by $F_{roll,ij} \cdot r$ [33, p.105]. Thus

$$F_{roll,ij} = \frac{F_{zij} \cdot \Delta x_{ij}}{r} \tag{3.24}$$

As Δx_{ij} is not easily measured and varies with speed and temperature [p.106][33], [15, p.111-113] a proportionality constant c_{roll} (referred to as the rolling resistance coefficient) is often used as an approximation of $\Delta x_{ij}/r$ reducing equation (3.24) to:

$$F_{roll,ij} = c_{roll} \cdot F_{zij}$$

The rolling resistance always opposes rotation of the wheels. In order to satisfy this condition the rolling resistance is calculated as:

$$F_{roll,ij} = c_{roll} \cdot F_{zij} \cdot \text{sign}(\omega_{ij}) \tag{3.25}$$

Typical values of c_{roll} are given in table 3.2.

Road and pavement condition	c_{roll}
Very good concrete	0.008-0.1
Very good asphalt	0.01-0.0125
Average concrete	0.01-0.015
Average asphalt	0.018
Good stone paving	0.033-0.055
Concrete in poor condition	0.02
Ashpalt in poor condition	0.23
Stone pavement in poor condition	0.085
Shallow snow (5 cm)	0.025
Thick snow (10 cm)	0.037
Sand	0.15-0.3

Table 3.2: Typical rolling resistance coefficient values for selected road surfaces [16, p.121].

The value of c_{roll} is dependent on many factors besides road condition. Other factors influencing c_{roll} are [16, p.]: tire speed, inflation pressure, side slip, wear, temperature, load, braking forces and tractive forces.

3.7 Vehicle Load

The normal force acting on the each wheel affects the friction forces as well as the rolling resistance developed at that wheel. The normal force distribution is dependent on the location of the CoM and the longitudinal and lateral acceleration of the vehicle. In this section the normal forces for each wheel will be derived. The suspension dynamics will not be considered as vertical vehicle motion is neglected. The normal force derivation will therefore be made with the assumption of infinite suspension stiffness. Furthermore the normal force distribution caused by wind and rolling resistance is not considered.

As planar motion is considered the total vehicle load $m \cdot g$ must be counterbalanced by the total normal force:

$$F_{zfr} + F_{zfl} + F_{zrr} + F_{zrl} = m \cdot g \tag{3.26}$$

3.7.1 Lateral Normal Force Distribution

The normal force distribution between the left and right wheel pairs can be determined from a torque balance around the x^B-axis. This torque balance is based on the force diagram seen in figure 3.12.

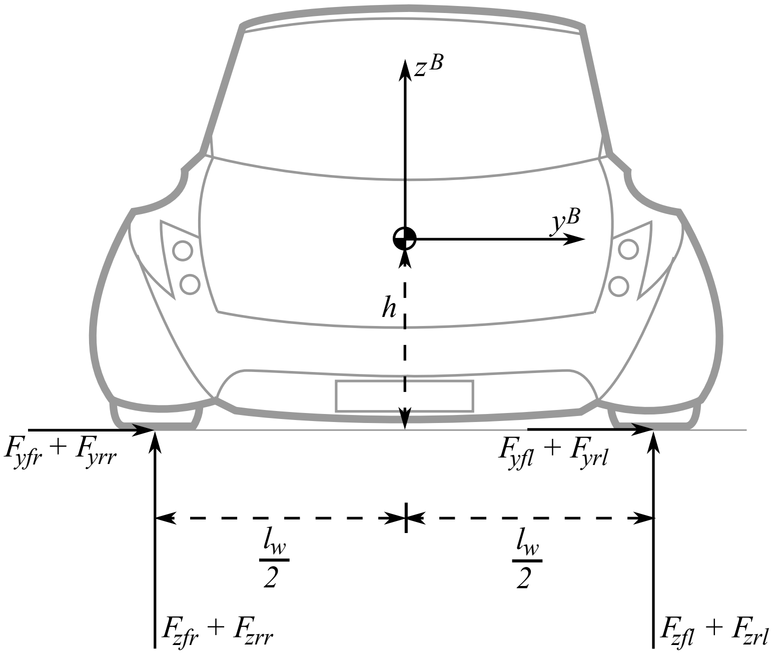

Figure 3.12: Vehicle sketch seen from the front showing forces acting in the y^B and z^B directions.

The torque balance around the x^B-axis yields:

$$\frac{l_w}{2}\left(F_{zfl} + F_{zrl} - F_{zfr} - F_{zrr}\right) + h\left(F_{yfr} + F_{yfl} + F_{yrr} + F_{yrl}\right) = 0 \tag{3.27}$$

As wind and rolling resistance is neglected the force balance of equation (3.1) reduces to:

$$F_{yfr} + F_{yfl} + F_{yrr} + F_{yrl} = m\left(\ddot{y} + \dot{\psi} \cdot \dot{x}\right) \tag{3.28}$$

Inserting equation (3.28) into (3.27) yields:

$$\frac{l_w}{2}\left(F_{zfl} + F_{zrl} - F_{zfr} - F_{zrr}\right) + h \cdot m\left(\ddot{y} + \dot{\psi} \cdot \dot{x}\right) = 0 \tag{3.29}$$

Isolating the term $F_{zfl} + F_{zrl}$ in equation (3.26) and inserting this term into equation (3.29) yields:

$$F_{zfr} + F_{zrr} = F_{zr} = \frac{m \cdot g}{2} + \frac{h \cdot m}{l_w}\left(\ddot{y} + \dot{\psi} \cdot \dot{x}\right) \tag{3.30}$$

The left side terms $F_{zfl} + F_{zrl} = F_{zl}$ are found using a similar approach:

$$F_{zfl} + F_{zrl} = F_{zl} = \frac{m \cdot g}{2} - \frac{h \cdot m}{l_w}\left(\ddot{y} + \dot{\psi} \cdot \dot{x}\right) \tag{3.31}$$

The left side and right side forces consists of a static term containing only constant values and a dynamic term containing the vehicle lateral acceleration. It is observed that the static vehicle load $m \cdot g$ is distributed equally between the left/right wheel pair because of symmetry through the $x^B z^B$-plane. The dynamic loads however are transfered from the left wheel pair to the right wheel pair when the vehicle accelerates to the left (positive lateral acceleration) and vice versa.

The dynamic loads stated in equation (3.31) and (3.30) are shared equally between the front and rear wheels as they balance torque around the longitudinal vehicle axis only.

3.7.2 Longitudinal Normal Force Distribution

The normal force distribution between the front and rear wheels can be determined from a torque balance around the y^B-axis following a similar approach. The torque balance is based on the force diagram seen in figure 3.13.

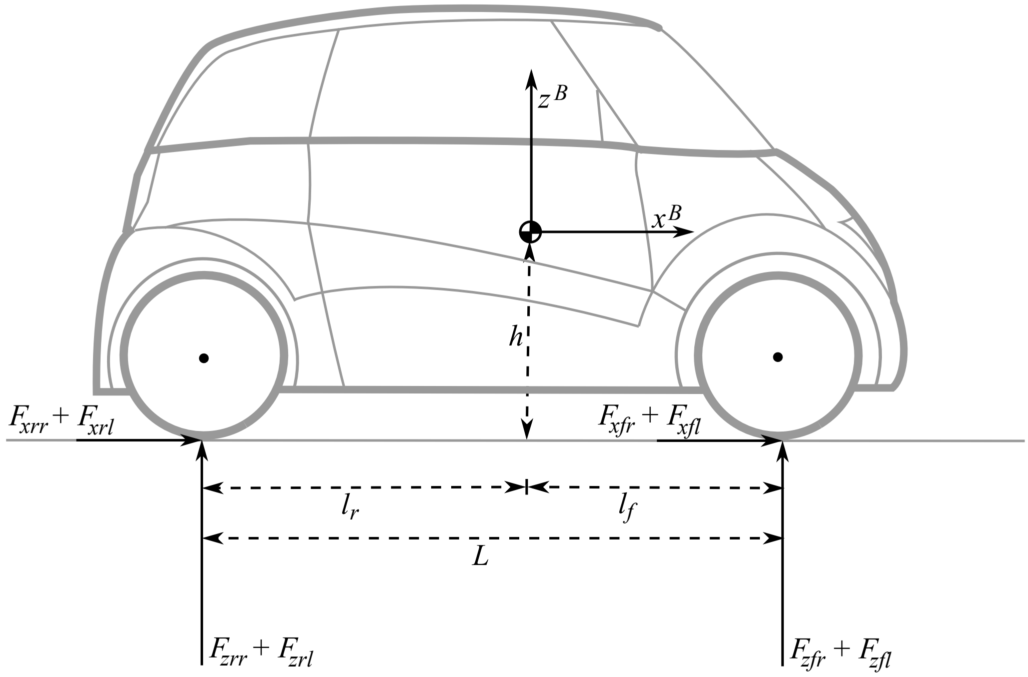

Figure 3.13: Forces acting in the x^B and z^B directions.

The resulting expressions for the distribution of the normal force between the front and rear wheels are:

$$F_{zrr} + F_{zrl} = F_{zr} = \frac{l_f \cdot m \cdot g}{L} + \frac{h \cdot m}{L} (\ddot{x} - \dot{\psi} \cdot \dot{y}) \tag{3.32}$$

and

$$F_{zfr} + F_{zfl} = F_{zf} = \frac{l_r \cdot m \cdot g}{L} - \frac{h \cdot m}{L} (\ddot{x} - \dot{\psi} \cdot \dot{y}) \tag{3.33}$$

Equations (3.32) and (3.33) also contain a static and a dynamic term. It is observed that the static load $m \cdot g$ is distributed unequally between the front and rear wheels, because the vehicle is asymmetric through the $y^B z^B$-plane (as $l_r \neq l_f$). The dynamic load is influenced by the longitudinal acceleration. It transfers load from the front wheels to the rear wheels when the vehicle accelerates and from the rear wheels to the front wheels when braking.

The dynamic loads stated in equation (3.32) and (3.33) are shared equally between the left and right wheels as they balance torque around the lateral vehicle axis only.

3.7.3 Total Normal Force Distribution

The static and dynamic normal force at each wheel is thereby:

$$\begin{aligned}
F_{zfr} &= \underbrace{\frac{l_r \cdot m \cdot g}{2 \cdot L}}_{F_{stat,f}} - \underbrace{\frac{h \cdot m}{2 \cdot L}}_{\Delta_{a_x}} (\ddot{x} - \dot{\psi} \cdot \dot{y}) + \underbrace{\frac{h \cdot m}{2 \cdot l_w}}_{\Delta_{a_y}} (\ddot{y} + \dot{\psi} \cdot \dot{x}) \\
F_{zfl} &= \underbrace{\frac{l_r \cdot m \cdot g}{2 \cdot L}}_{F_{stat,f}} - \underbrace{\frac{h \cdot m}{2 \cdot L}}_{\Delta_{a_x}} (\ddot{x} - \dot{\psi} \cdot \dot{y}) - \underbrace{\frac{h \cdot m}{2 \cdot l_w}}_{\Delta_{a_y}} (\ddot{y} + \dot{\psi} \cdot \dot{x}) \\
F_{zrr} &= \underbrace{\frac{l_f \cdot m \cdot g}{2 \cdot L}}_{F_{stat,r}} + \underbrace{\frac{h \cdot m}{2 \cdot L}}_{\Delta_{a_x}} (\ddot{x} - \dot{\psi} \cdot \dot{y}) + \underbrace{\frac{h \cdot m}{2 \cdot l_w}}_{\Delta_{a_y}} (\ddot{y} + \dot{\psi} \cdot \dot{x}) \\
F_{zrl} &= \underbrace{\frac{l_f \cdot m \cdot g}{2 \cdot L}}_{F_{stat,r}} + \underbrace{\frac{h \cdot m}{2 \cdot L}}_{\Delta_{a_x}} (\ddot{x} - \dot{\psi} \cdot \dot{y}) - \underbrace{\frac{h \cdot m}{2 \cdot l_w}}_{\Delta_{a_y}} (\ddot{y} + \dot{\psi} \cdot \dot{x})
\end{aligned} \tag{3.34}$$

where Δ_{a_x} is the coefficient of load transfer due to longitudinal acceleration and Δ_{a_y} is the coefficient of load transfer due to lateral acceleration.

The forces and torques affecting the planar vehicle motion have now been described. The parameters introduced in the previous sections will now be quantified.

3.8 Parameter Variations

The dynamic model of the QBEAK vehicle involves both known (or measurable parameters) and unknown constant or varying parameters. The parameters listed in table 3.3 are considered constant independent of vehicle load or road condition.

Parameter and value	Description
$g = 9.82\ [m/s^2]$	Gravitational constant
$\rho = 1.2041\ [kg/m^3]$	Density of air
$L = 2.2\ [m]$	Longitudinal distance between the front and rear wheel axle
$l_w = 1.5\ [m]$	Track width
$A = 2.25\ [m^2]$	Frontal vehicle area
$n = 10.3675\ [\cdot]$	Gearing ratio between PMSM and wheel axle*
$J_{wf} = 2.5745\ [kg \cdot m^2]$	Mass moment of inertia of each front wheel and PMSM rotor*
$J_{wr} = 2.4583\ [kg \cdot m^2]$	Mass moment of inertia of each rear wheel
$b = 0.5175\ [N{\cdot}m{\cdot}s/rad]$	Viscous friction coefficient at wheel axle*
$T_{mj,max} = 198.02\ [N \cdot m]$	Maximum available motor torque
$\tau_m = 0.0023\ [s]$	Time constant of closed-loop PMSM torque control system
$\tau_b = 0.030\ [s]$	Time constant of closed-loop braking torque control system

Table 3.3: Constant parameters used in the dynamic vehicle model. Parameters marked by * have been determined experimentally - see Appendix A.

The road dependent parameters c_1, c_2, c_3 and c_{roll} are listed in table 3.1 and 3.2 respectively. The bounds on the parameters are listed in table 3.4.

Minimum value	Parameter	Maximum value
$c_{1,min} = 0.05\ [\cdot]$	c_1	$c_{1,max} = 1.1973\ [\cdot]$
$c_{2,min} = 6.4565\ [\cdot]$	c_2	$c_{2,max} = 306.39\ [\cdot]$
$c_{3,min} = 0\ [\cdot]$	c_3	$c_{3,max} = 0.6691\ [\cdot]$
$c_{roll,min} = 0.008\ [\cdot]$	c_{roll}	$c_{roll,min} = 0.3\ [\cdot]$

Table 3.4: Bounds on parameters that change according to the road condition.

A series of parameters depend on the vehicle load m. The vehicle load is allowed to vary between the weight of an empty vehicle with 1 battery module ($m = 450\ [kg]$) to the weight of a fully loaded vehicle ($m = 1050\ [kg]$). As the vehicle load changes so does the vehicle CoM which affects a variety of parameters. The position of the CoM has only been calculated for 3 different values of m - the previously mentioned values of $m = 450\ [kg]$ and $m = 1050\ [kg]$ as well as an intermediate situation with $m = 600\ [kg]$ corresponding to 6 battery modules and one passenger without baggage. These three values of m are used to determine three operating points in which the system can be modeled. The load dependent parameters are listed in table 3.5 for the three operating points.

Parameter	**Description**	**Value corresponding to** $m = 450\ [kg]$	**Value corresponding to** $m = 600\ [kg]$	**Value corresponding to** $m = 1050\ [kg]$
$J_z\ [kg \cdot m^2]$	Mass moment of inertia around z^B-axis	265.875	354.500	620.375
$l_r\ [m]$	Distance from rear wheel axle to CoM	1.2076	1.1000	0.8507
$l_f\ [m]$	Distance from front wheel axle to CoM	0.9924	1.1000	1.3493
$h\ [m]$	Distance from ground to CoM	0.5300	0.4960	0.5600
$r_{fr}\ [m]$	Distance from front right wheel coordinate system to CoM	1.2440	1.3314	1.5438
$r_{fl}\ [m]$	Distance from front left wheel coordinate system to CoM	1.2440	1.3314	1.5438
$r_{rr}\ [m]$	Distance from rear right wheel coordinate system to CoM	1.4215	1.3314	1.1341
$r_{rl}\ [m]$	Distance from rear left wheel coordinate system to CoM	1.4215	1.3314	1.1341
$\varepsilon_{fr}\ [rad]$	Angle between the y^B-axis and the line intersecting the front right wheel coordinate system and the CoM	0.9237	0.9724	1.0635
$\varepsilon_{fl}\ [rad]$	Angle between the x^B-axis and the line intersecting the front left wheel coordinate system and the CoM	0.6471	0.5984	0.5073
$\varepsilon_{rr}\ [rad]$	Angle between the x^B-axis and the line intersecting the rear right wheel coordinate system and the CoM	0.5558	0.5984	0.7226
$\varepsilon_{rl}\ [rad]$	Angle between the y^B-axis and the line intersecting the rear left wheel coordinate system and the CoM	1.0150	0.9724	0.8482

Table 3.5: Load dependent parameters.

Apart from the parameter variations caused by changing road and load conditions the following parameters are considered varying or uncertain:

- The drag coefficient c_D is not exactly known but is assumed to be bounded by $c_{D,min} \leq c_D \leq c_{D,max}$ given in table 3.6.
- The effective tire radius r is not exactly known as different tires can be mounted on the QBEAK vehicle and the tire inflation might change affecting the deflection of the tire. Again r is assumed to be bounded

by $r_{min} \leq r \leq r_{max}$ given in table 3.6.

Minimum value	Parameter	Maximum value
$c_{D,min} = 0.30\ [\cdot]$	c_D	$c_{D,max} = 0.40\ [\cdot]$
$r_{min} = 0.25\ [m]$	r	$r_{max} = 0.35\ [m]$

Table 3.6: Bounds on c_D and r.

With the given parameters quantified, the dynamic vehicle model can now be implemented in the MATLAB Simulink environment.

3.9 Matlab Simulink Model

The dynamic model derived in this chapter is implemented in the MATLAB Simulink environment. The Simulink model is used to simulate the dynamics of the vehicle in different driving and braking conditions. The performance of the slip controller (described in Section 5.2) is tested using the Simulink model as is the performance of friction force observer and friction curve estimator (described in Section 5.4 and 5.5 respectively).

The Simulink model is appended on a CD (see Appendix C). The file name is *Qbeak.mdl*
A block diagram of the model is shown in figure 3.14.

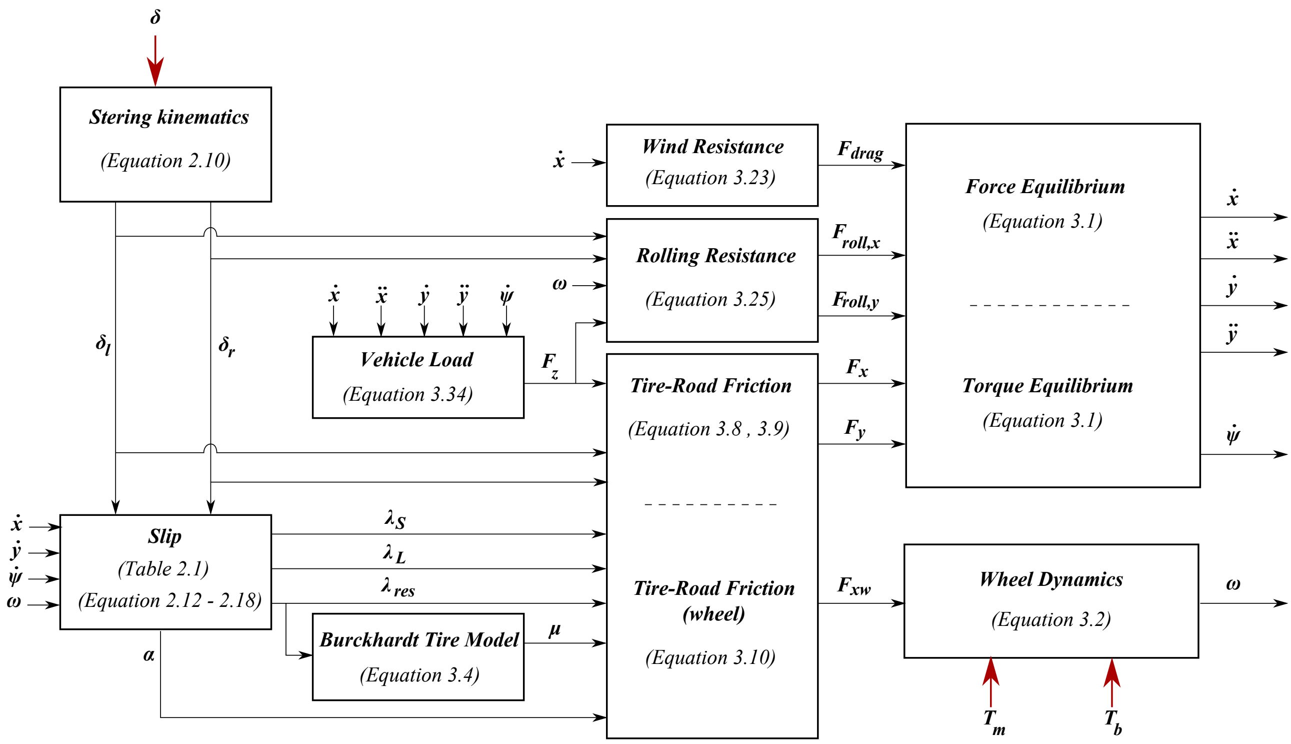

Figure 3.14: Block diagram of the MATLAB Simulink model. The red arrows indicate inputs to the model.

The model uses the 4th order Runge-Kutta based differential equation solver ODE-45 [2] with a variable step algorithm and a maximum step size of 0.001.
As the model is initialized the script *par_Qbeak.m* is run. This file loads the parameters necessary to run the model.

As the dynamic equations are implemented in the Simulink model this concludes the formulation of the dynamic model. The derivation of the vehicle dynamics in this chapter forms the basis of the following problem statement.

4 Problem Statement

A slip control system is to be designed based on the dynamic model of the QBEAK vehicle derived in Chapter 3. The control system will be designed to ensure that the requirements listed in the initiating problem statement (Section 1.5) are fulfilled.

The controller must be robust to variations in road conditions and vehicle load. Robustness must also be guaranteed in spite of the bounded uncertainties in the following parameters:

- The vehicle mass m.
- The tire radius r.
- The drag coefficient c_D.
- The rolling resistance coefficient c_{roll}.

listed in table 3.4, 3.5 and 3.6 in Section 3.8.

The slip controller should stabilize the slip at a reference value chosen to ensure an optimal trade-off between lateral and longitudinal tire-road friction.

5 Design of Slip Controller

The design of a slip controller is presented in this chapter. It is based on a simplification of the dynamic vehicle model derived in Chapter 3. A sliding mode control structure is proposed using a boundary layer around the sliding surface to reduce chattering. An anti wind-up scheme is proposed to avoid integrator wind-up. As part of the slip control system is a torque distribution system, a friction force observer and a friction curve estimator. These subsystems will be tested through simulations and experiments.

5.1 Simplified Longitudinal Model

The design of the slip controller is based on the assumption of longitudinal motion only, i.e. $\dot{y} = \ddot{y} = \dot{\psi} = \ddot{\psi} = \beta = \delta_j = \alpha_{ij} = 0$. The dynamic vehicle model given by equation (3.1) and (3.2) then reduces to the following 5 DoF system:

$$\begin{aligned} m \cdot \ddot{x} &= \underbrace{\left(F_{xfr} + F_{xfl} + F_{xrr} + F_{xrl}\right)}_{F_x} - \underbrace{\left(F_{roll,fr} + F_{roll,fl} + F_{roll,rr} + F_{roll,rl}\right)}_{F_{roll}} - F_{drag} \\ J_{wi} \cdot \dot{\omega}_{ij} &= T_{mj} - T_{bij} \cdot \mathrm{sign}(\omega_{ij}) - b \cdot \omega_{ij} - r \cdot F_{xwij} \end{aligned} \tag{5.1}$$

As the vehicle motion is purely longitudinal the friction forces in the direction of the vehicle longitudinal axis and wheel axes are equal, i.e. $F_{xij} = F_{xwij} = F_{zij} \cdot \mu_{Lij}$. The last equality indicates that all of the available friction lies in the direction of λ_{Lij} as $\lambda_{Sij} = 0$.

The model given by equation (5.1) is further simplified by assuming that the viscous torques developed at the wheel axles are negligible compared to the torques caused by the tractive forces, thus $b \cdot \omega_{ij} \approx 0$. Furthermore the tractive forces developed at the individual wheels are equal, i.e. only the wheel dynamics of one wheel is necessary to calculate the tractive forces.

Finally $\omega_{ij} \leq 0$ and $\dot{x} \leq 0$ as it is assumed that no slip control is necessary when reversing. The resulting simplified vehicle model is described by:

$$\dot{\omega}_{ij} = -\frac{r \cdot F_{xij}}{J_{wi}} + \frac{1}{J_{wi}} \cdot u_{ij} \tag{5.2}$$

and

$$\ddot{x} = \frac{2 \cdot F_{xij} - F_{roll} - F_{drag}}{m} \qquad \text{TCS} \tag{5.3}$$

$$\ddot{x} = \frac{4 \cdot F_{xij} - F_{roll} - F_{drag}}{m} \qquad \text{ABS} \tag{5.4}$$

The difference in the models considering TCS and ABS conditions is due to the fact that only 2 wheels supply tractive forces when TCS is used while all four wheels supply braking forces when ABS is used. Thus the total tractive force is twice the tractive force developed at a single wheel (F_{xij}) for TCS and four times the tractive force developed at a single wheel for ABS.
The input u_{ij} is the total torque input at the wheel axle:

$$\left.\begin{array}{rcl} u_{fj} & = & T_{mj} \\ u_{rj} & = & 0 \end{array}\right\}\text{TCS} \qquad \left.\begin{array}{rcl} u_{fj} & = & T_{mj}-T_{bfj} \\ u_{rj} & = & -T_{brj} \end{array}\right\}\text{ABS} \tag{5.5}$$

The output of the slip controller is a reference torque at each wheel axle, $u_{ij,ref}$. This torque must be supplied by the PMSMs, the brakes or both. The distribution of the torque between the actuators is treated in Section 5.3.

5.1.1 Slip Dynamics

The state variables in the simplified model given by equation (5.2) to (5.4) are $\dot{x}$ and ω_{ij}. Since the slip dynamics are of interest when designing a slip controller the states of the model are changed. The following expressions for λ_{Lij}, ω_{ij}, $\dot{\lambda}_{Lij}$ and $\dot{\omega}_{ij}$ will be used to express the simplified model in the state variables λ_{Lij} and $\dot{x}$ - these expressions are derived from the longitudinal slip equations given in table 2.1:

TCS $(\omega_{ij} > \dot{x})$	**ABS** $(\omega_{ij} \leq \dot{x})$
$\lambda_{Lij} = 1-\frac{\dot{x}}{\omega_{ij}\cdot r}$	$\lambda_{Lij} = \frac{\omega_{ij}\cdot r}{\dot{x}}-1$
$\omega_{ij} = \frac{\dot{x}}{r}\frac{1}{1-\lambda_{Lij}}$	$\omega_{ij} = \frac{\dot{x}}{r}(1+\lambda_{Lij})$
$\dot{\lambda}_{Lij} = \frac{\dot{x}}{r\cdot\omega_{ij}^2}\cdot\dot{\omega}_{ij}-\frac{1}{r\cdot\omega_{ij}}\cdot\ddot{x}$	$\dot{\lambda}_{Lij} = \frac{r}{\dot{x}}\cdot\dot{\omega}_{ij}-\frac{\omega_{ij}\cdot r}{\dot{x}^2}\cdot\ddot{x}$
$\dot{\omega}_{ij} = \frac{r\cdot\omega_{ij}^2}{\dot{x}}\cdot\dot{\lambda}_{Lij}+\frac{\omega_{ij}}{\dot{x}}\cdot\ddot{x}$	$\dot{\omega}_{ij} = \frac{\dot{x}}{r}\dot{\lambda}_{Lij}+\frac{\omega_{ij}}{\dot{x}}\cdot\ddot{x}$

Combining the above equations with equation (5.2), (5.3) and (5.4) results in the following models describing the slip dynamics.

TCS

$$\dot{\lambda}_{Lij} = -\frac{1}{\dot{x}}\cdot\left(\frac{1-\lambda_{Lij}}{m}\cdot(2\cdot F_{xij}-F_{roll}-F_{drag})+\frac{r^2\cdot(1-\lambda_{Lij})^2}{J_{wi}}\cdot F_{xij}\right)+\frac{r\cdot(1-\lambda_{Lij})^2}{J_{wi}\cdot\dot{x}}\cdot u_{ij} \tag{5.6}$$

ABS

$$\dot{\lambda}_{Lij} = -\frac{1}{\dot{x}} \cdot \left(\frac{1+\lambda_{Lij}}{m} \cdot (4 \cdot F_{xij} - F_{roll} - F_{drag}) + \frac{r^2}{J_{wi}} \cdot F_{xij} \right) + \frac{r}{J_{wi} \cdot \dot{x}} \cdot u_{ij} \tag{5.7}$$

The state variables $\dot{x}$ and λ_{Lij} can be assumed to evolve on significantly different time scales due to the large difference in inertia of the wheels and the vehicle [35, p.26], [18]. Thus $\dot{x}$ can be treated as a slowly varying parameter with negligible dynamics compared to λ_{Lij}. Equation (5.3) and (5.4) will therefore be neglected in the analysis and control design.

It is noted that the slip dynamics described by equation (5.6) and (5.7) become infinitely fast as $\dot{x} \to \infty$. Thus, it is expected that the slip becomes difficult to control at low vehicle velocities due to sampling effects and dynamics of the controller and actuators.

The open-loop stability of the slip dynamics is investigated in the next section.

5.1.1.1 Open-loop Stability

The stability of the slip dynamics is investigated by analyzing the equilibrium points of the system. The equilibrium points λ^*_{Lfj} of interest are characterized by $\dot{\lambda}_{Lfj} = 0$, i.e. constant slip [38, p.10]. Treating F_{roll} and F_{drag} as disturbance forces allows equation (5.6) and (5.7) to be rewritten as:

$$\dot{\lambda}_{Lij} = -\frac{r \cdot (1-\lambda_{Lij})^2}{J_{wi} \cdot \dot{x}} \cdot (\Psi_{TCS} - u_{ij}) \qquad \text{for TCS} \tag{5.8}$$

and:

$$\dot{\lambda}_{Lij} = -\frac{r}{J_{wi} \cdot \dot{x}} \cdot (\Psi_{ABS} - u_{ij}) \qquad \text{for ABS} \tag{5.9}$$

with Ψ_{TCS} and Ψ_{ABS} given as:

$$\Psi_{TCS} = \left(2 \cdot \frac{J_{wi}}{m \cdot r} \cdot \frac{1}{1-\lambda_{Lij}} + r \right) \cdot F_{xij} \tag{5.10}$$

$$\Psi_{ABS} = \left(4 \cdot \frac{J_{wi}}{m \cdot r} (1+\lambda_{Lij}) + r \right) \cdot F_{xij} \tag{5.11}$$

Thus the equilibrium points ($\dot{\lambda}_{Lij} = 0$) are given by the intersection of u_{ij} and Ψ_{TCS} or Ψ_{ABS} and are thereby independent of $\dot{x}$.

Ψ_{TCS} and Ψ_{ABS} can be plotted as functions of λ_{Lij} by assuming that $F_{zij} = F_{stat,ij}$ and noting that $F_{xij} = F_{zij} \cdot \mu_{Lij}$ with μ_{Lij} given as:

$$\mu_{Lij} = \text{sign}(\lambda_{Lij}) \cdot \left[c_1 \cdot \left(1 - e^{-c_2 \cdot |\lambda_{Lij}|}\right) - c_3 \cdot |\lambda_{Lij}| \right] \tag{5.12}$$

as $\lambda_{Sij} = 0 \Rightarrow \lambda_{res,ij} = |\lambda_{Lij}|$.

Figure 5.1 shows plots of Ψ_{TCS} and Ψ_{ABS} for different road surfaces. The plots are made for $F_{zij} = F_{stat,f} = \frac{l_r \cdot m \cdot g}{2 \cdot L}$, $J_{wi} = J_{wf}$ and $m = 600$ $[kg]$ which approximately corresponds to the QBEAK vehicle with one driver and no baggage.

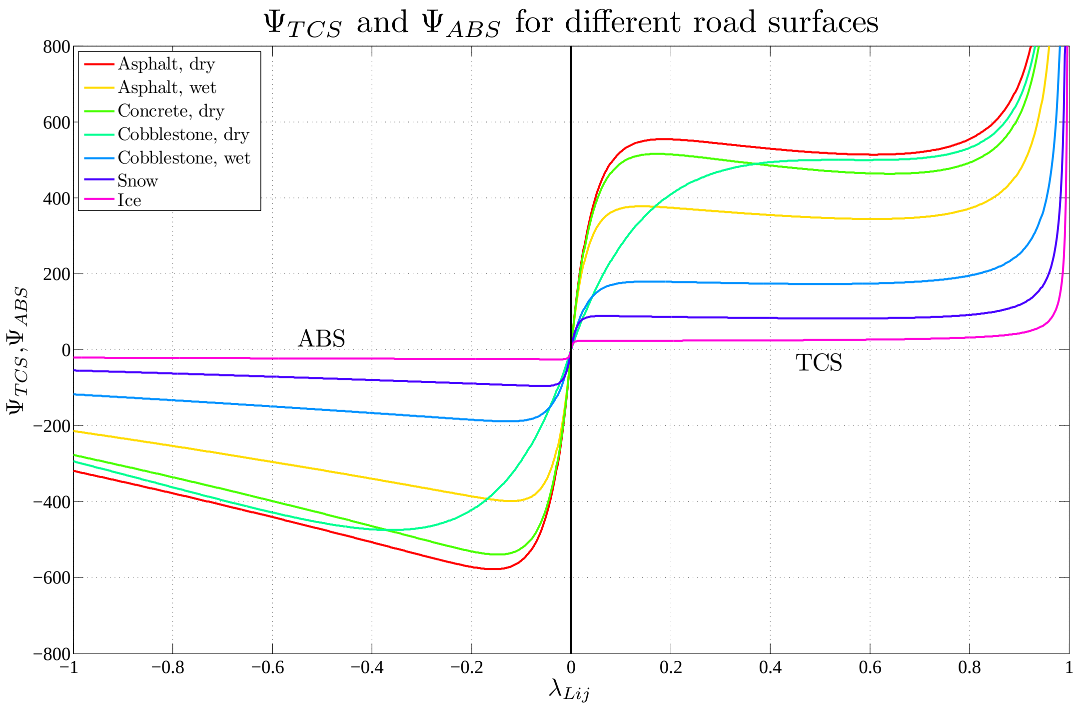

Figure 5.1: Ψ_{TCS} and Ψ_{ABS} for different road surfaces.

The following is observed from the plot of Ψ_{TCS} and Ψ_{ABS} in figure 5.1:

- As the equilibrium points of the system are found by the intersection of u_{ij} and Ψ_{TCS} or Ψ_{ABS} the system can have one, two or three equilibrium points for TCS and zero, one or two equilibrium points for ABS.
- As $u_{ij} = T_{mj}$ for TCS and $|T_{mj}| \leq T_{mj,max} = 198.02$ $[N \cdot m]$ the system can only achieve slip values near λ_{max} at low friction road surfaces (ice, snow and wet cobblestone).
- Slip values of 1 are unobtainable as $\Psi_{TCS} \to \infty$ for $\lambda_{Lij} \to 1$. The reason for this is that $\lambda_{Lij} = 1 \Rightarrow \omega_{ij} = \infty$ for $\dot{x} \neq 0$ (according to the slip definition in table 2.1).

The open-loop stability of the equilibrium points can be determined by inserting the equilibrium input $u_{ij}^* = \Psi_{TCS}$ or $u_{ij}^* = \Psi_{ABS}$ into equation (5.8) or (5.9) respectively and plotting the phase portrait assuming $\dot{x}$ is constant. Two situations will be considered; acceleration on wet cobblestone with constant input $u^*_{ij} = 176$ $[N \cdot m]$ and braking on wet cobblestone with constant input $u^*_{ij} = -176$ $[N \cdot m]$. The first situation corresponds to 3 equilibrium points and the second situation corresponds to 2 equilibrium points. The stability of the equilibrium points is determined from the phase portraits in figure 5.2 and 5.3.

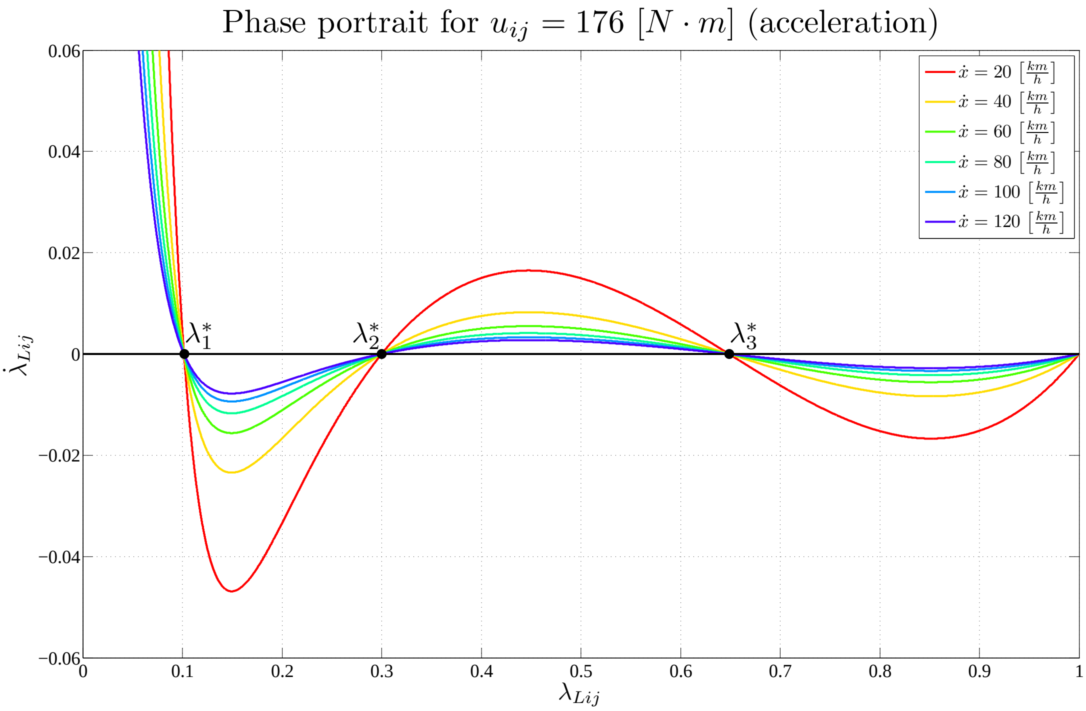

Figure 5.2: Phase portrait for $u^*_{ij} = 176$ $[N \cdot m]$.

It is seen from the phase portrait in figure 5.2 that the system has three equilibrium points $\lambda^*_1 \approx 0.1$, $\lambda^*_2 \approx 0.3$ and $\lambda^*_3 \approx 0.65$. The slip corresponding to maximum friction is $\lambda_{max} = 0.14$, i.e. λ^*_2 and λ^*_3 are located beyond the peak of the friction curve.
The following observations regarding the stability of the three equilibrium points are made:

- The stability of the equilibrium points is independent of the value of $\dot{x}$.
- The absolute value of the tangent to the trajectories increases as $\dot{x}$ decreases, i.e. the dynamics become faster at lower vehicle velocities.
- λ^*_1 is a stable equilibrium as the slope of the trajectories are negative in this point. As λ^*_1 is located at a slip value below that of the friction curve peak, small increases of the slip beyond this singular point also increases the friction force acting on the wheel, and thus forces the slip back to the equilibrium value. A similar argument holds for small decreases in slip values.
- λ^*_2 is an unstable equilibrium as the slope of the trajectories are positive in this point. λ^*_2 is located at a slip value beyond that of the friction curve peak. Thus small increases in slip beyond this equilibrium decreases the friction force acting on the wheel which further increases the slip. The trajectories will therefore leave the equilibrium point.

- λ_3^* is a stable equilibrium as the slope of the trajectories are negative in this point. This equilibrium point is also located at a slip value beyond that of the friction curve peak. However, as $\Psi_{TCS} \to \infty$ for $\lambda_{Lij} \to 1$ the system prevents itself from slip values near $\lambda_{Lij} = 1$.
- The phase portrait indicates that $\lambda_{Lij} = 1$ is an equilibrium point. However, this point would yield $\dot{x} = 0$ or $u_{ij} = \infty$. Values for which the system is not defined.

A similar analysis can be made of the phase portrait corresponding to $u_{ij}^* = -176\ [N \cdot m]$ which is plotted in figure 5.3.

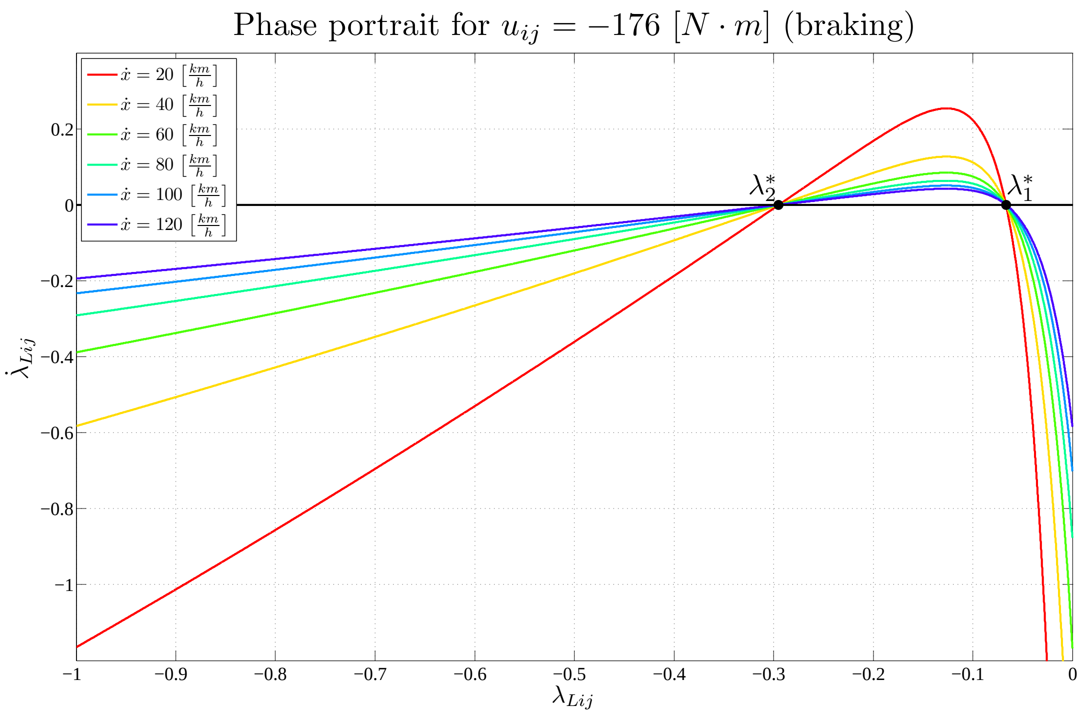

Figure 5.3: Phase portrait for $u_{ij}^* = -176\ [N \cdot m]$.

The phase portrait indicates that the system has 2 equilibrium points; $\lambda_1^* \approx -0.067$ and $\lambda_1^* \approx -0.3$, thus $|\lambda_1^*| < |\lambda_{max}| < |\lambda_2^*|$ where λ_{max} is the slip corresponding to a maximum absolute friction value. It is seen that the equilibrium point located at a lower absolute slip value than the peak of the friction curve is stable while the equilibrium point located at a higher absolute value than the peak is unstable. The explanation is similar to the case of acceleration. However, the wheels are not prevented from locking during braking as the trajectories do not reach a stable equilibrium if the absolute slip reaches values beyond $|\lambda_{max}|$.
Again it is noted that $\dot{x}$ does not affect the stability of the equilibrium points.

Based on the analysis of the equilibrium points for acceleration and braking it is concluded that a slip control system is needed to stabilize the slip near λ_{max} - for both acceleration and braking situations - as this point separates the stable part of the λ_{Lij}-$\dot{\lambda}_{Lij}$ domain from the unstable part.

It must be noted that the forces due to drag and rolling resistance as well as the dynamics of $\dot{x}$ have been neglected in the analysis of the equilibrium points. In real driving situations a constant slip cannot be maintained for a constant input u_{ij} as changing velocity would result in changing drag force and viscous friction torque which would have to be compensated for by u_{ij}.

A final motivation for designing a closed-loop slip control system is the increasing robustness to external disturbances and parameter variations such a system can ensure.

5.2 Controller Design

The slip controllers used as TCS and ABS are developed in this section based on the reduced nonlinear model of the slip dynamics given by equation (5.6) and (5.7). It is noted that both systems are nonlinear in the state λ_{Lij} and the slowly varying parameter $\dot{x}$ but linear in the input u_{ij} and can be written in the canonical form:

$$\dot{\lambda}_{ij} = f(\lambda_{ij}, \dot{x}) + g(\lambda_{ij}, \dot{x}) \cdot u_{ij} \tag{5.13}$$

The notation of the system dynamics given by equation (5.13) makes it possible to design the slip controller simultaneously for TCS and ABS.

The system given by (5.13) is subject to the parameter uncertainties stated in Section 3.8 and the unknown tire-road friction force F_{xij}. The friction force is affected by slip ratio, side slip and changing road condition as well as variations of the normal force caused by acceleration in the longitudinal and lateral directions. The fast dynamics of F_{zij} makes the friction force unsuitable for adaptive compensation while the large uncertainty in μ_{ij} makes it unsuitable for robust compensation as a very high loop gain would be necessary. A friction force observer is therefore designed to estimate F_{xij} and the controller design will be carried out with the assumption that F_{xij} is measurable. The friction force observer is described in Section 5.4.

A sliding mode controller for the dynamics given by (5.13) is proposed in this project as this controller can be made robust to bounded parameter variations and unmodeled dynamics [38, p.306].

The controller design will be carried out by initially designing a sliding surface defining the desired closed-loop behavior of the system. A stabilizing control law will then be derived assuming no parametric uncertainties. The control law is finally extended to be robust to the parameter variations.

5.2.1 Design of Sliding Surface

The idea behind sliding mode control is to formulate a scalar function s of the system tracking error and designing a control law that forces this function to zero in spite of disturbances and parameter uncertainties. The case of $s = 0$ represents a surface in the phase plane and is therefore referred to as a sliding surface or sliding manifold. As the system is always forced onto the sliding surface, the trajectories will "slide" along $s = 0$ with the dynamics determined by the definition of the sliding surface. Thus the system experiences a reaching phase in which the system is forced onto $s = 0$ and a sliding phase where the dynamics are determined by $s = 0$ [38, p.286-287].

The design of a sliding mode controller can be divided into two parts; the design of the sliding surface and the design of a discontinuous control law that forces the system trajectory towards this sliding surface.

It is widely used to formulate s as a weighted function of the system state errors with the weighting terms chosen such that $s = 0$ is a Hurwitz polynomial (as an example see [38, p.278] for a general guide to designing s). For systems of second or higher order this would result in exponential convergence to zero of the system state errors. However, as the system under consideration is first order, the error function would simply be $s = \tilde{\lambda}_{Lij}$ where $\tilde{\lambda}_{Lij} = \lambda_{Lij} - \lambda_{Lij,ref}$. Thus $s = 0$ represents a vertical line in the phase plane and does not yield exponential dynamics. However, if $s = \tilde{\lambda}_{Lij}$, then $s = 0$ would immediately result in zero state error. The problem is that the dynamics outside of the sliding surface are difficult to control as only asymptotic convergence normally can be guaranteed. For the first order case this would result in a simple bang-bang control only acting on the sign of the error and not its magnitude. The reaching time (and thus the convergence rate) would then be determined by the gain of the control discontinuity along $s = 0$.

In this project a modification of the sliding surface is proposed. The error function s is chosen as a weighted sum of the state error and the integrated state error. This is known as integral sliding mode control and has the advantage that the sliding surface can be designed to yield exponential error convergence when $s = 0$ and can also be designed to eliminate the reaching phase completely, thus achieving exponential error convergence even if $\tilde{\lambda}_{Lij}(0) \neq 0$ [38, p.286-287].

The error function will be designed as:

$$\boxed{s = \tilde{\lambda}_{Lij}(t) + \eta \cdot \int_0^t \tilde{\lambda}_{Lij}(\tau)\, d\tau - \tilde{\lambda}_{Lij}(0) \qquad (5.14)}$$

where η is a positive constant determining the convergence rate and τ is a dummy variable used for integration. The term $\tilde{\lambda}_{Lij}(0)$ shifts the sliding surface in the phase plane to ensure that $s(0) = 0$, i.e. the system trajectory is initially located at the sliding surface and the reaching phase is eliminated for all initial conditions.

It is seen that when $s = 0$, equation (5.14) reduces to:

$$\tilde{\lambda}_{Lij}(t) + \eta \cdot \int_0^t \tilde{\lambda}_{Lij}(\tau)\, d\tau = \tilde{\lambda}_{Lij}(0)$$

The dynamics of the system is found by a change of variables, such that $z(t) = \int_0^t \tilde{\lambda}_{Lij}(\tau)\, d\tau$, which yields:

$$\dot{z}(t) + \eta \cdot z(t) = \dot{z}(0) \qquad (5.15)$$

The dynamics of $z(t)$ is then the solution of the first order inhomogeneous ODE given by equation (5.15) with constant input $\dot{z}(0)$. The solution is given as [31, p.116-119]:

$$z(t) = z(0) \cdot e^{-\eta \cdot t} + \frac{1}{\eta} \cdot \dot{z}(0) \cdot \left(1 - e^{-\eta \cdot t}\right) \tag{5.16}$$

Expressing equation (5.16) in the original variable $\int_0^t \tilde{\lambda}_{Lij}(\tau)\, d\tau$ yields:

$$\begin{aligned} \int_0^t \tilde{\lambda}_{Lij}(\tau)\, d\tau &= \int_0^0 \tilde{\lambda}_{Lij}(\tau)\, d\tau \cdot e^{-\eta \cdot t} + \frac{1}{\eta} \cdot \tilde{\lambda}_{Lij}(0) \cdot \left(1 - e^{-\eta \cdot t}\right) \\ &= \frac{1}{\eta} \cdot \tilde{\lambda}_{Lij}(0) \cdot \left(1 - e^{-\eta \cdot t}\right) \end{aligned} \tag{5.17}$$

Thus the integrated error converges to a nonzero constant for nonzero initial slip error. The variable of interest is however not the integrated error but the slip error. The slip error dynamics are given by the derivative of equation (5.17):

$$\tilde{\lambda}_{Lij} = \tilde{\lambda}_{Lij}(0) \cdot e^{-\eta \cdot t} \tag{5.18}$$

It is seen that $\int_0^t \tilde{\lambda}_{Lij}(\tau)\, d\tau \to \frac{1}{\eta} \cdot \tilde{\lambda}_{Lij}(0)$ and $\tilde{\lambda}_{Lij} \to 0$ as $t \to \infty$ with exponential rate η.

The dynamics of the closed-loop slip control system therefore acts as a first order low pass filter with time constant τ given as:

$$\tau = \frac{1}{\eta} \tag{5.19}$$

The 2 % settling time t_{settle} of the closed-loop system is:

$$t_{settle} = -\frac{\ln(0.02)}{\eta} \approx 3.9 \cdot \tau \tag{5.20}$$

The error function given by equation (5.14) will be used in the slip control systems for both accelerating and braking the vehicle.

A control law that forces the system trajectories onto the sliding surface in spite of uncertainties in $f(\lambda_{Lij}, \dot{x})$ and $g(\lambda_{Lij}, \dot{x})$ will be derived in the following section.

5.2.2 Design of Robust Control Law

Initially the control law will be designed assuming no parameter uncertainty. The control law is then modified to take into account that $f(\lambda_{Lij}, \dot{x})$ and $g(\lambda_{Lij}, \dot{x})$ are unknown but with known bounds. In the following $f := f(\lambda_{Lij}, \dot{x})$ and $g := g(\lambda_{Lij}, \dot{x})$ for simplicity. The system dynamics are then written as:

$$\dot{\lambda}_{Lij} = f + g \cdot u_{ij}$$

With s defined as in equation (5.14) the time derivative of s is:

$$\dot{s} = \dot{\tilde{\lambda}}_{Lij} + \eta \cdot \tilde{\lambda}_{Lij}$$

$$= \dot{\lambda}_{Lij} - \dot{\lambda}_{Lij,ref} + \eta \cdot \tilde{\lambda}_{Lij}$$

In this case $\dot{\lambda}_{Lij,ref} = 0$ resulting in:

$$\dot{s} = \dot{\lambda}_{Lij} + \eta \cdot \tilde{\lambda}_{Lij}$$

$$= f + g \cdot u_{ij} + \eta \cdot \tilde{\lambda}_{Lij} \tag{5.21}$$

A stabilizing control input is found by formulating a Lyapunov function candidate V and choosing u_{ij} such that $\dot{V}$ is negative definite. The Lyapunov function candidate V is chosen as the positive definite function:

$$V = \frac{1}{2} \cdot s^2 \tag{5.22}$$

which satisfies the condition $V \to \infty$ for $|s| \to \infty$.

The time derivative of V is:

$$\dot{V} = \dot{s} \cdot s = \left(f + g \cdot u_{ij} + \eta \cdot \tilde{\lambda}_{Lij} \right) \cdot s \tag{5.23}$$

It is seen that if u_{ij} is chosen as:

$$u_{ij} = -\frac{f + \eta \cdot \tilde{\lambda}_{Lij} + k \cdot \text{sign}(s)}{g} \tag{5.24}$$

then equation (5.23) reduces to:

$$\dot{V} = -k \cdot \text{sign}(s) \cdot s = -k \cdot |s| \tag{5.25}$$

Which is negative definite. Thus V is a Lyapunov function and $s = 0$ is a globally asymptotically stable equilibrium, i.e. the system trajectories asymptotically converge to $s = 0$ as $t \to \infty$ [38, p.65]. The system trajectories are therefore forced to slide along $s = 0$, and the error dynamics are then given by equation (5.18).

It is observed that the control input given by equation (5.24) consists of three terms:

- The inverse dynamics of the plant.
- A term which makes the dynamics of the plant equal to that of $s = 0$.
- A discontinuous term that forces the system trajectories onto the sliding surface.

It will now be shown that the control law given by equation (5.24) can be extended to be robust to bounded uncertainties in f and g by a proper choice of k. Thus the discontinuous term keeps the system on the sliding surface in spite of model uncertainties. It is emphasized that k is allowed to be a function of the system states and time.

It is assumed that f and g are not exactly known but estimated as $\hat{f}$ and $\hat{g}$ [38, p.287]. The estimation error on f is assumed to be bounded by some known function F such that:

$$|\hat{f} - f| \leq F \tag{5.26}$$

It is furthermore assumed that bounds on g are known and satisfy:

$$0 < g_{min} \leq g \leq g_{max}$$

As the control input u_{ij} is multiplied by g it is reasonable to choose the estimate of g as:

$$\hat{g} = \sqrt{g_{min} \cdot g_{max}}$$

The bounds on the estimation error can then be formulated as:

$$\begin{gathered} \beta^{-1} \leq \frac{\hat{g}}{g} \leq \beta \\ \text{or} \\ \beta^{-1} \leq \frac{g}{\hat{g}} \leq \beta \end{gathered} \tag{5.27}$$

with β given as:

$$\beta = \sqrt{\frac{g_{max}}{g_{min}}} \tag{5.28}$$

By approximating the control law given in equation (5.24) by the estimated inverse dynamics:

$$\boxed{u_{ij} = -\frac{\hat{f} + \eta \cdot \tilde{\lambda}_{Lij} + k \cdot \text{sign}(s)}{\hat{g}}} \tag{5.29}$$

the derivative of V is expressed as:

$$\begin{aligned} \dot{V} &= \left(f - g \cdot \frac{\hat{f} + \eta \cdot \tilde{\lambda}_{Lij} + k \cdot \text{sign}(s)}{\hat{g}} + \eta \cdot \tilde{\lambda}_{Lij} \right) \cdot s \\ &= \left(f - \frac{g}{\hat{g}} \cdot \hat{f} + \left(1 - \frac{g}{\hat{g}}\right) \cdot \eta \cdot \tilde{\lambda}_{Lij} - \frac{g}{\hat{g}} \cdot k \cdot \text{sign}(s) \right) \cdot s \end{aligned} \tag{5.30}$$

Rewriting equation (5.30) using that $f = (f - \hat{f}) + \hat{f}$:

$$\dot{V} = \left((f - \hat{f}) + \left(1 - \frac{g}{\hat{g}}\right) \cdot \left(\hat{f} + \eta \cdot \tilde{\lambda}_{Lij}\right) - \frac{g}{\hat{g}} \cdot k \cdot \text{sign}(s) \right) \cdot s \tag{5.31}$$

In order to make $\dot{V}$ negative definite the following inequality must be satisfied:

$$\begin{aligned} k &\geq \frac{\hat{g}}{g} \cdot \left| (f - \hat{f}) + \left(1 - \frac{g}{\hat{g}}\right) \cdot \left(\hat{f} + \eta \cdot \tilde{\lambda}_{Lij}\right) \right| \qquad \Rightarrow \\ k &\geq \frac{\hat{g}}{g} \cdot \left| f - \hat{f} \right| + \left(\frac{\hat{g}}{g} - 1\right) \cdot \left| \hat{f} + \eta \cdot \tilde{\lambda}_{Lij} \right| \end{aligned} \tag{5.32}$$

It is seen that equation (5.32) is satisfied if k is chosen as:

$$\boxed{k \geq \beta \cdot F + (\beta - 1) \cdot \left| \hat{f} + \eta \cdot \tilde{\lambda}_{Lij} \right|} \tag{5.33}$$

This results in:

$$\dot{V} \leq -|s| \tag{5.34}$$

Which makes $\dot{V}$ negative definite. Thus V is a Lyapunov function and $s = 0$ is a globally asymptotically stable equilibrium, i.e. the system trajectories asymptotically converge to $s = 0$ as $t \to \infty$ [38, p.65]. Thus, the system trajectories are forced to slide along $s = 0$, and the error dynamics are then given by equation (5.18).

It is seen that the control law given by equation (5.29) and (5.33) now uses the approximated inverse dynamics. The gain of the discontinuity is increased to account for the parametric uncertainties.

So far the control law has been derived without distinguishing between the driving and braking situations. In the following section the two situations will be treated independently when $\hat{f}$, F, $\hat{g}$ and β are determined.

5.2.3 Parametric Uncertainties

Inserting the expressions for F_{roll} and F_{drag} into equation (5.6) og (5.7) yields:

TCS

$$\dot{\lambda}_{Lij} = \underbrace{-\frac{1}{\dot{x}} \cdot \left(\frac{1-\lambda_{Lij}}{m} \cdot \left(2 \cdot F_{xij} - m \cdot g \cdot c_{roll} - \frac{\rho}{2} \cdot A \cdot c_D \cdot \dot{x}^2 \right) + \frac{r^2 \cdot (1-\lambda_{Lij})^2}{J_{wi}} \cdot F_{xij} \right)}_{f} + \underbrace{\frac{r \cdot (1-\lambda_{Lij})^2}{J_{wi} \cdot \dot{x}}}_{g} \cdot u_{ij}$$

ABS

$$\dot{\lambda}_{Lij} = \underbrace{-\frac{1}{\dot{x}} \cdot \left(\frac{1+\lambda_{Lij}}{m} \cdot \left(4 \cdot F_{xij} - m \cdot g \cdot c_{roll} - \frac{\rho}{2} \cdot A \cdot c_D \cdot \dot{x}^2 \right) + \frac{r^2}{J_{wi}} \cdot F_{xij} \right)}_{f} + \underbrace{\frac{r}{J_{wi} \cdot \dot{x}}}_{g} \cdot u_{ij}$$

Uncertainties in F_{xij} are neglected as an observer will be designed to estimate this force. The parametric uncertainties affecting the system then reduces to uncertainties in the following parameters: m, r, c_{roll} and c_D. These parameters are assumed to be bounded by the minimum and maximum values given in Section 3.8 and an estimate of the bounds will be determined as the mean of the maximum and minimum values resulting in:

Minimum value	Estimate	Maximum value	Maximum deviation
$m_{min} = 450$ $[kg]$	$\hat{m} = 750$ $[kg]$	$m_{max} = 1050$ $[kg]$	$\bar{m} = 300$ $[kg]$
$r_{min} = 0.25$ $[m]$	$\hat{r} = 0.30$ $[m]$	$r_{max} = 0.35$ $[m]$	$\bar{r} = 0.05$ $[m]$
$c_{D,min} = 0.30$ $[\cdot]$	$\hat{c}_D = 0.35$	$c_{D,max} = 0.40$ $[\cdot]$	$\bar{c}_D = 0.05$ $[\cdot]$
$c_{roll,min} = 0.008$ $[\cdot]$	$\hat{c}_{roll} = 0.154$ $[\cdot]$	$c_{roll,max} = 0.3$ $[\cdot]$	$\bar{c}_{roll} = 0.146$ $[\cdot]$

Table 5.1: Uncertainty bounds and estimates of m, r, c_D and c_{roll}.

The maximum deviations given in table 5.1 is the maximum error of the parameter estimate given the bounded uncertainties. These quantities are used to determine the estimated dynamics $\hat{f}$ and $\hat{g}$ and the estimation error bounds F and β introduced in Section 5.2.2.

$\hat{f}$, $\hat{g}$, F and β are listed in table 5.2.

TCS	$\hat{f} = -\frac{1}{\dot{x}} \cdot \left(\frac{1-\lambda_{Lij}}{\hat{m}} \cdot \left(2 \cdot F_{xij} - \hat{m} \cdot g \cdot \hat{c}_{roll} - \frac{\rho}{2} \cdot A \cdot \hat{c}_D \cdot \dot{x}^2\right) + \frac{\hat{r}^2 \cdot (1-\lambda_{Lij})^2}{J_{wi}} \cdot F_{xij} \right)$
	$F = \frac{1}{\dot{x}} \cdot \left(\lvert 1-\lambda_{Lij} \rvert \cdot \left(2 \cdot \lvert F_{xij} \rvert \cdot \frac{\bar{m}}{\hat{m} \cdot m_{min}} + g \cdot \bar{c}_{roll} + \frac{\rho}{2} \cdot A \cdot \dot{x}^2 \cdot \frac{c_{D,max} \cdot \hat{m} + \hat{c}_D \cdot m_{max}}{\hat{m} \cdot m_{min}}\right)\right)$
	$\hat{g} = \sqrt{r_{min} \cdot r_{max}} \cdot \frac{(1-\lambda_{Lij})^2}{J_{wi} \cdot \dot{x}}$
	$\beta = \sqrt{\frac{r_{max}}{r_{min}}}$
ABS	$\hat{f} = -\frac{1}{\dot{x}} \cdot \left(\frac{1+\lambda_{Lij}}{\hat{m}} \cdot \left(4 \cdot F_{xij} - \hat{m} \cdot g \cdot \hat{c}_{roll} - \frac{\rho}{2} \cdot A \cdot \hat{c}_D \cdot \dot{x}^2\right) + \frac{\hat{r}^2}{J_{wi}} \cdot F_{xij} \right)$
	$F = \frac{1}{\dot{x}} \cdot \left(\lvert 1+\lambda_{Lij} \rvert \cdot \left(4 \cdot \lvert F_{xij} \rvert \cdot \frac{\bar{m}}{\hat{m} \cdot m_{min}} + g \cdot \bar{c}_{roll} + \frac{\rho}{2} \cdot A \cdot \dot{x}^2 \cdot \frac{c_{D,max} \cdot \hat{m} + \hat{c}_D \cdot m_{max}}{\hat{m} \cdot m_{min}}\right)\right)$
	$\hat{g} = \frac{\sqrt{r_{min} \cdot r_{max}}}{J_{wi} \cdot \dot{x}}$
	$\beta = \sqrt{\frac{r_{max}}{r_{min}}}$

Table 5.2: Estimated dynamics and estimation error bounds.

All the terms in the control law given by equation (5.29) and (5.33) have now been determined and the slip controller can be discretized and implemented in the MATLAB Simulink model described in Section 3.9. The control law is slightly modified in the following sections to account for discretization effects and integrator wind-up.

5.2.4 Chattering

As the inverse dynamics used in the control law is only an approximation of the true inverse dynamics and the system is subject to disturbances, the trajectories will only stay on $s = 0$ due to the control discontinuity. When the system is implemented in a digital controller, the trajectories will chatter across $s = 0$ resulting in high control effort and oscillations in the system response. The magnitude of these oscillations are dependent on sampling time, discontinuity gain and dynamics of the system and the actuators.

One way to decrease the chattering of the controller is to implement a boundary layer around the sliding surface inside which the discontinuity gain is decreased. The boundary layer is illustrated by the grey area around $s = 0$ in figure 5.4. This can effectively eliminate chattering but has the downside of decreasing the robustness and tracking accuracy inside the boundary layer. Obviously the width of the boundary layer (denoted by θ_c) should be chosen as small as possible while reducing the chattering to an acceptable extend.

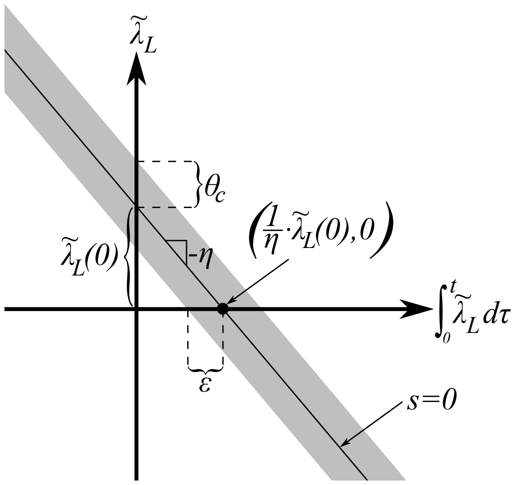

Figure 5.4: Illustration of boundary layer (grey area) in the λ_{Lij}-$\dot{\lambda}_{Lij}$ plane.

In this project the boundary layer will have a fixed width θ_c and the gain k will decrease linearly with s inside the boundary layer. This is achieved by replacing sign(s) with [38, p.290-299]:

$$\mathrm{sat}\left(\frac{s}{\theta_c}\right) = \begin{cases} \dfrac{s}{\theta_c} & \text{for} \left|\dfrac{s}{\theta_c}\right| \leq 1 \\ \mathrm{sign}\left(\dfrac{s}{\theta_c}\right) & \text{otherwise} \end{cases}$$

The boundary layer is a global invariant set as $\mathrm{sat}\left(\frac{s}{\theta_c}\right) = \mathrm{sign}(s)$ outside the boundary layer. The system trajectories will therefore converge to the boundary layer.

The boundary layer width θ_c gives a guaranteed limitation of the tracking error. The relationship between θ_c and tracking error is given as [38, p.291]:

$$\forall t \geq 0 \ , \ |\tilde{\lambda}_{Lij}(t)| \leq 2 \cdot \eta \cdot \varepsilon$$

for all trajectories starting inside the boundary layer. ε is illustrated in figure 5.4. It is defined as $\varepsilon = \frac{\theta_c}{\eta}$ and it is therefore guaranteed that:

$$\forall t \geq 0 \; , \; |\tilde{\lambda}_{Lij}(t)| \leq 2 \cdot \theta_c \tag{5.35}$$

The upper bound on the guaranteed tracking accuracy corresponds to a worst case situation where $|\hat{f} - f| = F$ and $\hat{g}/g = \beta$. The tracking error is therefore often significantly lower than the maximum bound.

The boundary layer width θ_c and the convergence rate η are tuned through simulation. The choice of θ_c and η is dependent on the actuator dynamics and is therefore different for TCS/ABS and front/rear wheels. The results are listed in table 5.3. The field TCS/Rear wheels is left blank as no actuation of the rear wheels is possible during acceleration.

	Front wheels	**Rear wheels**
TCS	$\theta_c = 0.05$ $\eta = 22$	
ABS	$\theta_c = 0.05$ $\eta = 8.8$	$\theta_c = 0.03$ $\eta = 8.8$

Table 5.3: Boundary layer width θ_c and convergence rate η.

The slip error is therefore limited to 0.1 for the front wheels and 0.06 for the rear wheels. For maximum utilization of the available tire-road friction the slip reference might be as low as 0.06 (corresponding to λ_{max} when driving on snow). It is therefore only guaranteed that the slip error is less than or equal to 167 % of the slip reference. However, as mentioned, this corresponds to a worst case scenario and the actual error is often significantly lower which will be shown in Chapter 6.

The effect of implementing the boundary layer is illustrated by simulating a straight line braking maneuver on dry asphalt with and without the boundary layer implemented. The simulations are made using the MATLAB Simulink model described in Section 3.9 with an initial vehicle velocity of $\dot{x}(0) = 80$ $[km/h]$ and a constant slip reference of $\lambda_{L,ref} = 0.17$. Plots of the longitudinal slip response (at a front wheel) with and without the boundary layer is seen in figure 5.5. The response corresponding to $s = 0$ and the tracking limits imposed by the boundary layer is plotted as well.

It is seen from the plot in figure 5.5 that the boundary layer effectively reduces the oscillations caused by the control discontinuity while keeping the tracking error well below the depicted limits (illustrated by the dotted lines). The increasing magnitude of the chattering seen in the simulation without the boundary layer is a result of the increasingly fast slip dynamics caused by the decreasing vehicle velocity during the braking maneuver.

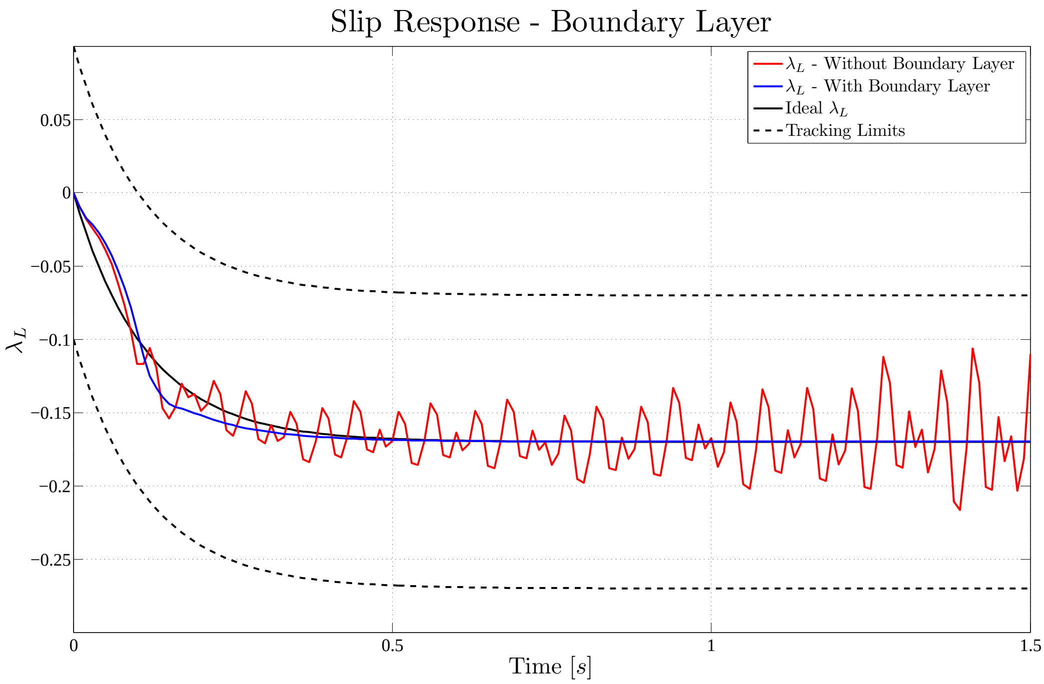

Figure 5.5: Simulated slip response with and without boundary layer.

The sliding motion of the trajectories is shown by plotting the phase portrait of the system. The phase portrait corresponding to the simulation described above is plotted in figure 5.6.

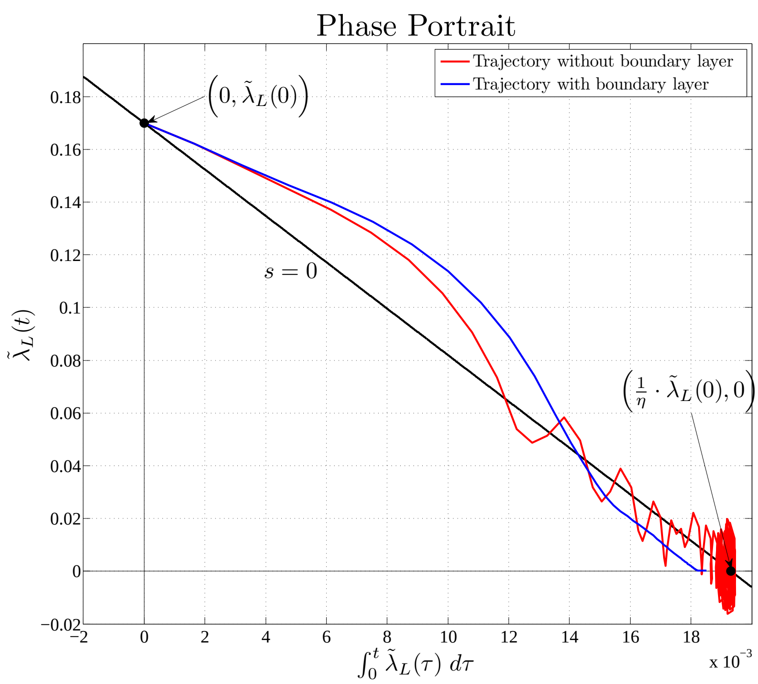

Figure 5.6: $\left(\frac{1}{\eta} \cdot \tilde{\lambda}_L(0), 0\right)$ trajectories with and without boundary layer.

The ideal response in the $\int_0^t \tilde{\lambda}_{Lij}(\tau)\, d\tau$-$\tilde{\lambda}_{Lij}(t)$ plane is indicated by the black line ($s = 0$). If the trajectories slide along this line, then ideal sliding motion is achieved and the trajectories converge to the desired equilibrium point $\left(\frac{1}{\eta} \cdot \tilde{\lambda}_L(0), 0\right)$. It is seen that the trajectory chatters around $s = 0$ when no boundary layer is implemented. The chattering is significantly reduced by the boundary layer at the expense of converging to a non-ideal equilibrium point. It is however noted that the trajectory slowly converges towards the desired equilibrium point as the small tracking error is integrated.

A final advantage of implementing the boundary layer is that the control effort is reduced as the oscillations of the controller output are lowered. This is clearly seen from figure 5.7 showing the simulated output of the slip controller (the reference torque that must be supplied by the brakes and the PMSMs) for the simulation described above.

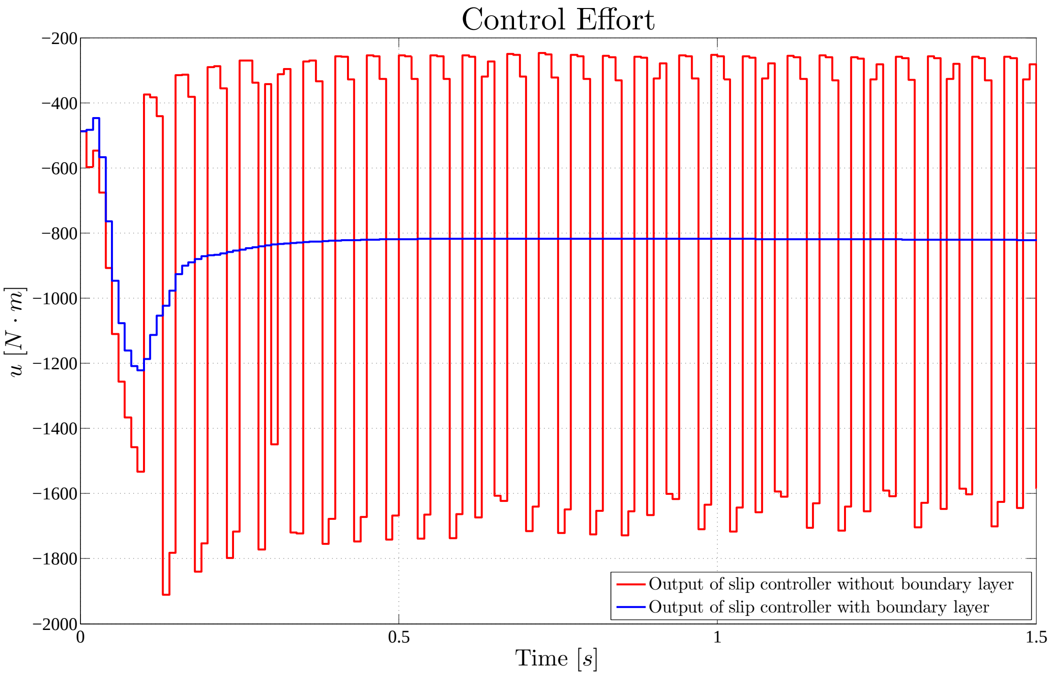

Figure 5.7: Output of slip controller with and without boundary layer implemented.

The reduced oscillations of the control signal protects the system from vibrations caused by the control discontinuity as well as reduces the energy consumption needed to control the slip.

5.2.5 Anti Wind-up

The sliding surface given by equation (5.14) involves integration of the slip error. This presents a risk of integration wind-up as the motor torque is limited. Many different anti wind-up schemes exist for PID-type controllers (13 approaches are presented in [41]). However, as the wind-up problem is in the variable s and not directly on the control output as in PID-control the normal anti wind-up schemes cannot be directly implemented. The problem of designing an anti wind-up algorithm is therefore presented in this section.

The proposed anti wind-up scheme involves switching between two sliding surfaces - the sliding surface designed in Section 5.2.1 is used when the output of the controller u_{ij} is within the limits of T_{mj} and another surface is chosen if the output is outside this limit, i.e. if actuator saturation occurs. As the system leaves saturation at time t_o the originally proposed sliding surface (equation (5.14)) is switched on again with the term $\tilde{\lambda}_{Lij}(0)$ replaced by $\tilde{\lambda}_{Lij}(t_o)$ and $\int_0^t \tilde{\lambda}_{Lij}(\tau)$ replaced by $\int_{t_o}^t \tilde{\lambda}_{Lij}(\tau)$. The sliding surface is thereby shifted so that the trajectories at t_o are located at $s = 0$ and exponential convergence is obtained immediately.

The error function s that is used when $|u_{ij}| > T_{mj,max}$ is chosen as:

$$s = \tilde{\lambda}_{Lij} \tag{5.36}$$

As mentioned in Section 5.2.1 this error function corresponds to a vertical sliding surface in the λ_{Lij}-$\dot{\lambda}_{Lij}$ domain and does not yield exponential error convergence. However, as exponential convergence cannot be guaranteed when the actuators are saturated, this error function is suitable as it does not involve error integration.

The following control law makes $s = \tilde{\lambda}_{Lij} = 0$ a globally asymptotically stable equilibrium:

$$u_{ij} = -\frac{\hat{f} + k \cdot \mathrm{sign}(s)}{\hat{g}} \tag{5.37}$$

with k given as:

$$k = \beta \cdot F + (\beta - 1) \cdot |\hat{f}| \tag{5.38}$$

These results can be obtained using a similar approach as in Section 5.2.2. A boundary layer is added around $s = 0$ as in Section 5.2.4.

It is observed that the control law used when $|u_{ij}| > T_{mj,max}$ is slightly different compared to the control law used when $|u_{ij}| \leq T_{mj,max}$. The control laws are however equal if η and $\lambda_{Lij}(t_o)$ are set to zero.

The anti wind-up is only implemented for TCS. The limitations on the motor torque is compensated for by the brakes during ABS. The effect of adding the proposed anti wind-up scheme to the slip controller is illustrated by a simulation with and without anti wind-up implemented. The simulation is made using the MATLAB Simulink model described in Section 3.9. The simulation corresponds to driving on dry cobblestone with an initial vehicle velocity of $\dot{x}(0) = 5$ $^{km}/_{h}$. The slip reference is initially set at a value that is unobtainable due to the actuator limitation. After 2 [s] the reference is stepped down to a value that is within the limits of the system. Plots of the slip response of the system with and without anti wind-up implemented along with the slip reference is shown in figure 5.8.

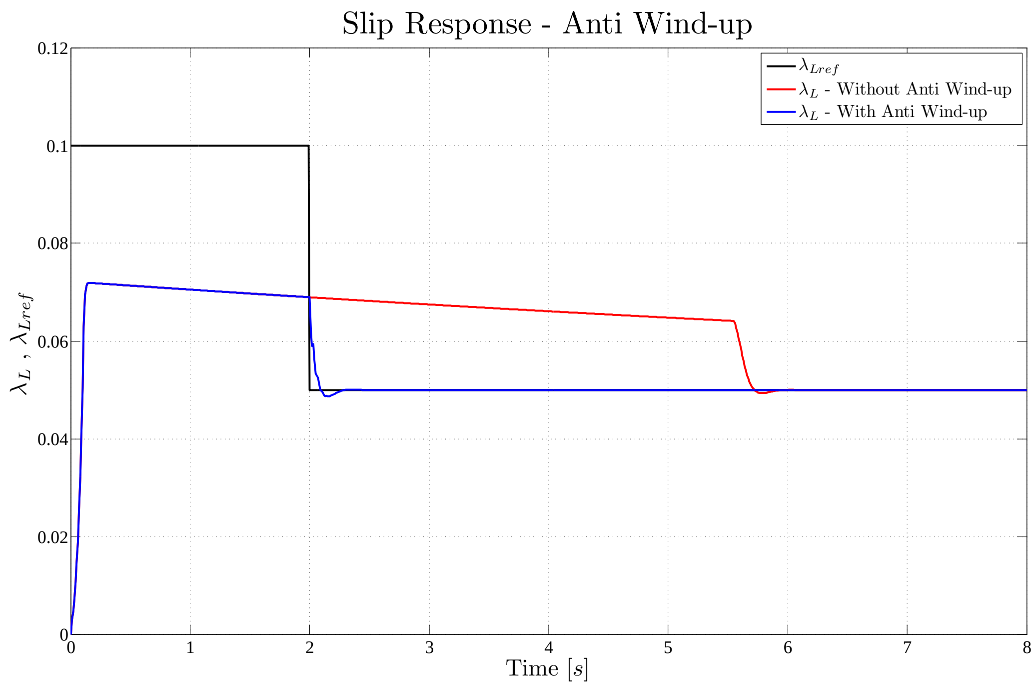

Figure 5.8: Simulated slip response with and without anti wind-up.

It is seen that the initial slip reference cannot be obtained due to the limitation on T_{mj}. As a result the actuator saturates at $T_{mj} = T_{mj,max}$. The slip error is integrated when anti wind-up is not implemented. When the slip reference is lowered this integrated error must be removed by an integration of the negative slip error before the controller reacts to the step. As the error integration is avoided when the anti wind-up is activated the controller immediately responds to the reference step. It is therefore concluded that the proposed anti wind-up scheme successfully reduces the implications of actuator saturation.

With the anti wind-up successfully designed and the chattering reduced the design of the slip controller is complete. The following section treats the problem of distributing the control output between the actuators.

5.3 Torque Distribution

The output of the slip controller designed in Section 5.2 is a desired torque at the wheel axle. During acceleration (TCS) this torque must be developed by the PMSMs at the front wheels. During braking (ABS), the situation is different. At the rear wheels the torque must be supplied by the brakes but at the front wheels the torque can be supplied by the PMSMs, the brakes or both. This section treats the problem of determining how the desired torque at the front wheels should be distributed between the brakes and the PMSMs during braking.

The slip control system is designed with the assumption that the actuator dynamics are infinitely fast. The effect of slow actuator dynamics is oscillations in the slip response. It is therefore concluded that the actuator dynamics should be as fast as possible.

The torque response of the PMSMs is significantly faster than the torque response of the brakes according to Section 3.3 and 3.4. This is illustrated by the unit step response of the two closed-loop torque control systems plotted in figure 5.9, thus the PMSMs should take care of the high frequency content of the control output.

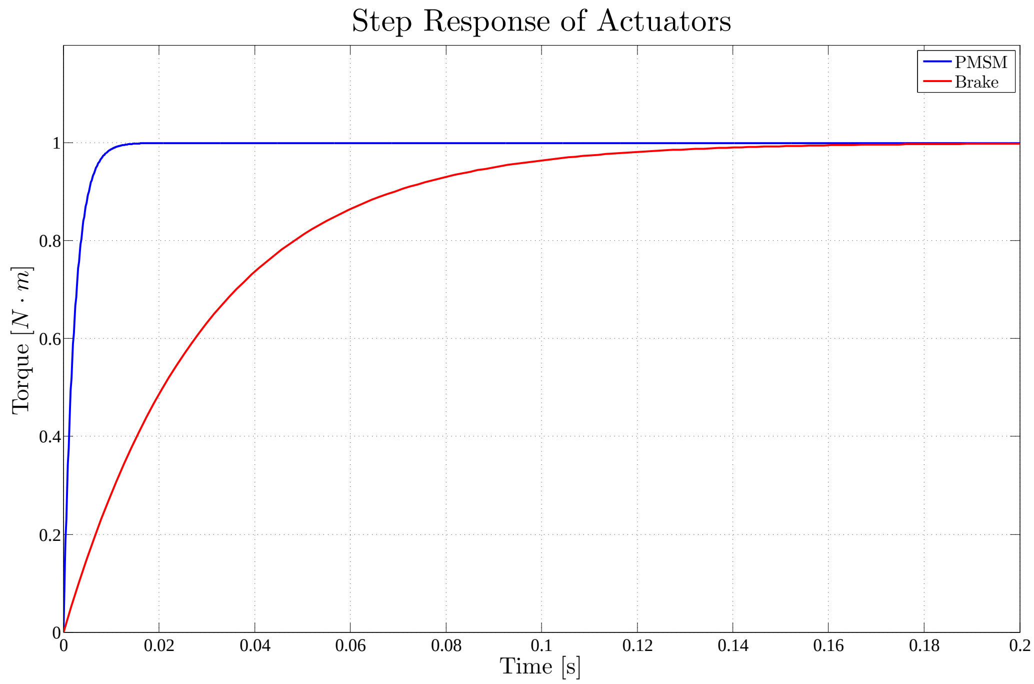

Figure 5.9: Unit step response of PMSM and hydraulic brake.

The PMSMs offer another advantage over the brakes as regenerative braking can be utilized when the PMSMs are braking the vehicle, thus some of the braking energy is recovered as electrical energy in the batteries. From a fuel economical point of view the brakes should only be activated when the PMSMs cannot deliver the demanded torque. As the torque output of the PMSMs is limited, this would result in the PMSMs braking with the maximum allowable torque in hard braking maneuvers. Thus no motor torque is available to act on the fast dynamics of the control output and the dynamic superiority of the PMSMs is lost. Instead the brakes would need to supply the remaining torque needed to stabilize the slip at the reference resulting in slower actuator dynamics.

It is concluded that high performance of the slip controller is more important than using the regenerative braking to a maximum extend. The motivation is that the ABS is designed to avoid crashes and will not be active during normal driving conditions.

The torque distribution system illustrated in figure 5.10 is proposed. $u_{ij,ref}$ is the control output, i.e. the demanded torque at the wheel axle and u_{ij} is the actual developed torque.

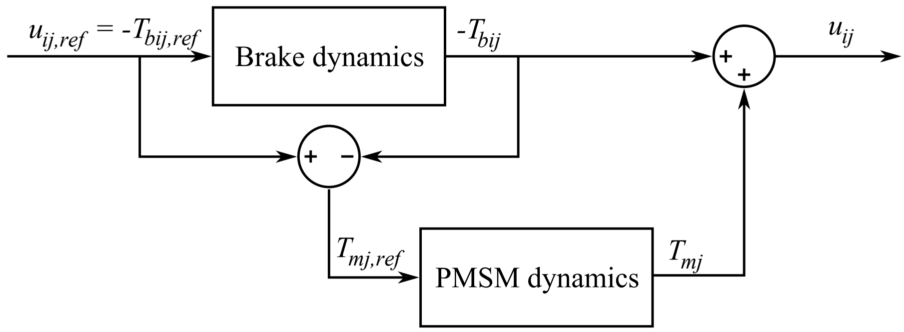

Figure 5.10: Proposed torque distribution system.

With the distribution of $T_{bij,ref}$ and $T_{mj,ref}$ proposed in figure 5.10 the PMSM only acts on the high frequency content of $u_{ij,ref}$ which is not captured by the slow dynamics of the brakes. The result is that the brakes contribute to the majority of u_{ij} while the PMSMs adjusts u_{ij} around T_{bij} to account for the fast dynamics of $u_{ij,ref}$. The system thereby exploits the fast dynamics of the PMSMs while avoiding actuator saturation caused by the torque limitations.

A simulation is made to illustrate the improvement in actuator dynamics caused by the proposed torque distribution. A braking maneuver on dry asphalt is simulated using the MATLAB Simulink model described in Section 3.9 with an initial vehicle velocity of $\dot{x} = 80$ $[{}^{km}/_{h}]$.

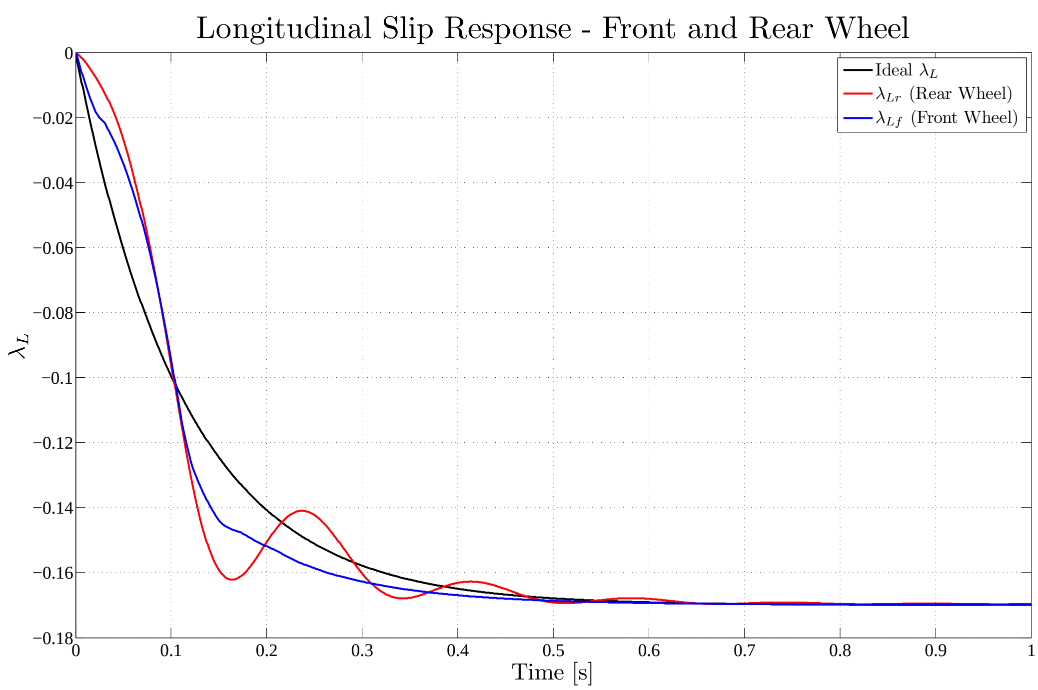

Figure 5.11: Slip response at front and rear wheels during braking maneuver.

Figure 5.11 shows the corresponding slip response at a front and a rear wheel as well as the ideal response corresponding to $s = 0$. The response at the front wheel is seen to have less oscillations compared to the rear

wheels. The torque distribution system thereby improves the actuator dynamics and is implemented in the MATLAB Simulink model.
The next section presents the design of an observer which supplies the slip controller with an estimate of the tire-road friction force.

5.4 Friction Force Observer

The varying tire-road friction force cannot be measured directly. A friction force observer is therefore designed based on sliding mode control theory and derived using Lyapunov stability. A similar observer has been used in the design of a hydraulically actuated slip control system in [11].
The observer is designed to give an estimate of the instantaneous friction force acting on the tire. This is done using measurements of angular velocity, motor torque and braking torque.
For each wheel the tire-road contact point friction force acting along the x^{wij}-axis can be obtained from the wheel torque balance:

$$J_{wi} \cdot \dot{\omega}_{ij} = T_{mj} - T_{bij} \cdot \mathrm{sign}(\omega_{ij}) - b \cdot \omega_{ij} - r \cdot F_{xwij} \tag{5.39}$$

As the angular velocity of the wheel ω_{ij}, the motor torque T_{mj} and braking torque T_{bij} are assumed measurable variables, only the angular wheel acceleration $\dot{\omega}_{ij}$ needs to be derived to determine the friction force. The angular wheel acceleration can be computed by numeric differentiation of the angular wheel velocity. However, even though ω_{ij} can be found with high accuracy using high resolution encoders, the numeric differentiation is still very sensitive to measurement noise and quantization. The proposed observer overcomes this problem as numerical differentiation is avoided.

Under the assumption that J_{wi} and b are known, the model given by equation (5.39) is estimated as:

$$J_{wi} \cdot \dot{\hat{\omega}}_{ij} = T_{mj} - T_{bij} \cdot \mathrm{sign}(\omega_{ij}) - b \cdot \omega_{ij} - r \cdot L(\omega_{ij}, \hat{\omega}_{ij}) \tag{5.40}$$

where $\hat{\omega}_{ij}$ is an estimate of the angular wheel velocity and $L(\omega_{ij}, \hat{\omega}_{ij})$ is a discontinuous input chosen as:

$$L(\omega_{ij}, \hat{\omega}_{ij}) = -M \cdot \mathrm{sign}(e_{\omega,ij}) \tag{5.41}$$

where $e_{\omega,ij} = \omega_{ij} - \hat{\omega}_{ij}$ is the velocity estimation error. It is seen that the signal $L(\omega_1, \hat{\omega}_1)$ is discontinuous across $e_{\omega} = 0$ and thus is expected to oscillate at the sampling frequency for successful estimation ($e_{\omega} \approx 0$).
$L(\omega_1, \hat{\omega}_1)$ is factorized by the observer gain M which - as will be shown below - determines the stability of the observer.
It will now be shown that the low frequency content of $L(\omega_{ij}, \hat{\omega}_{ij})$ is an estimation of the friction force.

Subtracting (5.40) from (5.39) yields the following velocity error dynamics:

$$\dot{e}_{\omega,ij} = \dot{\omega}_{ij} - \dot{\hat{\omega}}_{ij} = -\frac{r}{J_{wi}} \cdot (M \cdot \text{sign}(e_{\omega,ij}) + F_{xwij}) \tag{5.42}$$

Thus $L(\omega_{ij}, \hat{\omega}_{ij}) = F_{xwij}$ when $\dot{e}_{\omega,ij}$=0. However $L(\omega_{ij}, \hat{\omega}_{ij})$ can only take the values $\pm M$ and zero, thus the estimated friction force is equal to the low frequency content (the average) of $L(\omega_{ij}, \hat{\omega}_{ij})$.

It is a necessity that the error dynamics goes towards zero in order to estimate the friction force correctly. The convergence of the error dynamics to zero is therefore proven using Lyapunov stability theory. A Lyapunov function candidate is chosen as a positive definite function of the estimation error:

$$V(e_{\omega,ij}) = \frac{1}{2} \cdot e_{\omega,ij}^2 \tag{5.43}$$

which satisfies $V(e_{\omega,ij}) \to \infty$ as $|e_{\omega,ij}| \to \infty$.

The derivative of $V(e_{\omega,ij})$ is found using the error dynamics in equation (5.42):

$$\begin{aligned} \dot{V}(e_{\omega,ij}) &= \dot{e}_{\omega,ij} \cdot e_{\omega,ij} \qquad \Rightarrow \\ &= -\frac{r}{J_{wi}} \cdot (M \cdot \text{sign}(e_{\omega,ij}) + F_{xwij}) \cdot e_{\omega,ij} \qquad \Rightarrow \\ &= -\frac{r}{J_{wi}} \cdot \left(M \cdot |e_{\omega,ij}| + F_{xwij} \cdot e_{\omega,ij}\right) \end{aligned} \tag{5.44}$$

It is seen that $\dot{V}(e_{\omega,ij})$ is negative definite if the gain M is chosen as:

$$M > \max\left(|F_{xwij}|\right) \tag{5.45}$$

Thus if M satisfies this inequality then the observer is globally asymptotically stable [38, p.65] and $e_{\omega,ij} \to 0$ when $t \to \infty$. As the derivative of $e_{\omega,ij}$ is a discontinuous function this does not guarantee that $\dot{e}_{\omega,ij} \to 0$. However, it is only required that the low frequency content of $\dot{e}_{\omega,ij}$ converges to zero in order to estimate the friction force. This condition is implied by the convergence of $e_{\omega,ij}$ to zero.

As for the sliding mode controller, the discontinuity of the observer causes chattering. In [11] it is proposed that the chattering should be removed through first order low-pass filtering, thereby extracting the low frequency content of $L(\omega_{ij}, \hat{\omega}_{ij})$. The low-pass filtering is expected to deteriorate the dynamic performance of the observer by adding a phase shift to the signal. This might be a problem if the sampling frequency is low compared to the bandwidth of the friction force dynamics. Simulation results showing this problem are presented below.
Another method of reducing the oscillations in the friction force estimate is to add a boundary layer around $e_\omega = 0$ in which the observer gain M is reduced. This is similar to the approach described in Section 5.2.4 and

reduces the estimation accuracy of the observer by only guaranteeing that e_ω converge to a value less than or equal to the width of the boundary layer. Thus the boundary layer is a global invariant set towards which the velocity error converges asymptotically [38, p.73].

5.4.1 Tuning of Observer parameters

The dynamic performance of the observer is investigated by implementing the observer in the MATLAB Simulink model described in Section 3.9. The observer response is then simulated under the following conditions:

- The road surface is set to dry asphalt. This road surface will require the highest absolute value of the tire-road friction for all slip values compared to the different road surfaces given in table 3.1. The peak friction force is therefore an indication of the maximum tire-road friction achievable. This can be used to give an estimate of a suitable observer gain M.
- The vehicle motion is only in the longitudinal direction during simulation. The steering angle reference is thus set to zero so that no side slip is present. Thus all of the available friction lies in $F_{xwij} = F_{xij}$.
- The observer is tested in a braking situation using the torque distribution described in Section (5.3). As this results in faster actuator dynamics on the front wheels compared to the rear wheels the friction force changes more rapidly at the front wheels than at the rear wheels.
  The initial vehicle velocity is set to $\dot{x}_0 = 150$ $[{}^{km}/_{h}]$ to induce a relatively long braking time.

The inputs to the observer model are: The angular velocity ω_{ij} and the actuator torques supplied by the brakes T_{bij} and the motors through the gear T_{mj}.
The system is tested by supplying step inputs to the actuator dynamics. The steps are chosen so that the slip reaches values close to the peak of the friction curve.

The simulation is run twice under the same conditions. In the first simulation the suggested filtering of $L = -M \cdot sign(e_\omega)$ is tuned so that the oscillations of L are suppressed. The filter is removed in the second simulation and the oscillations of L are suppressed by adding and tuning the suggested boundary layer around $e_\omega = 0$. Simulation results for both situations are shown in figure 5.12 along with the true simulated friction force. The plots in figure 5.12 correspond to forces at a front wheel.

The peak of the true friction force has a value of -2691 $[N]$ while the observer gain, M_o, is 3000. The closer this gain is to the magnitude of F_{xwij} the less oscillations are seen on the friction estimate, however a safety margin is added to the observer gain to account for variations in F_{xwij} due to increases in load transfer and in m.

The friction estimated through the first order filter (the green curve on figure 5.12) is seen to follow the true friction poorly. The filter was designed with a cutoff frequency of $f_c = 1$ $[Hz]$ to filter out the oscillations of L. The cutoff frequency could have been increased if the sampling time T_s was lower and the filter would have shown a faster dynamic response.

It is seen that the boundary layer effectively filters out oscillations of the estimate while maintaining a significantly improved dynamic response (the blue curve on figure 5.12). By tuning the width of the boundary layer the best friction estimate response is found with $\theta_o = 6$ for the front wheels. Using this boundary layer, the error of the estimated friction force is within 5 % after 0.06 [s].

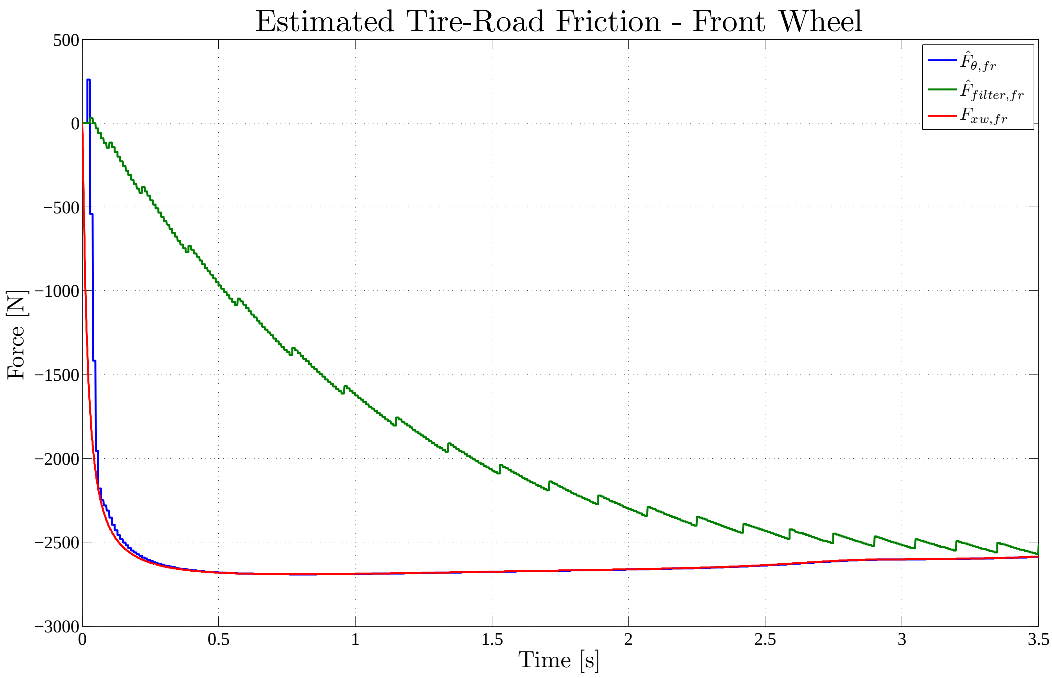

Figure 5.12: Simulated true $F_{xw,fr}$ and estimated friction forces $\hat{F}_{\theta,fr}$ and $\hat{F}_{filter,fr}$ for a front wheel.

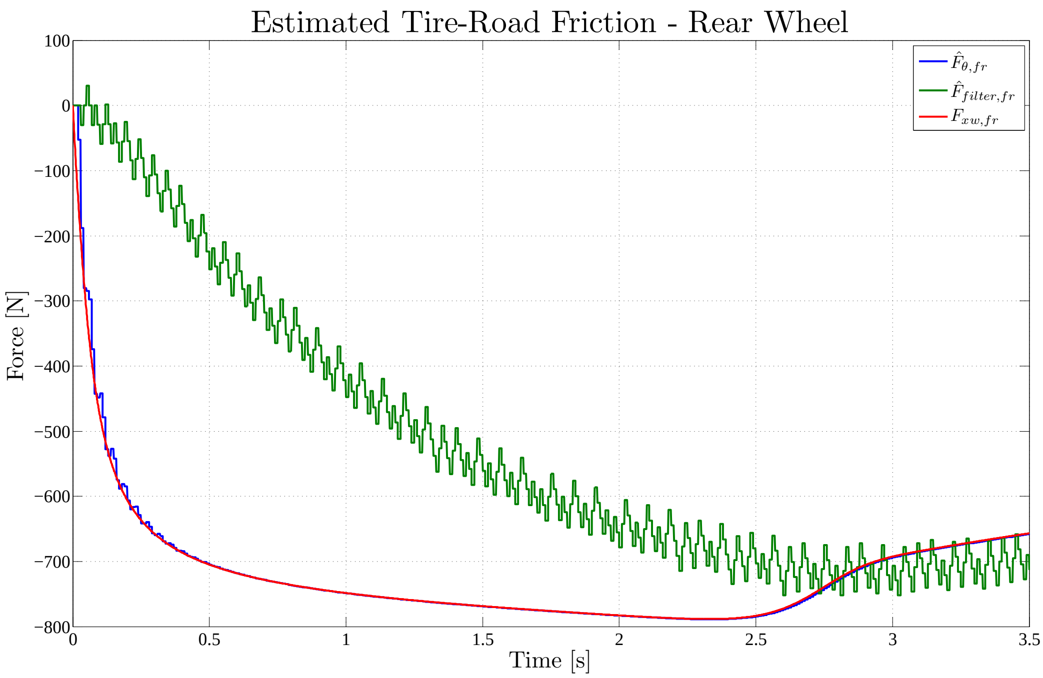

Figure 5.13: Simulated true $F_{xw,rr}$ and estimated friction forces $\hat{F}_{\theta,rr}$ and $\hat{F}_{filter,rr}$ for a rear wheel.

The tire-road friction estimated at a rear wheel is shown in figure 5.13. In this figure the oscillations of the filtered friction estimation has a higher amplitude. Since the rear wheel tire-road friction has a minimum value of -788 $[N]$ (due to the dynamic load transfer) the observer gain is further from the magnitude of F_{xwij} and the oscillations are larger. Again the dynamic performance is significantly improved by using a boundary layer to filter out the oscillations of the estimate compared to the low-pass filter. The width of the boundary layer is chosen as $\theta_o = 3$ for the rear wheels. The error of the friction force estimate is within 5 % after 0.11 $[s]$.

The observer is also tested in a simulation where the vehicle is accelerated. The estimated friction showed responses similar to the braking situation.

5.4.2 Observer Test

The observer is tested in a laboratory to investigate its performance experimentally. The test is described in Appendix A.4. The observer parameters used in the test differs from the tuned parameters designed for the dynamic vehicle model as the test system parameters differs from parameters in the dynamic vehicle model used in simulations. The variation between test-setup system and dynamic model is explained in Appendix A.1. In table 5.4 the tuned observer parameters are listed for both test and simulation. The tuning of the parameters used in the test is outlined in the test journal.

	θ_o	M_o
Test	2	1000
Simulation	6 (front wheels) 3 (rear wheels)	3000

Table 5.4: Tuned observer parameters.

A MATLAB Simulink model is used to emulate the test system based on the mathematical model of the setup given in Appendix A.1. A simulation is made using a torque input similar to the input given in test 4 of the test journal. The output of the simulation is then compared to the test results. The comparison is seen in figure 5.14. Since the friction forces in the contact point in the test is unknown the friction surface in simulation is chosen as dry concrete as this shows the estimation of the friction force closest to the test data. Choosing different road surfaces changes the slope of the friction estimate for a constant torque input. The same was concluded in the test journal where the surface friction was changed by adding an oil based lubrication. The inability to emulate the exact friction characteristics encountered in the experiment is assumed to be the reason that the simulated result has a slightly different slope and does not reach the exact same values as the test results.
From the observer test journal it was concluded that pre-filtering the angular velocity input affects the dynamic response of the estimated friction force. The settling time of the response equals that of the filter response. A filter identical to the one used in test is thus added in the simulation and the filter is seen to have the same effect. Furthermore noise is added to the simulated angular velocity measurement. The magnitude of the noise is chosen to match the observed noise in the test. The noise is seen to influence the friction estimate; it fluctuates with approximately 8 $[N]$ from its true value.

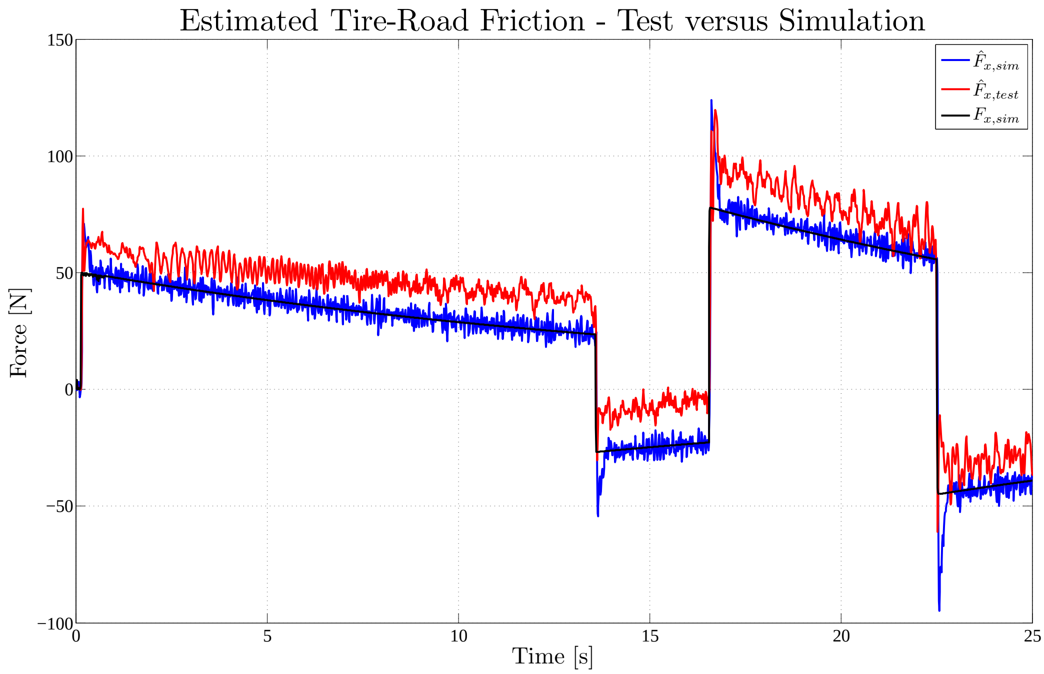

Figure 5.14: Estimated friction force from test $\hat{F}_{x,test}$ compared to estimated friction force from simulation $\hat{F}_{x,sim}$ and true simulated friction force $F_{x,sim}$.

Comparing the estimated friction force to the true friction force (determined by Burckhardts tire model) in the test simulation gives an indication of the accuracy of the estimated friction from test. Naturally this friction is unknown but assuming that its dynamics are similar to the simulated dynamics the friction estimate from test mostly differs from the actual value when a step is applied and then quickly settles at the actual value with small fluctuations due to noise in the angular velocity measurement.

Apart from being an input to the slip controller, the friction force estimate is the basis of an online friction curve estimator which is presented in the following section.

5.5 Friction Curve Estimator

A critical point in the design of a slip control system is to make the system track an optimal slip value. An often used optimal value is the slip corresponding to maximum friction in the longitudinal direction. In this project the optimal slip is defined as the slip value corresponding to maximum resulting friction, i.e. the slip value $\lambda_{max,ij}$ that utilizes all of the available friction. This value gives an optimal trade-off between longitudinal and lateral friction forces - see Section 3.2. If the friction characteristics are known a longitudinal slip λ_{Lij} can always be found to ensure that $\lambda_{res,ij} = \lambda_{max,ij}$ as long as $\lambda_{Sij} \leq \lambda_{max,ij}$ - see equation (3.11).
The major problem in designing the reference to the slip controller is that the value $\lambda_{max,ij}$ changes as the road conditions are altered.
Different approaches have been proposed to overcome this problem. Optimum-seeking controllers have been proposed in [11] and [35, ch.7]. Another method is to estimate the friction characteristics while driving. This can be done using a variety of estimation approaches. The maximum likelihood algorithm has been proposed

in [35, ch.8] due to its ability to estimate nonlinear models (the Burckhardt tire model used in this report is nonlinear in the describing parameters c_1, c_2 and c_3), however this algorithm has been shown to yield reduced estimation accuracy when implemented as a recursive algorithm [35, ch.8]. A widely used approach is to linearize the friction model thereby obtaining a model which is linear in its describing parameters. The linearized model can then be estimated using e.g. a recursive least squares (RLS) algorithm. Different linearized models have been proposed in the literature, e.g. [35, ch.8], [22, ch.9].

An RLS estimation problem is proposed in this project using an approximation of the Burckhardt friction model. The friction coefficient as a function of the resulting slip will be referred to as the *friction curve* and the estimator will be referred to as the *friction curve estimator*.

The friction model used for estimation is [22, p.378]:

$$\mu = \frac{\mu^* \cdot \lambda_{res}}{1 + k_1 \cdot \lambda_{res} + k_2 \cdot \lambda_{res}^2} \tag{5.46}$$

This model can be rearranged to give a linear relationship between μ and the parameters μ^*, k_1 and k_2. The denominator of equation (5.46) is derived from a 2nd order power series approximation of the exponential function used in the Burckhardt friction model and μ^* is the initial slope of the friction curve. It is seen that μ^* can be determined by a combination of the variables c_1, c_2 and c_3 as:

$$\mu^* = \left.\frac{\partial \mu(\lambda_{res})}{\partial \lambda_{res}}\right|_{\lambda_{res}=0} = \left.\left(c_1 \cdot c_2 \cdot e^{-c_2 \cdot \lambda_{res}} - c_3\right)\right|_{\lambda_{res}=0} = c_1 \cdot c_2 - c_3 \tag{5.47}$$

This parameter varies in a relatively small range from from $\mu^* = 8.18$ for dry cobblestone to $\mu^* = 30.19$ for dry asphalt. It is therefore suggested in [22] not to estimate this parameter and keep it at a fixed value. In this project μ^* will however be estimated but an initial guess of $\mu^* = 25$ will be used in the RLS algorithm.

5.5.1 Recursive Least Squares Algorithm

The recursive least squares algorithm is briefly described in this section.
A least squares estimator assumes a linear model structure given by [14, p.5]:

$$\hat{y}(t) = \psi^T(t) \cdot \hat{\theta}_\mu \tag{5.48}$$

where $\psi^T(t)$ is the regression vector, $\hat{\theta}_\mu$ is an unknown vector containing the parameters to be estimated and $\hat{y}(t)$ is the estimated output vector.
The estimator determines $\hat{\theta}_\mu$ based on the error between the estimated model and the true model assumed to have the form:

$$y(t) = \psi^T(t) \cdot \theta_\mu \tag{5.49}$$

here $y(t)$ is the true output vector (this vector is assumed to be measurable) and θ_μ contains the true values of the parameters to be determined. The error between the true output and the estimated output is then:

$$\varepsilon(t,\theta) = y(t) - \underbrace{\psi^T(t) \cdot \hat{\theta}_\mu}_{\hat{y}(t)} \tag{5.50}$$

The minimization criterion for the least squares estimator is formulated as:

$$V_N(\hat{\theta}) = \frac{1}{N} \cdot \sum_{t=1}^{N} \frac{1}{2} \cdot \varepsilon^2(t,\hat{\theta}_\mu) \tag{5.51}$$

where N is the number of samples used in the estimator.

A simplified block diagram of the LS estimator is seen in figure 5.15.

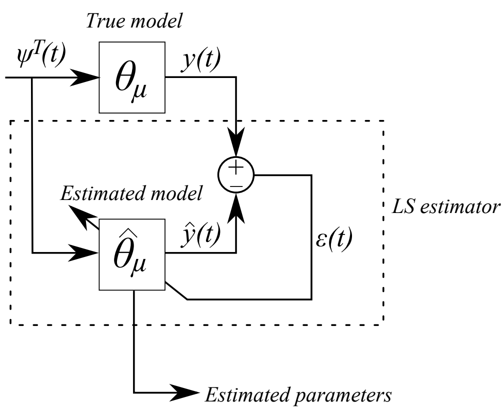

Figure 5.15: Simplified block diagram of LS estimator.

The RLS estimation algorithm can be formulated as [22, p.481]:

$$\begin{aligned}
\varepsilon(k-1) &= y(k) - \psi^T(k) \cdot \hat{\theta}_\mu(k-1) \\
\gamma(k-1) &= \frac{P(k-1) \cdot \psi(k)}{1 + \psi^T(k) \cdot P(k-1) \cdot \psi(k)} \\
P(k) &= P(k-1) - \gamma(k-1) \cdot \psi^T(k) \cdot P(k-1) \\
\hat{\theta}_\mu(k) &= \hat{\theta}_\mu(k-1) + \gamma(k-1) \cdot \varepsilon(k-1)
\end{aligned} \tag{5.52}$$

5.5.2 Recursive Least Squares Implementation

It is observed that the friction model given by equation (5.46) can be rearranged as:

$$\underbrace{\mu}_{y(t)} = \underbrace{\begin{bmatrix} -\lambda_{res} \cdot \mu & -\lambda_{res}^2 \cdot \mu & \lambda_{res} \end{bmatrix}}_{\psi^T(t)} \cdot \underbrace{\begin{bmatrix} k_1 \\ k_2 \\ \mu^* \end{bmatrix}}_{\hat{\theta}_\mu} \tag{5.53}$$

This model description is suitable for RLS estimation of the parameters μ^*, k_1 and k_2.

The inputs to the friction curve estimator is the instantaneous friction coefficient μ and the resulting slip λ_{res}. The friction coefficient is not directly measurable but can be approximated by dividing the estimated friction force $\hat{F}_{wx}$ (obtained from the friction force observer) by an approximation of the normal force at the tire. The normal force is not assumed to be measurable and a constant value of $\hat{F}_z = \frac{\hat{m} \cdot g}{4}$ will be used as an approximation. The variations due to dynamics load transfer and changes in m are not considered in this approximation. An estimation of μ is thereby given as:

$$\hat{\mu} = \frac{\hat{F}_{xw}}{\hat{F}_z} \tag{5.54}$$

This approximation only holds for purely longitudinal motion resulting in $\mu_L = \mu = \frac{F_x}{F_z} = \frac{F_{xw}}{F_z}$ and $\lambda_L = \lambda_{res}$. The friction curve estimator will therefore only be used under this condition.

It is noted that the optimal slip value corresponding to the peak of the estimated friction curve is simply given as:

$$\lambda_{max} = \frac{1}{\sqrt{k_2}} \tag{5.55}$$

The estimator is implemented in the MATLAB Simulink model described in Section 3.9 and its performance is tested through simulation.

5.5.3 Simulation of The RLS Estimator

The RLS estimator is required to be persistently excited by the input data in order to give a good estimate of the unknown parameters [14, p.7]. It is assumed that the varying acceleration and braking encountered in a driving situation produces a sufficiently rich signal for estimation. The input to the estimator is therefore varied over a wide range of operating points in the simulations by using the slip controller to track a varying reference. The reference slip is chosen as a sinusoidal signal of 0.1 $[Hz]$ with different magnitudes for different simulations. The estimator is tested in a simulated braking situation by varying the magnitude of the sinusoidal slip reference from 0.005 to 0.4. The maximum slip reference magnitude is chosen as λ_{max} for dry cobblestone

as this corresponds to the highest peak slip value.
During acceleration the sinusoidal magnitude is varied from 0.005 to 0.2 as higher λ_{max}-values cannot be encountered due to the actuator limitations.

Estimation During Braking

Using the slip reference described above the estimator is tested through simulation. The simulations use an initial velocity of 130 $[km/h]$ and $m = 600$ $[kg]$.
During the simulations it was observed that the estimated parameters did not yield acceptable friction curve estimates due to the dynamic load transfer between the front and rear wheel axle. To account for this the estimation is performed with a single RLS estimator using the average of the estimated friction forces of the 4 wheels and the average slip as inputs. The friction curve is therefore not estimated for each wheel but an average friction curve is obtained and used for all wheels. Different friction characteristics at each wheel is therefore not taken into account.
The simulations are repeated using the averaged inputs. An example of the estimated friction curves using different reference slip magnitudes is seen in figure 5.16. The plots in the figure are the estimated friction curves obtained after approximately 2 $[s]$ when driving on wet asphalt. The true friction curve (from the Burckhardt friction model) is plotted as the black curve.

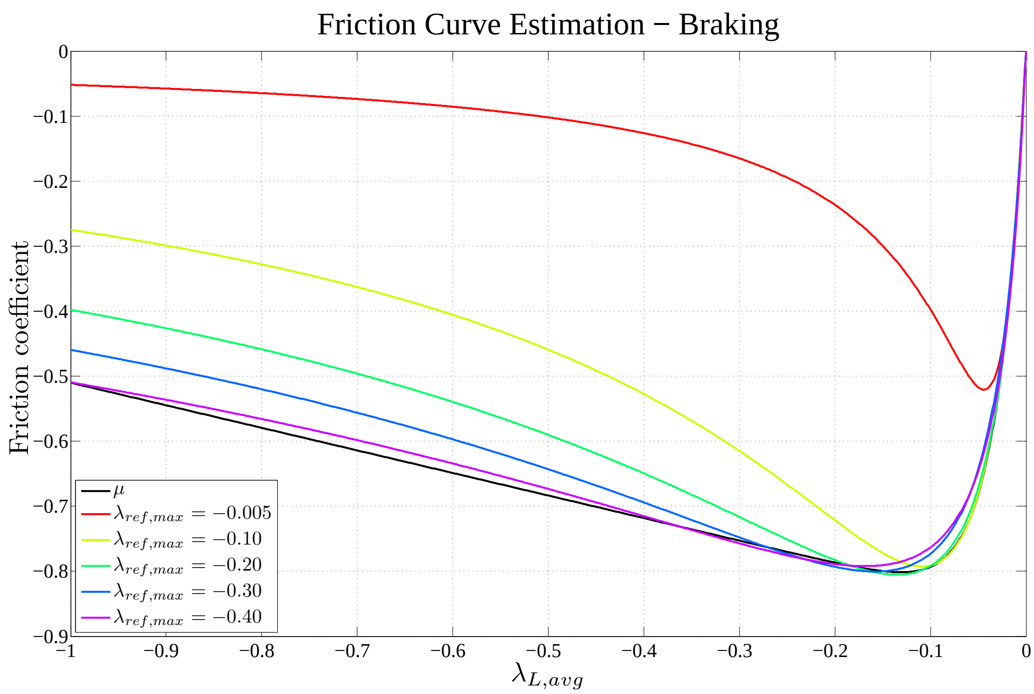

Figure 5.16: Simulated friction curve estimates for different slip reference magnitudes. The road surface is wet asphalt.

It is seen that the initial slope μ^* of the friction curve is estimated well for all slip references. It is also seen that the curve is estimated better for higher slip references. It is necessary for the slip to reach values near λ_{max} in order to give a good estimate of the peak of the friction curve which is not the case for the lowest slip reference (the red curve). As k_2 uniquely determine $\hat{\lambda}_{max}$ this is the most important term to estimate correctly.

The estimator performance is therefore tested by its ability to estimate λ_{max}. It is observed that the slope of the friction curve in the vicinity of the λ_{max} is low. This means that even if λ_{max} is not correctly estimated it may still be possible to utilize a large part of the available friction. It is therefore interesting to investigate how much of the available friction is utilized if the slip is stabilized at $\hat{\lambda}_{max}$ compared to λ_{max}. Table 5.5 summarizes the estimate of λ_{max} and the corresponding fraction of utilized friction given by $\frac{\mu(\hat{\lambda}_{max})}{\mu(\lambda_{max})}$ for different surfaces and slip reference magnitudes. The true value of λ_{max} is also given in the table.

		$\lambda_{ref,max} = 0.005$		$\lambda_{ref,max} = 0.10$		$\lambda_{ref,max} = 0.20$		$\lambda_{ref,max} = 0.30$		$\lambda_{ref,max} = 0.40$	
Road surface	λ_{max}	$\hat{\lambda}_{max}$	$\frac{\mu(\hat{\lambda}_{max})}{\mu(\lambda_{max})}$	$\hat{\lambda}_{max}$	$\frac{\mu(\hat{\lambda}_{max})}{\mu(\lambda_{max})}$	$\hat{\lambda}_{max}$	$\frac{\mu(\hat{\lambda}_{max})}{\mu(\lambda_{max})}$	$\hat{\lambda}_{max}$	$\frac{\mu(\hat{\lambda}_{max})}{\mu(\lambda_{max})}$	$\hat{\lambda}_{max}$	$\frac{\mu(\hat{\lambda}_{max})}{\mu(\lambda_{max})}$
Asphalt, dry	0.170	0.059	0.801	0.144	0.996	0.167	0.999	0.185	0.999	0.196	0.997
Asphalt, wet	0.131	0.054	0.872	0.111	0.996	0.139	0.999	0.157	0.996	0.165	0.994
Concrete, dry	0.160	0.064	0.849	0.137	0.996	0.159	1.000	0.176	0.999	0.185	0.997
Cobble-stone, dry	0.400	0.064	0.424	0.364	0.997	0.388	0.999	0.391	0.999	0.400	1.000
Cobble-stone, wet	0.140	0.121	0.998	0.116	0.996	0.145	0.999	0.166	0.997	0.179	0.995
Snow	0.060	0.034	0.972	0.068	0.999	0.093	0.992	0.104	0.989	0.110	0.987
Ice	0.123	0.015	0.989	0.065	1.000	0.122	1.000	0.181	1.000	0.241	1.000

Table 5.5: Summarized friction curve estimation results.

It is seen from the results in table 5.5 that the estimated friction curve peak deviates most from its true value for the lowest slip reference as expected. Furthermore, it is noted that more than 98 % of the available friction can be utilized by using $\hat{\lambda}_{max}$ as a reference to the slip controller at all surfaces if the estimation is performed with $\lambda_{ref,max} \geq 0.1$. Thus, if the input to the estimator is persistently exciting very good estimates can be obtained using the linearized friction model.

Estimation During Acceleration

A similar set of tests are performed for acceleration from an initial velocity of 25 $[{}^{km}/{}_{h}]$. The estimator only takes inputs from the front wheels during acceleration as it is assumed that the slip at the rear wheels is zero. The dynamic load transfer is therefore not compensated for. An example of a set of estimated curves is seen in figure 5.17 along with the actual friction curve corresponding to acceleration on wet cobblestone. This surface corresponds to the maximum friction obtainable - while being able to reach the peak of the friction curve - during acceleration due to actuator limitation. The impact of the dynamic load transfer is therefore most distinct at this road surface.

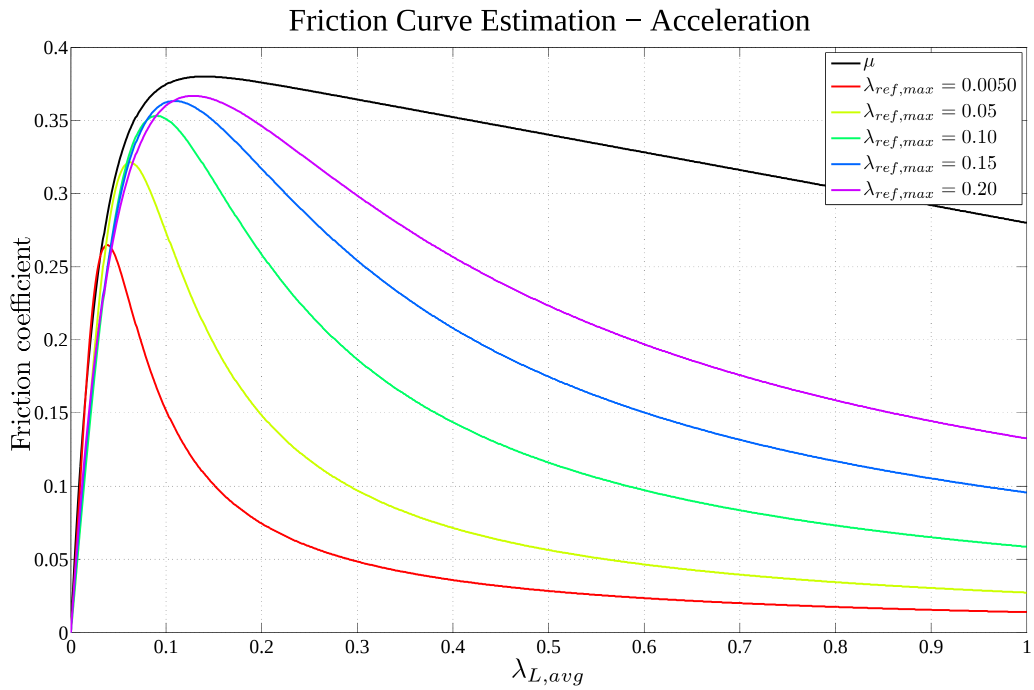

Figure 5.17: Simulated friction curve estimates for different slip reference magnitudes. The road surface is wet cobblestone.

It is seen that the estimated curves are lower in magnitude than the actual friction curve due to the decrease in normal force at the front wheels during acceleration. Again it is noted that good estimation of λ_{max} requires that the slip reaches values near λ_{max} during estimation.

Table 5.6 summarizes the estimator performance during acceleration in terms of $\hat{\lambda}_{max}$ and $\frac{\mu(\hat{\lambda}_{max})}{\mu(\lambda_{max})}$.

		$\lambda_{ref,max} = 0.005$		$\lambda_{ref,max} = 0.05$		$\lambda_{ref,max} = 0.10$		$\lambda_{ref,max} = 0.15$		$\lambda_{ref,max} = 0.20$	
Road surface	λ_{max}	$\hat{\lambda}_{max}$	$\frac{\mu(\hat{\lambda}_{max})}{\mu(\lambda_{max})}$	$\hat{\lambda}_{max}$	$\frac{\mu(\hat{\lambda}_{max})}{\mu(\lambda_{max})}$	$\hat{\lambda}_{max}$	$\frac{\mu(\hat{\lambda}_{max})}{\mu(\lambda_{max})}$	$\hat{\lambda}_{max}$	$\frac{\mu(\hat{\lambda}_{max})}{\mu(\lambda_{max})}$	$\hat{\lambda}_{max}$	$\frac{\mu(\hat{\lambda}_{max})}{\mu(\lambda_{max})}$
Cobble-stone, wet	0.140	0.038	0.751	0.066	0.918	0.098	0.984	0.122	0.998	0.142	1.000
Snow	0.060	0.034	0.977	0.054	0.999	0.076	0.998	0.096	0.991	0.112	0.985
Ice	0.123	0.021	0.998	0.043	1.000	0.070	1.000	0.096	1.000	0.124	1.000

Table 5.6: Summarized friction curve estimation results.

It is seen that the estimate of λ_{max} results in lowest friction utilization when driving on wet cobblestone. It is however noted that more than 98 % of the available friction can be utilized by using $\hat{\lambda}_{max}$ as a reference to the slip controller at all surfaces if the estimation is performed with $\lambda_{ref,max} \geq 0.1$. This is comparable to the results obtained for estimation during braking.

The estimated friction curves presented so far result from estimation over approximately 2 [s]. The estimated parameters are updated at each sampling instant (every 0.01 [s]). The RLS algorithm is designed to improve the estimates at every iteration based on the previous estimate and the new information. The time history of the parameters k_1, k_2 and μ^* and the corresponding friction curve is therefore investigated. This gives an indication on the estimation time required before the output of the estimator can be trusted. Figure 5.18 shows the time history of the parameters k_1, k_2 and μ^* for an estimation during acceleration on snow with a magnitude of 0.1 of the slip reference.

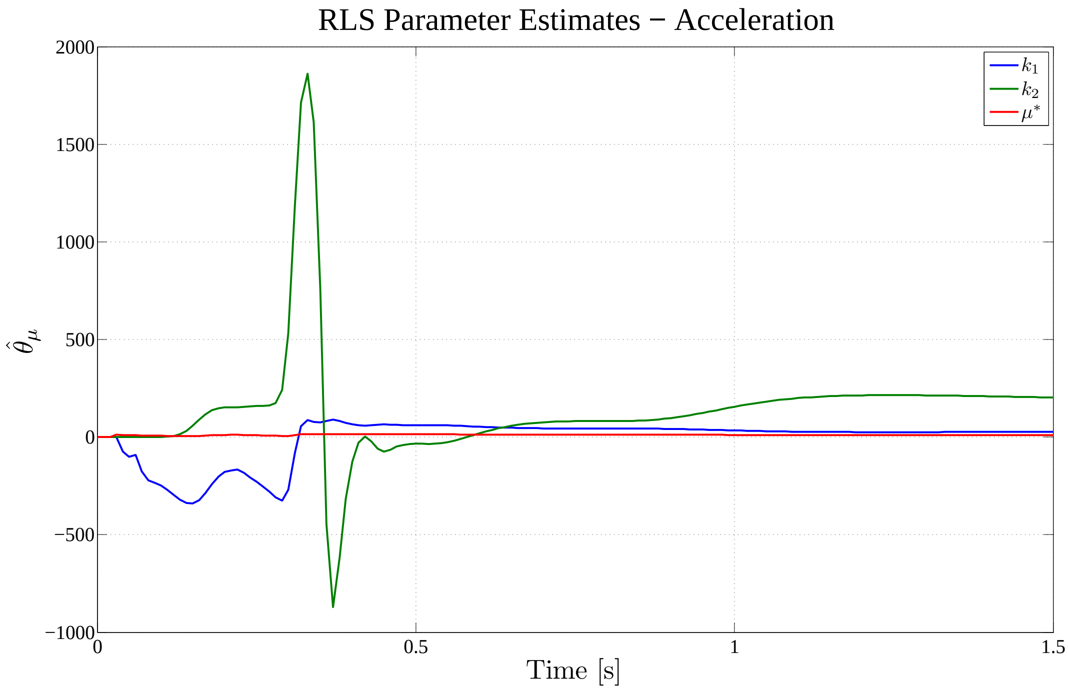

Figure 5.18: RLS parameter estimation for simulated acceleration on snow with $\lambda_{ref,max} = 0.1$.

It is seen that the estimated parameters k_1 and k_2 oscillate during the first 0.5 [s] and take negative values. A negative value of k_2 corresponds to an imaginary value of $\hat{\lambda}_{max}$ (see equation (5.55)). Thus, as a minimum it is required that this parameter is positive. It is also noted that the parameters settle after approximately 1 [s] of estimation. The corresponding time history of the friction curve obtained from the estimated parameters is plotted in figure 5.19. This figure indicates that the friction curve shape is approximately constant after 1 [s]. The initial 0.5 [s] are not shown as the estimated friction curve is far from its true shape.

It is concluded that 1 [s] of estimation is required before the estimated friction curve can be trusted. This presents a problem if the road surface changes suddenly during driving. As an example consider the situation of braking on asphalt when the surface suddenly changes to snow. The estimator would need 1 [s] to supply a suitable reference to the slip controller which increases the braking distance. This example highlights yet a problem with the online friction estimation in combination with slip control. As the vehicle is braking, using the slip controller, the slip is approximately constant during the braking maneuver. As the road surface changes, the slip is still at the value corresponding to maximum friction on asphalt. The input to the estimator is therefore not rich enough to estimate the new friction curve peak.

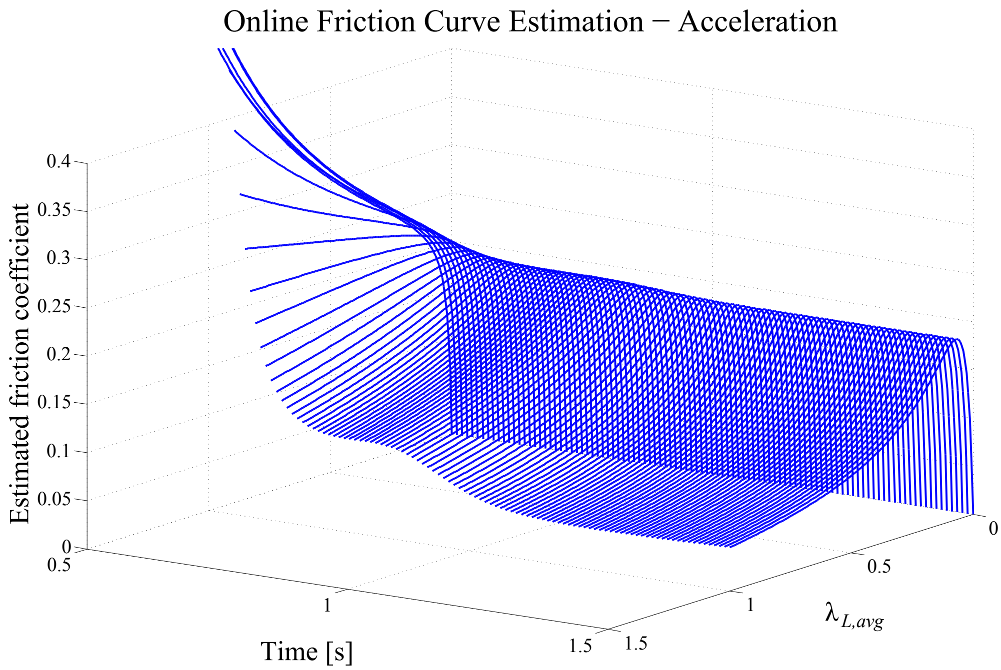

Figure 5.19: Online friction curve estimation for simulated acceleration on snow with $\lambda_{ref} = 0.1$.

It is therefore concluded that the friction curve estimator is useful for estimating a constant surface using a driver supplied input. The proposed estimator is not suitable for fast estimation of changing road conditions. It is therefore investigated whether a constant slip value can result in acceptable friction utilization for the 7 different road conditions.

5.5.4 Friction Utilization Using Constant Slip Reference

An optimal constant slip value λ_{opt} is defined as the slip value which maximizes the guaranteed fraction of utilized friction at any surface. This is formulated mathematically as:

$$\lambda_{opt} = \arg\max_{\lambda_{res}} \left(\min_{r} \left(\frac{\mu_r(\lambda_{res})}{\mu_{r,max}} \right) \right), r = \{1, 2, ..., 7\} \tag{5.56}$$

where μ_r is the friction coefficient at road condition r. The 7 road conditions are listed in table 3.1 in Section 3.2.

The function $\min_{r} \left(\frac{\mu_r(\lambda_{res})}{\mu_{r,max}} \right)$ is plotted in figure 5.20.

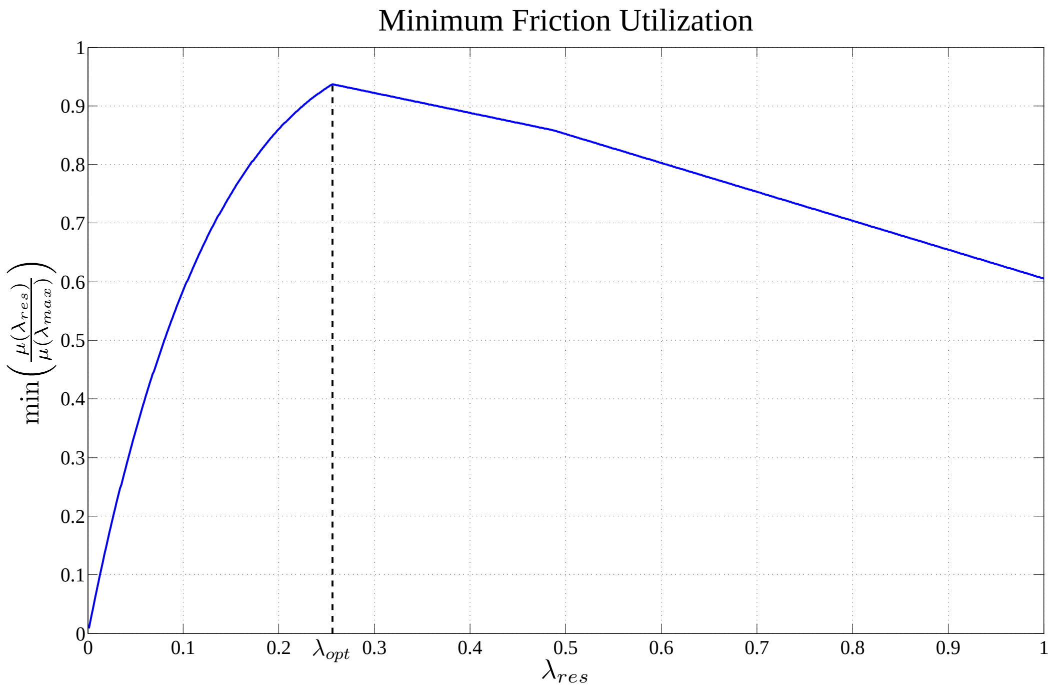

Figure 5.20: Minimum friction utilization at any road surface as a function of resulting slip.

The optimal slip is found as $\lambda_{opt} = 0.256$ with a corresponding value of $\min_r \left(\frac{\mu_r(\lambda_{res})}{\mu_{r,max}}\right) = 0.937$. If the resulting slip is stabilized at this value it is guaranteed that at least 93.7 % of the available friction is utilized at any road condition. The fraction of utilized friction at the 7 surfaces using this slip value is given in table 5.7.

Road surface	$\frac{\mu(\lambda_{opt})}{\mu(\lambda_{max})}$
Asphalt, dry	0.978
Asphalt, wet	0.958
Concrete, dry	0.971
Cobblestone, dry	0.937
Cobblestone, wet	0.973
Snow	0.937
Ice	1.000

Table 5.7: Fraction of utilized friction at all road surfaces with λ_{opt}.

It is seen from the results in table 5.7 that the suboptimal friction utilization achieved by stabilizing the resulting slip at λ_{opt} is above 97 % of the peak friction for dry asphalt, dry concrete, wet cobblestone and ice. For wet asphalt, dry concrete and snow more than 93.7 % of the available friction is utilized. A minimum bound on the utilized friction is thereby guaranteed which is not the case if λ_{max} is estimated online.

It is chosen to use λ_{opt} as a constant reference to the slip controller in order to increase the robustness to changing road conditions.

It is emphasized that if wheel acceleration control was used instead of slip control, it would not be possible to guarantee high friction utilization at all road surfaces [35, p.58-60]. In this case the utilized friction force would be limited to the friction force at the lowest friction surface.

Simulation of Slip Control 6

The slip controller designed in Chapter 5 is implemented in the MATLAB Simulink model described in Section 3.9 and different driving situations are simulated. The performance of the closed-loop system is evaluated in different road conditions and the robustness to the parameter uncertainties described in Section 3.8 is then tested. The system is finally tested in simulated driving situations involving side slip and noisy slip measurements. The controller is shown to satisfy the demands given in the Problem Statement. This includes the requirements regarding braking distance. Simulated braking distances in different driving conditions are presented in the end of this Chapter.

6.1 Slip Control in Different Driving Conditions

The controller performance is initially tested on different road surfaces during longitudinal motion.
The slip reference is $\lambda_{ref} = \lambda_{opt} = 0.256$ in all simulations according to Section 5.5.4. The MATLAB Simulink model is used to simulate the performance of the slip controller during braking and acceleration. The simulation results are presented below.

ABS

A straight line braking maneuver from an initial vehicle velocity of 130 $[^{km}/_{h}]$ is simulated for each of the 7 road surfaces presented in table 3.1. The simulated slip response at a front wheel is plotted in figure 6.1.

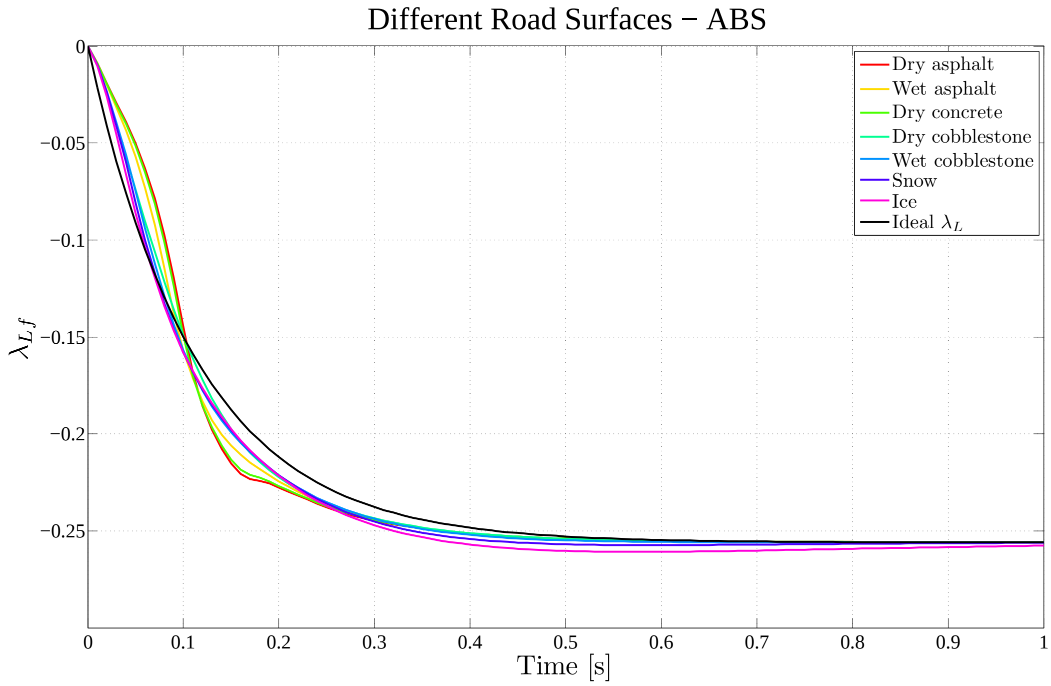

Figure 6.1: Simulated slip response for braking at different road surfaces. Initial condition: $\dot{x}_0 = 130$ $[^{km}/_{h}]$.

It is seen that the slip controller successfully stabilizes the slip at the reference value at all the modeled road surfaces. The slip has settled within 2 % of the reference in 0.4 [s] for all road conditions. This is slightly faster than the predicted settling time of $t_{settle} = 3.9 \cdot \tau_{ABS} = 0.44$ [s].
The impact of changing road condition on the performance of the ABS controller is concluded negligible. The tire-road friction force F_{wxij} changes as the road surface is altered. This change is compensated for as the force is estimated and included in the control law within the slip controller - see Section 5.2.3. The control output is thus adapted to the road condition.

As the vehicle velocity approaches zero, the open-loop slip dynamics become increasingly fast as described in Section 5.1.1. This presents a problem at low vehicle speeds as the phase shift caused by the actuator dynamics and the sampling time becomes significant. The effect is oscillations in the slip response when the vehicle velocity decreases below approximately 10 [$^{km}/_{h}$]. The performance of the ABS controller is therefore concluded unacceptable below this velocity.

The simulated slip response at the rear wheels shows similar results however with a slight increase in settling time due to oscillations caused by the slower actuator dynamics - refer to the plot of front and rear wheel slip response in figure 5.11.

TCS

The TCS is only actuated by the PMSMs (see Section 5.3) and as a consequence it can only stabilize the slip at λ_{opt} for three surfaces: Wet cobblestone, snow and ice - see Section 5.1.1.1. The slip controller is therefore only tested at these surfaces during acceleration. A slip reference of λ_{opt} will simply result in a saturated motor torque and a slip response below the requested value for the remaining road surfaces.

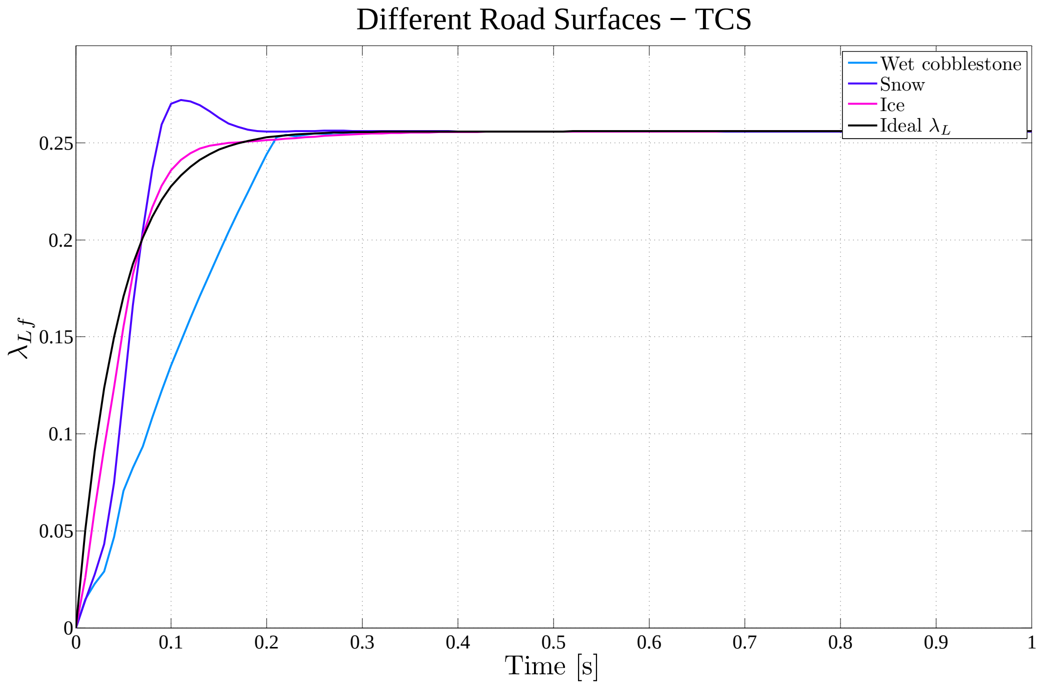

Figure 6.2: Simulated slip response at wet cobblestone, snow and ice. Initial condition: $\dot{x}_0 = 7$ [$^{km}/_{h}$].

The simulated slip responses for the three road surfaces are plotted in figure 6.2. The results correspond to acceleration from an initial vehicle velocity of 7 $[^{km}/_{h}]$. The ideal response is plotted as well.

Again it is seen that the slip controller successfully stabilizes the slip at the reference value for the tested road conditions. The slip has settled within 2 % of the reference in 0.2 $[s]$ for the three road conditions which is slightly slower than the predicted settling time of $t_{settle} = 3.9 \cdot \tau_{TCS} = 0.18$ $[s]$.
The motor torque saturates when the vehicle is accelerating on wet cobblestone as the tire-road friction is high compared to the other surfaces. This leaves little available torque from the PMSMs to accelerate the wheel and increase the slip, hence the increase in settling time at this surface.

The saturation effect is also evident at low friction surfaces if the initial velocity increases. This is due to slower slip dynamics and increasing viscous friction torque. The saturation effect is observed from the plots in figure 6.3. The figure shows the simulated slip response when accelerating on snow using different initial vehicle velocities $\dot{x}_0$ ranging from 7 to 50 $[^{km}/_{h}]$.

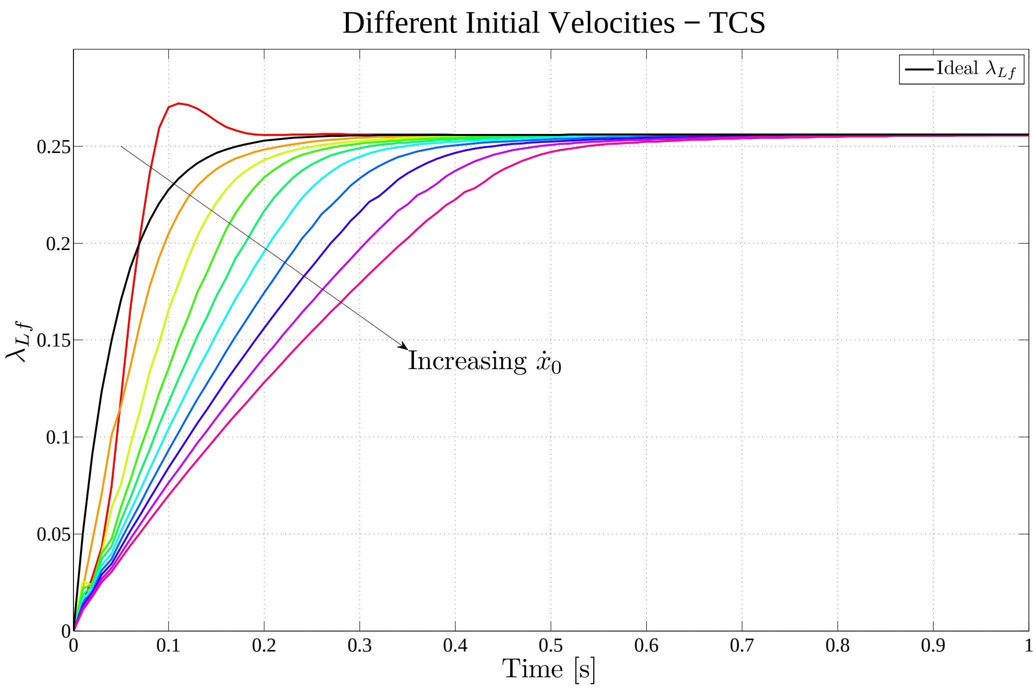

Figure 6.3: Simulated slip response for acceleration on snow with different initial velocities $\dot{x}_0$ in the range 7 to 50 $[^{km}/_{h}]$

Although the slip response deviates from the ideal exponential response as the PMSMs saturate, the anti wind-up scheme effectively compensates for the actuator saturation thereby protecting the system from overshoot of the slip response caused by integrator wind-up.
As in the braking simulation, the the slip response becomes increasingly oscillatory as the vehicle velocities decreases. It is concluded that the performance of the TCS is unacceptable for vehicle velocities below 7 $[^{km}/_{h}]$.

The slip controller has now been tested in different road conditions. It was seen to stabilize the slip response on all road surfaces. The controller robustness to variations in wheel radius, vehicle load and rolling- and drag resistance will now be tested.

6.2 Robustness to Parametric Uncertainties

The TCS and ABS slip controllers are designed to compensate for bounded parametric uncertainties in the parameters m, r, c_{roll} and c_D. The controllers are therefore tested for different values of these parameters. The vehicle mass m affects a variety of parameters as described in Section 3.8. Three operating conditions are chosen to emulate the span of possible load conditions. The three vehicle masses under consideration are: $m = 450$ $[kg]$, $m = 600$ $[kg]$ and $m = 1050$ $[kg]$. The controllers are tested for the three different values of m as well as the minimum and maximum values of r, c_{roll} and c_D. This results in $3 \cdot 2 \cdot 2 \cdot 2 = 24$ different operating conditions in which the system is simulated. The resulting simulated front wheel slip responses are plotted in figure 6.4 for ABS and figure 6.5 for TCS along with the response corresponding to $s = 0$ and the tracking limits imposed by the added boundary layer.
The ABS is tested for braking from an initial vehicle velocity of $\dot{x}_0 = 130$ $[{}^{km}/{}_h]$ on dry asphalt. The TCS is tested for acceleration from an initial vehicle velocity of $\dot{x}_0 = 7$ $[{}^{km}/{}_h]$ on snow. Both road conditions are worst case scenarios (largest oscillations of the slip response).

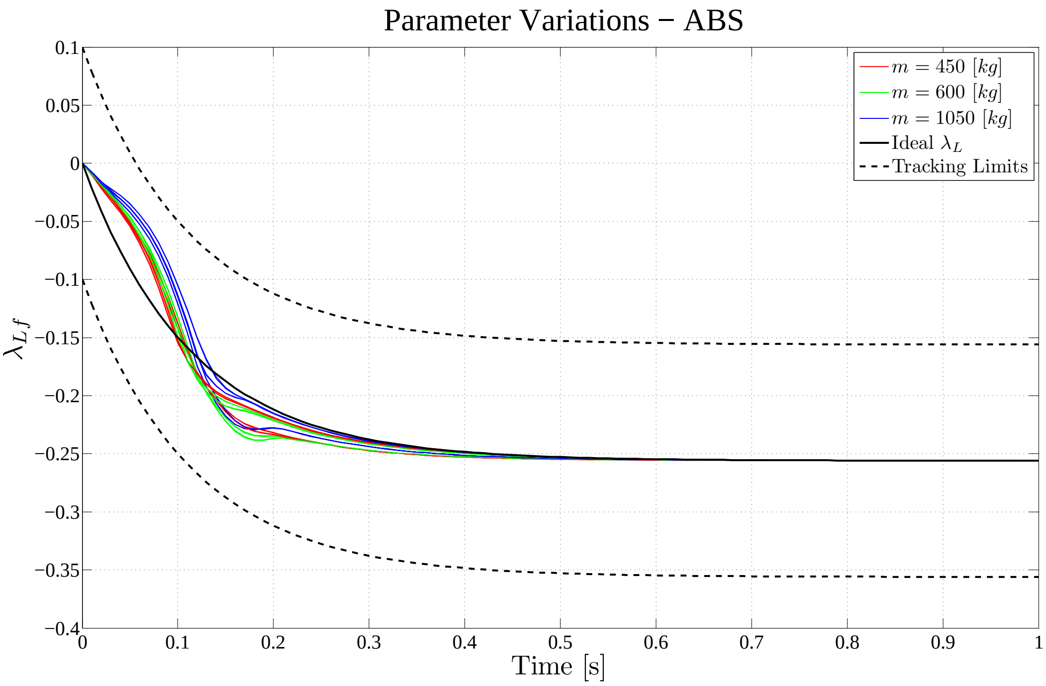

Figure 6.4: Simulated slip response in the 24 different operating conditions. All plots correspond to braking on dry asphalt with initial vehicle velocity $\dot{x}_0 = 130$ $[{}^{km}/{}_h]$.

The slip responses plotted in figure 6.4 and 6.5 show that the slip controller is robust to the parameter variations in all of the simulated operating conditions during both braking and acceleration. Both the ABS and TCS successfully stabilizes the slip at the given reference and the tracking error is within the limits depicted in Section 5.2.4. It is also noted that the tracking performance improves significantly as the slip stabilizes. This is an advantage of using integral sliding mode control over conventional sliding mode control as the integrated error compensates for constant or slowly varying disturbances, much like the integrator within a PI-controller.

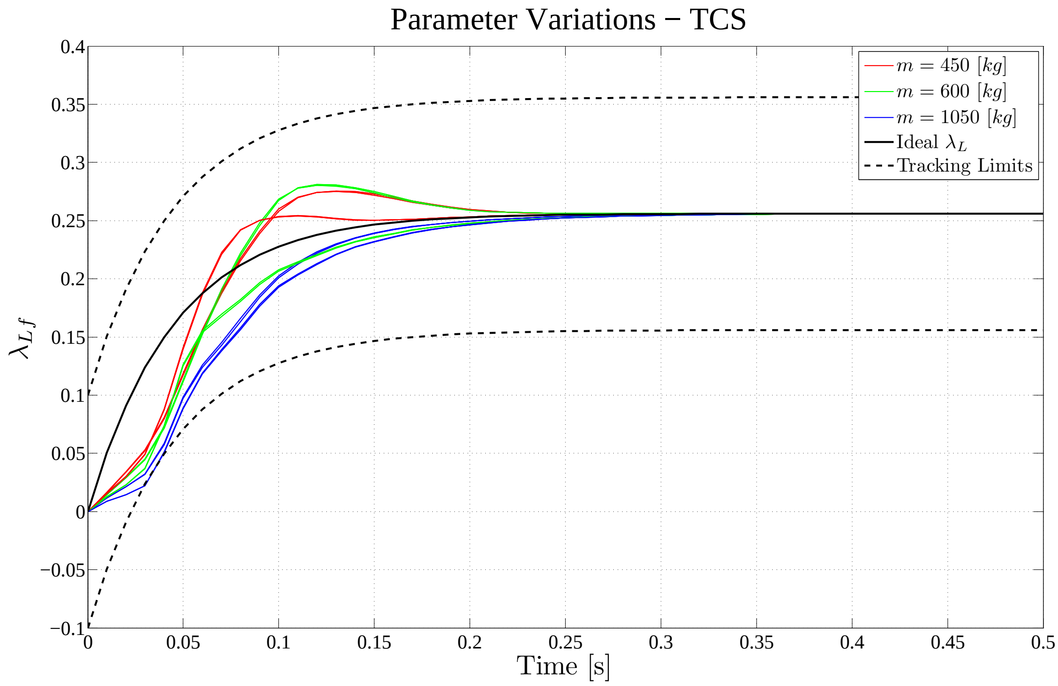

Figure 6.5: Simulated slip response in the 24 different operating conditions. All plots correspond to acceleration on snow with initial vehicle velocity $\dot{x}_0 = 7$ $[{}^{km}/_{h}]$.

It must be noted that only 12 different responses are visible in figure 6.4 and 6.5. The reason is that the variations in c_D result in almost identical responses, i.e. the plots corresponding to $c_D = c_{D,min}$ and $c_D = c_{D,max}$ coincide.
The robustness of the controllers to parameter variations is concluded acceptable.

6.3 Slip Control Under The Influence of Side Slip

The TCS and ABS slip controllers are designed based on the assumption of purely longitudinal motion. In real driving situations lateral and yaw motion naturally occurs as the driver maneuvers the vehicle. The slip controllers are designed to prevent loss of maneuverability due to large slip and must therefore be able to aid the driver in maneuvering the vehicle in spite of side slip.
The slip reference supplied to the slip controllers is designed to maximize the friction utilization during straight driving as well as during cornering. This is achieved by adjusting the longitudinal slip reference according to equation (3.11) with $\lambda_{max,ij} = \lambda_{opt}$. It is therefore tested whether the slip controllers are able to follow the supplied reference in a cornering maneuver.
The TCS and ABS controllers are tested in two different simulated driving situations in order to highlight some of the benefits of the two systems. The simulations are described in the following sections.

6.3.1 Simulation of TCS During Surface Change

The TCS is tested by simulating a driving situation where the vehicle is initially driving on asphalt and enters a patch of snow while negotiating a turn. After driving 1 $[s]$ on snow the surface changes to asphalt again. The short duration of the low friction surface is chosen to simulate a situation where the driver does not react fast enough to compensate for the change in road conditions. The vehicle path is plotted in figure 6.6 for a simulation with TCS enabled and a simulation without TCS enabled. Both situations use the same steering angle input and initial velocity $\dot{x}_0 = 60$ $[^{km}/_{h}]$.

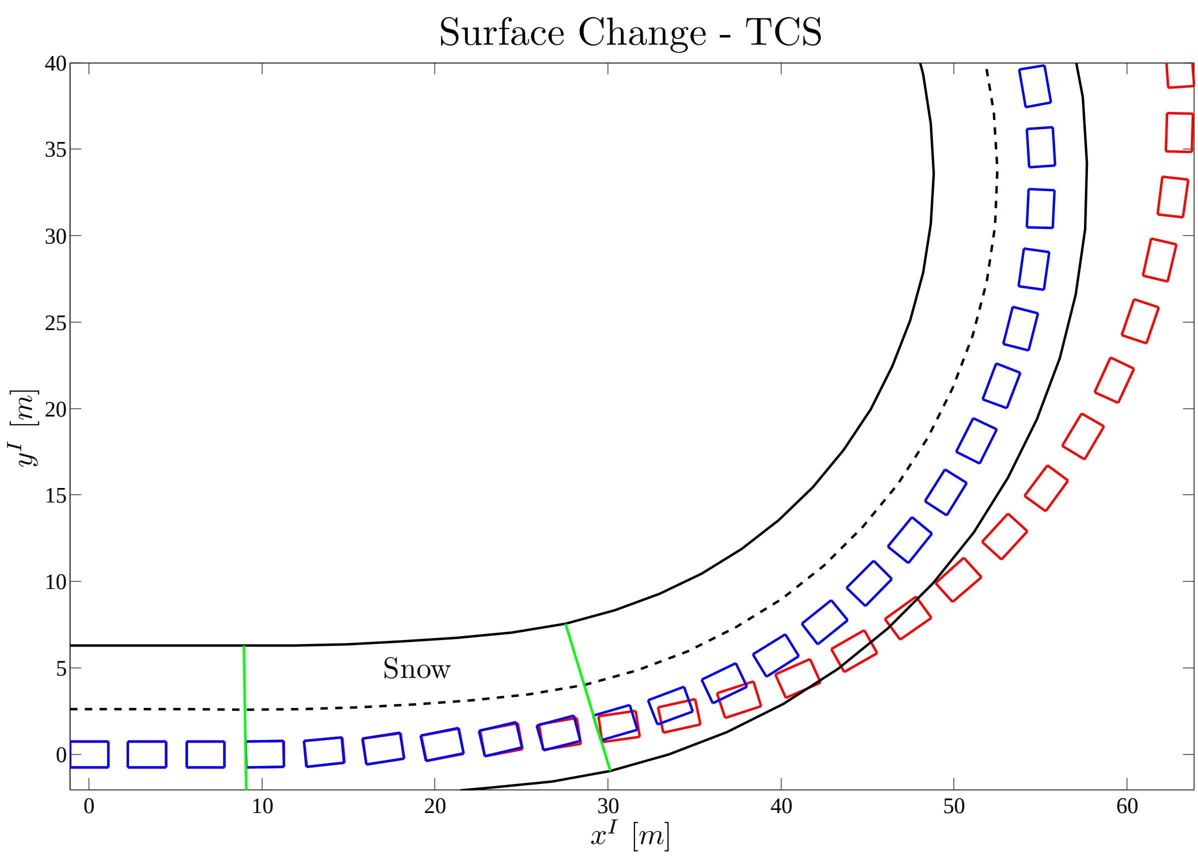

Figure 6.6: Simulated vehicle path in inertial frame with TCS enabled (blue) and without TCS enabled (red). The green lines indicate the snow covered area.

The plots of vehicle paths in figure 6.6 show that the vehicle is able to maintain a sharper curve with the same steering angle if the TCS is enabled.
During stable driving no side slip angle greater than 16° can occur [22, p.325]. The steering angle input is therefore chosen so that the side slip angle reaches a maximum of approximately 16°. This means that if the driver increases the steering angle δ to compensate for the loss of traction, then the side slip angle is increased beyond its limit and the system will become unstable.
The improved traction obtained when using the TCS is illustrated from the plots in figure 6.7 showing the steering angle supplied by the driver, the reference slip (λ_{opt}) and resulting and longitudinal slip response of the two simulations. The green lines indicate when the vehicle enters and leaves the patch of snow covered road.

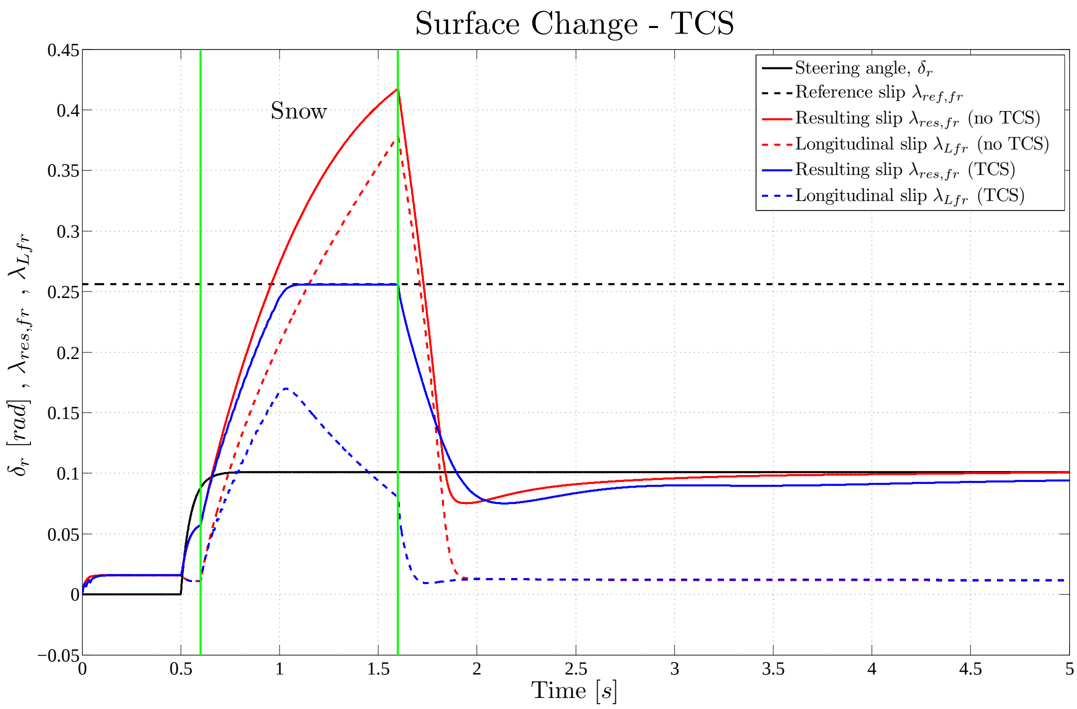

Figure 6.7: Simulated steering angle, reference slip and resulting and longitudinal slip response with (blue) and without (red) TCS enabled. Initial velocity is $\dot{x}_0 = 60$ $[{}^{km}/_{h}]$.

The following is observed from the plots in figure 6.7: As the vehicle is initially driving straight ahead on asphalt the resulting slip cannot reach the reference of 0.256 due to actuator saturation. As the turn is initiated at $t = 0.5$ $[s]$ the side slip angle increases and the friction force acting in the direction of x^{wfr} decreases (see equation (3.10)). The lower friction force enables the PMSMs to increase the slip.
At $t = 0.6$ $[s]$ the vehicle enters the snow covered patch and the reduced friction causes the longitudinal slip to increase. The TCS effectively stabilizes the resulting slip at $\lambda_{opt} = 0.256$ by reducing λ_{Lfr} as the side slip increases. It is seen that the longitudinal slip continues to increase in the simulation without TCS enabled until the vehicle exits the snow covered area. This causes the lateral friction coefficient to decrease - see figure 3.8.
At $t = 1.6$ $[s]$ the vehicle exits the snow covered area and the PMSMs again saturate causing the longitudinal and resulting slip to decrease.

As the side slip angle reaches values near 16° in the simulation with TCS enabled it is concluded that the slip controller is able to stabilize the resulting slip at the reference value in spite of side slip within the range of stable driving.

6.3.2 Simulation of ABS During Evasive Maneuver

The ABS is tested by simulating an evasive maneuver where the vehicle is braking from an initial velocity of $\dot{x}_0 = 130$ $[{}^{km}/_{h}]$ on dry asphalt and changes lane during the braking maneuver. This is done to simulate a collision avoidance situation. The situation is simulated with slip control enabled and with locked wheels ($\lambda_{Lij} = -1$) corresponding to braking with maximum braking torque without ABS. The vehicle path for both simulations is plotted in figure 6.8. The simulations use identical steering angle inputs.

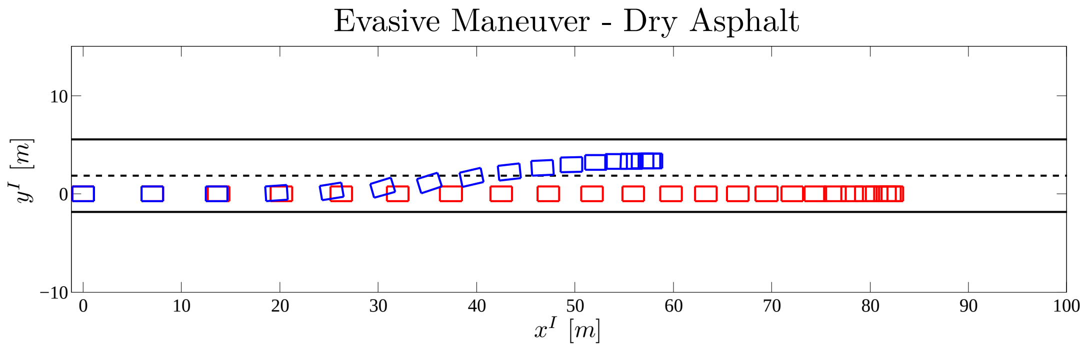

Figure 6.8: Evasive maneuver with (blue) and without (red) ABS enabled. Initial condition: $\dot{x}_0 = 130$ $[km/h]$. Road surface: Dry asphalt.

It is observed from the simulated vehicle paths that the maneuverability is lost when the wheels are blocked. This is in correspondence with figure 3.8. The vehicle is thereby not able to change lane in spite of a nonzero steering angle. In the situation with ABS enabled the wheels are prevented from locking and lateral maneuverability is maintained. It is also noted that the braking distance is reduced from 84.3 $[m]$ to 58.9 $[m]$ when the slip is controlled by ABS. The braking distance is the distance the vehicle travels until it comes to complete stop.

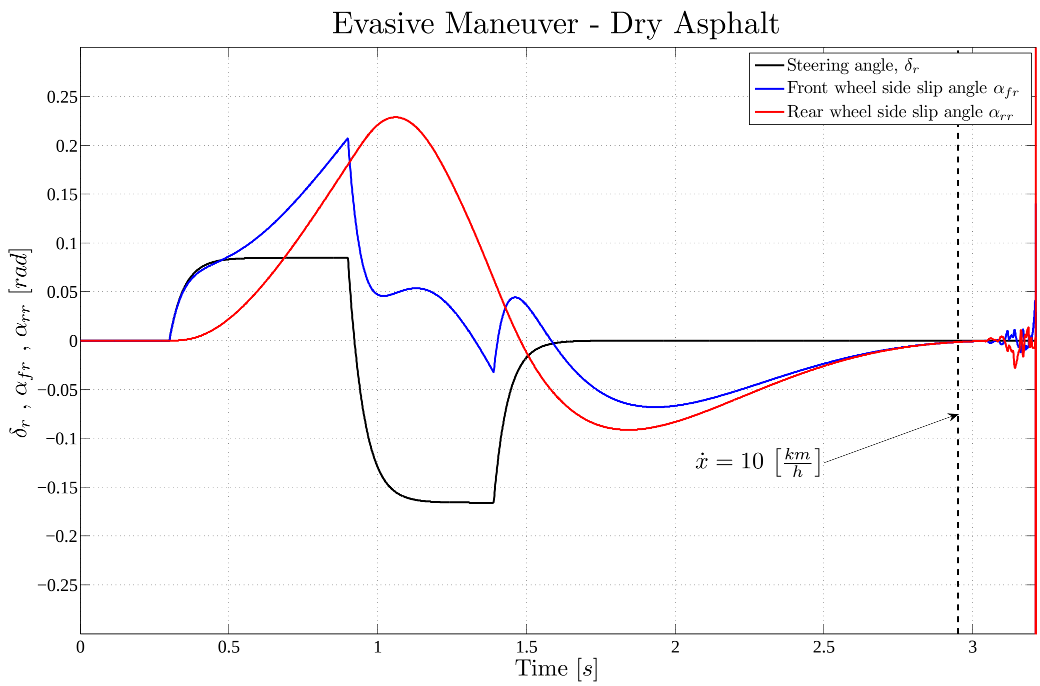

Figure 6.9: Simulated steering angle and side slip angle at right front (blue) and rear (red) wheel. Initial velocity is $\dot{x}_0 = 130$ $[km/h]$. Road surface: Dry asphalt. The dotted line indicates the time instant where the vehicle velocity drops below $\dot{x} = 10$ $[km/h]$.

The steering angle and the side slip angle developed at the right front and rear wheels during the simulated evasive maneuver is plotted in figure 6.9. The plots are only presented for the case where ABS is enabled. The side slip is equal to the steering angle for the case where ABS is disabled.

The side slip angle reaches 0.2287 $[rad]$ (approximately $13°$) at the right rear wheel and varies considerably during the simulation. The controller is thereby tested in a large range of side slips. The reference to the slip controllers at each wheel is therefore varied in order to stabilize the resulting slip at $\lambda_{opt} = 0.256$.
The side slip at the front wheel changes rapidly due to the steps in steering angle. The ability of rejecting step disturbances is therefore tested.
The resulting and longitudinal slip response at the right front and rear wheel is plotted in figure 6.10 along with the reference slip (λ_{opt}) and the steering angle applied at the front right wheel.

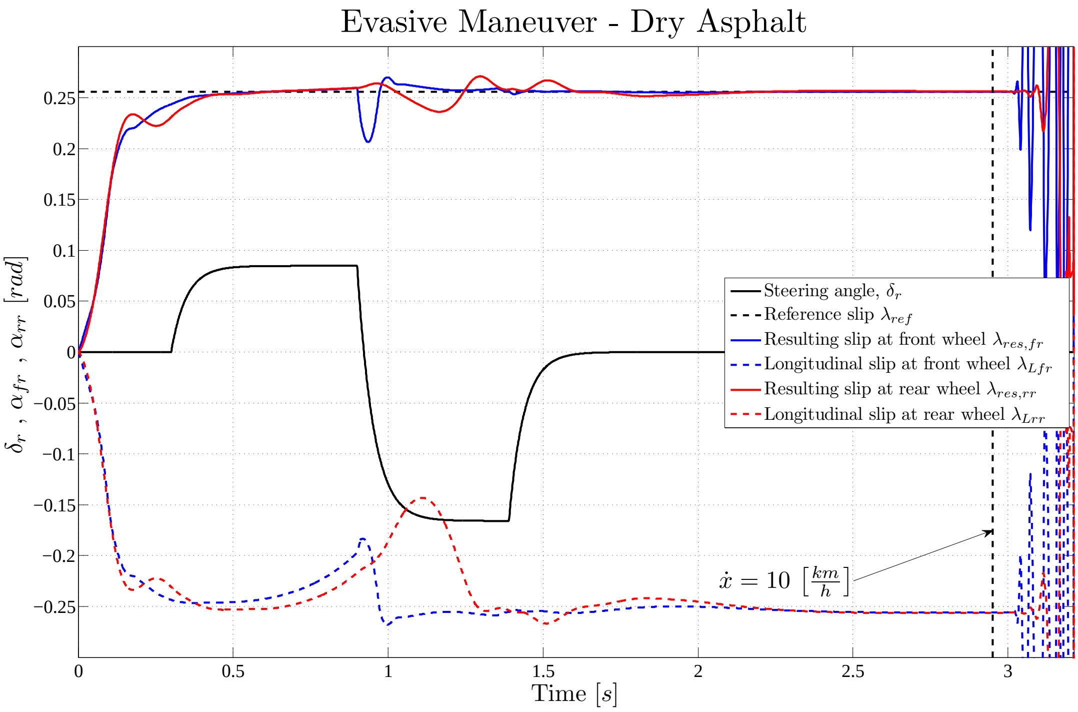

Figure 6.10: Simulated steering angle, reference slip and resulting slip response and longitudinal slip at right front (blue) and rear (red) wheel. Initial velocity is $\dot{x}_0 = 130$ $[km/h]$. Road surface: Dry asphalt. The dotted line indicates the time instant where the vehicle velocity drops below $\dot{x} = 10$ $[km/h]$

It is seen that the slip controller successfully stabilizes the resulting slip at the reference value in spite of varying side slip angle. The tracking error caused by the direction change in steering angle reach a magnitude of 0.0494 at the front right wheel and 0.0198 at the rear right wheel. The 2 % settling time after the steering angle steps are 198 $[ms]$ at the front wheel and 675 $[ms]$ at the rear wheel.
It is observed that the slip responses become increasingly oscillatory as the vehicle velocity falls below approximately $\dot{x} = 10$ $[km/h]$ as mentioned earlier. The system is however able to decrease the braking length of the vehicle significantly in spite of the oscillations and the performance of the controller is concluded acceptable.

6.3.3 Slip Control Under Influence of Noisy Slip Measurements

A drawback of slip control compared to traditional rule based logic ABS control is that good slip measurements are difficult to obtain as noisy velocity signals has great effect on the slip measurement [35, ch.6]. During experiments on a test setup supplied by ECOmove ApS it was observed that the velocity measurements available caused low frequency oscillations on the slip measurement with a magnitude of approximately 0.007. A test showing noise on the angular velocity measurements is foi in Appendix A.2. The performance of the slip controller under influence of noise is therefore tested, by simulating the evasive maneuver described above, with noise added to the controller input slip. A noisy sinusoidal signal comparable to the observed disturbance from figure A.11 is used to simulate the measured noise as it enters the slip controller. The modeled noise signal is plotted in figure 6.11.

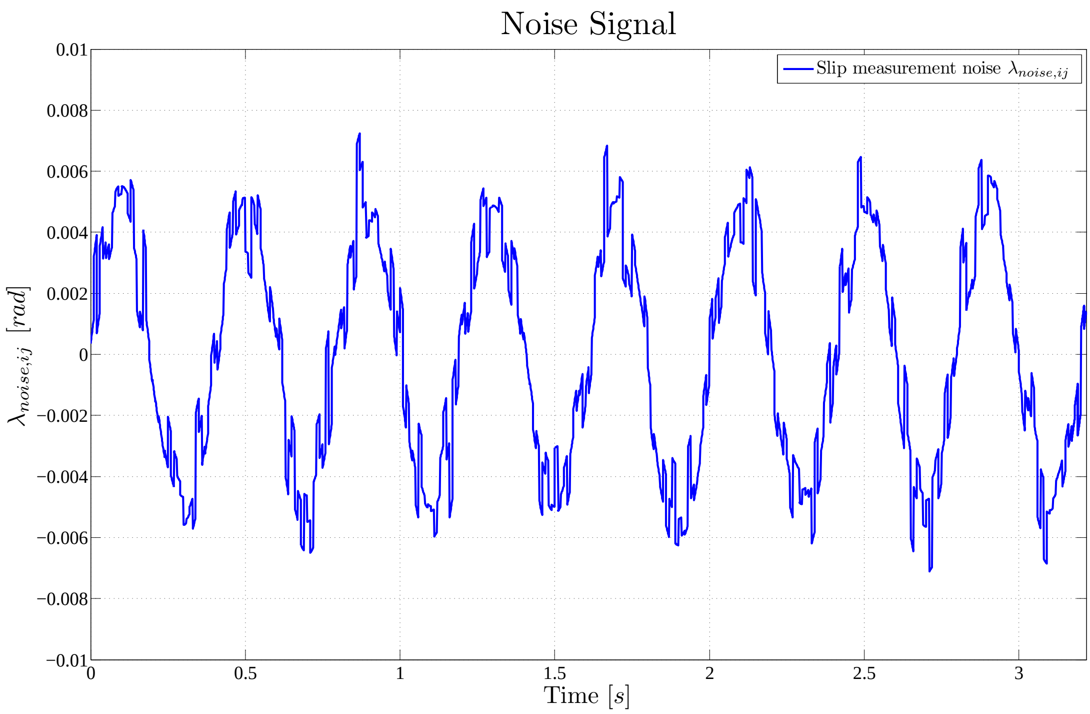

Figure 6.11: Noise signal that is added to λ_{Lij} (at the input to the controller) in simulation.

The slip responses from the simulation are plotted in figure 6.12, they can be directly compared to the responses plotted in figure 6.10. It is seen that the noisy slip measurement has negligible effect at high speeds but become more pronounced as the vehicle velocity decreases and the slip dynamics become faster. It is observed that the rear wheel slip is less affected by the noise as the slower actuator dynamics filter the oscillations. The front wheel slip does however become oscillatory at higher vehicle velocities compared to the noise-free simulation. The braking distance and lateral movement is unaltered (within 0.001 $[m]$) by the addition of noise on the slip measurement. The performance of the slip controller is therefore concluded robust to noisy slip measurements.

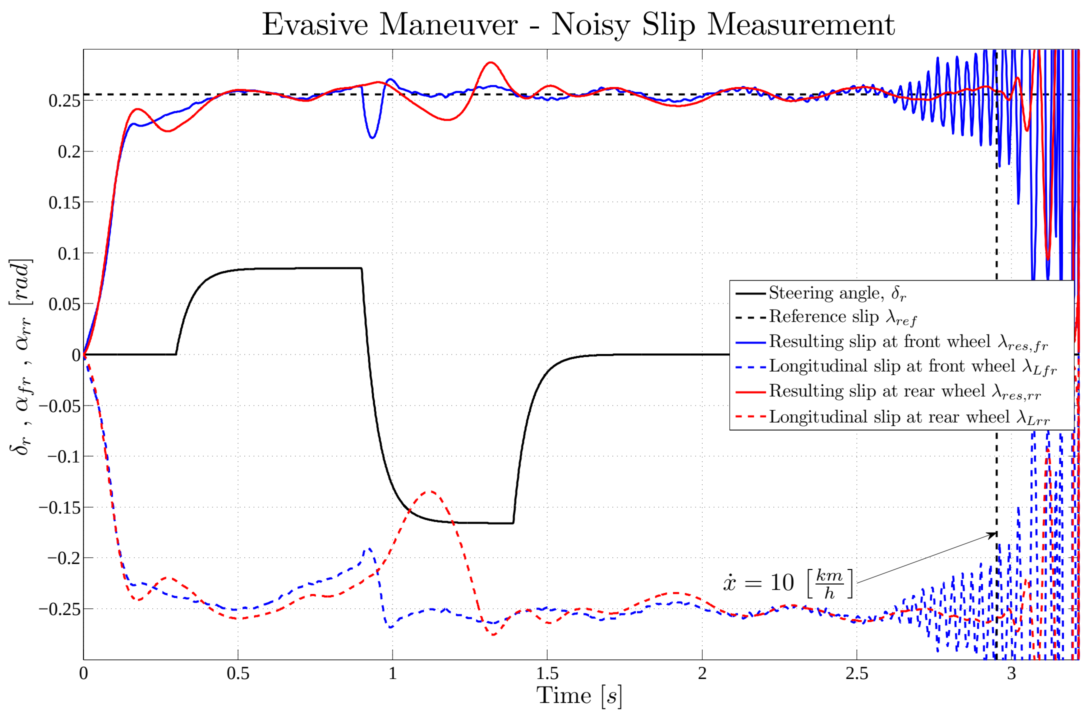

Figure 6.12: Simulated steering angle, reference slip and resulting and longitudinal slip response at right front (blue) and rear (red) wheel under influence of noisy slip measurements. Initial velocity is $\dot{x}_0 = 130$ $[km/h]$. Road surface: Dry asphalt. The dotted line indicates the time instant where the vehicle velocity drops below $\dot{x} = 10$ $[km/h]$

6.4 Braking Distance Reduction

One of the main reasons for designing a ABS is to reduce the distance required to brake the vehicle. The slip controller is therefore tested by simulating straight line braking from 3 three different initial velocities at the 7 different road conditions modeled by the Burckhardt friction model. The simulations are carried out with the maximum vehicle load ($m = 1050$ $[kg]$) to simulate a worst case scenario. Each braking maneuver is simulated with locked wheels (ABS disabled) and with ABS enabled. The simulation results are summarized in table 6.1.

	$\dot{x}_0 = 80$ $[km/h]$		$\dot{x}_0 = 100$ $[km/h]$		$\dot{x}_0 = 130$ $[km/h]$		Average
Road Surface	ABS $[m]$	Locked wheels $[m]$	ABS $[m]$	Locked wheels $[m]$	ABS $[m]$	Locked wheels $[m]$	Braking Improvement %
Asphalt, dry	22.1	32.6	34.3	50.6	56.9	84.3	32.3
Asphalt, wet	32.1	48.2	49.6	74.7	82.4	123.6	33.4
Concrete, dry	23.9	37.4	37.0	58.1	61.4	96.6	36.3
Cobblestone, dry	27.6	35.4	42.4	54.7	70.1	91.3	22.6
Cobblestone, wet	58.2	86.6	89.6	132.7	147.6	216.5	32.4
Snow	111.7	179.4	170.2	269.8	275.1	426.1	36.7
Ice	360.0	420.6	523.5	605.6	786.1	896.5	13.4

Table 6.1: Braking lengths of the QBEAK vehicle with slip control and for blocked wheels. $m = 1050$ $[kg]$.

The average improvement in braking distance varies from 36.7 % down to 13.4 % for a road surface covered with ice. On surfaces with lower friction (such as ice) the slip controller will not be able to improve the braking distance as much because braking force resulting from drag- and rolling resistance are relatively large compared to the tire-road friction force and thus have a bigger impact. Furthermore the difference in friction force at λ_{opt} and $\lambda = -1$ is smaller for ice.

The braking distance limitation of 70 $[m]$ on dry asphalt with $\dot{x}_0 = 100$ $[km/h]$ (introduced in equation (1.1)) is satisfied with and without slip control. The braking distance is however decreased by 16.3 $[m]$ (corresponding to 32.2 %) with the ABS enabled. The safety of the vehicle is therefore significantly improved with the implementation of the proposed slip control system.

7 Conclusion

A robust sliding mode slip controller has successfully been designed for the QBEAK concept vehicle. The controller was designed for a FWD layout and was tuned to deliver a desirable closed-loop slip response for both braking and acceleration of the vehicle in spite of uncertainty in vehicle parameters and road conditions.

The controller performance was tested through simulations in MATLAB Simulink using a dynamic model of the QBEAK vehicle. The model describes the planar vehicle motion and the wheel dynamics. The Burckhardt friction model was used to model the tire-road friction forces. Besides the tractive forces resulting from tire-road friction the model includes drag and rolling resistance and dynamic load transfer between the four wheels. A simplified model was derived on the basis of the dynamic vehicle model in pure longitudinal motion. The simplified model was used to derive a simplified expression for the slip dynamics.
Analysis of the slip dynamics showed that a constant input torque could result in several equilibrium points. The stability of these equilibrium points was concluded to be dependent on their location compared to the peak of the tire-road friction curve. It was shown that a stabilizing closed-loop slip control system would improve the safety of driving by aiding the driver in preventing wheel spin and locked wheels.
During the analysis of the slip dynamics it was also seen that the torque limitations of the PMSMs precluded the ability to utilize all the available tire-road friction at high friction road surfaces during acceleration.
A closed-loop slip control system was designed based on the simplified slip dynamics. The slip control system was designed as an integral sliding mode controller and stability was guaranteed in spite of bounded uncertainty in the following vehicle parameters:

- Vehicle load m
- Tire radius r
- Rolling resistance coefficient c_{roll}
- Drag coefficient c_D

as these parameters were assumed to vary during driving or from drive to drive.

The slip controller was designed to function during both acceleration (TCS) and braking (ABS) as the control law was designed based on a unified expression of the slip dynamics in the two situations. The ABS and TCS was thereby implemented using identical control topologies but with slightly different control parameters to account for the difference in slip and actuator dynamics in the two cases.

The slip controller was modified to reduce the chattering caused by the discrete implementation of the controller. This was achieved by relaxing the guaranteed tracking precision with the implementation of a boundary layer around the sliding surface. Simulations indicated that the chattering was reduced significantly and the control effort was reduced. The tracking error of the slip ratio was guaranteed to be less than or equal to 0.1 at the front wheels and 0.06 at the rear wheels.

An anti wind-up algorithm was designed for the slip controller in order to compensate for integrator wind-up caused by the torque limitations of the PMSMs during acceleration. The proposed anti wind-up scheme involves switching between two control laws depending on whether the PMSMs saturate or not. Simulations showed that the proposed anti wind-up scheme significantly improves the performance of the controller in situations were the PMSMs reach their torque limit.

A torque distribution system was designed to distribute the torque demanded by the slip controller between the PMSMs and the hydraulic brakes during braking. The system was designed to utilize the fast dynamics of the PMSMs and the high braking torque of the hydraulic brakes. It was proposed because the bandwidth of the PMSMs is approximately 13 times higher than the bandwidth of the brakes. Simulations indicated that the dynamic performance could be improved by letting the PMSMs act only on the high frequency content of the torque demand which could not be supplied by the hydraulic brakes. This could be achieved without saturating the actuators.

The slip controller was derived based on the assumption that the tire-road friction force was measurable. An observer was therefore designed to estimate this friction force as it cannot be measured directly. The observer was based on sliding mode control theory and proved stable using Lyapunov stability theory. By using the observer, numerical differentiation of the angular wheel velocity was avoided and it was shown that the friction force could be estimated using only torque and wheel velocity measurements. A boundary layer around the sliding manifold was implemented to reduce chattering of the estimated friction force caused by the observer discontinuity. The boundary layer was shown to effectively reduce the chattering while maintaining acceptable dynamic performance.
Simulations showed that the friction force observer was able to estimate the friction force with less than 5 % error in 0.06 [s] at the front wheels and 0.11 [s] at the rear wheels when a large step in friction force was encountered.
The friction force observer was implemented in a test setup and tested experimentally. The observer was concluded suitable to be implemented in a slip control system and was used to supply the friction force measurement to the slip controller in all simulations. The test journal is found is Appendix A.4.

A friction curve estimator was designed to estimate the friction characteristics during driving. The estimator uses a recursive least squares algorithm to estimate the friction curve based on a linearization of the Burckhardt friction model. The estimator was shown to accurately estimate the friction characteristics in simulations, based on slip measurements and the estimated friction force from the observer. It was shown that the location of the peak of the friction curve could be accurately determined based on the estimated friction characteristics if the inputs to the estimator was persistently exciting. Under this condition the estimator could be used to supply the reference to the slip controller. Simulations did however indicate that the estimator was not able to estimate the friction characteristics accurately when sudden changes in the road surface was encountered. It was therefore concluded that a constant slip reference should be used in order to increase the robustness to changing road conditions. The constant slip reference was chosen as the slip value that would guarantee the highest friction utilization at all the modeled road surfaces. This optimal slip value was determined to be $\lambda_{opt} = 0.256$ and it was shown that at least 93.7 % of the available friction would be utilized at any road surface if the slip was stabilized at this value. It was concluded that $\lambda_{opt} = 0.256$ should be used as a constant slip reference to both the ABS and TCS slip controller.

Using the constant slip reference the slip controller was tested through simulations of different driving conditions using the MATLAB Simulink dynamic vehicle model. The slip controller was able to stabilize the slip at λ_{opt} at every road surface when braking (ABS) and on 3 of the 7 modeled road surfaces when accelerating (TCS). The reference slip could not be reached at the remaining surfaces due to the torque limitation of the PMSMs. It was shown that the simulated closed-loop performance of the slip control system resembled the theoretically predicted performance with comparable settling time in spite of the simplifications made in the design process.

The slip controller was also shown to be robust to variations in the parameters m, r, c_{roll} and c_D within the predetermined uncertainty bounds during both braking (ABS) and acceleration (TCS). The tracking precision was shown to be within the limits imposed by the implemented boundary layer in all operating points. The simulations did however show that the slip response became oscillatory at low vehicle velocities as the slip dynamics became increasingly fast. It was therefore concluded that the ABS should be turned off at vehicle velocities below 10 $[{}^{km}/_{h}]$ and the TCS should only be turned on at vehicle velocities above 7 $[{}^{km}/_{h}]$.

The slip controller was tested in two different simulated driving situations involving lateral motion:

- Simulation of a sudden change in road condition during cornering showed that the slip controller was able to increase the lateral friction force by controlling the slip and thereby preventing wheel spin (TCS). The turn radius could therefore be reduced while maintaining maneuverability of the vehicle compared to a situation were the slip was not controlled.
- Simulation of an evasive maneuver involving braking showed that the slip controller was able to significantly reduce the braking distance and increase the maneuverability of the vehicle (ABS) compared to a situation were the wheels were locked (simulating uncontrolled hard braking).

During experiments it was observed that small disturbances on velocity measurements could cause significant disturbances on the slip measurement. The slip controller was therefore tested with noise added to the slip signal. The simulation showed that the addition of noise to the slip signal caused increasing oscillations at low vehicle velocities but neither the braking distance nor the vehicle maneuverability was affected. The slip controller was therefore concluded robust to measurement disturbances on the slip signal.

Finally a series of straight line braking maneuvers were simulated with the slip controller enabled and disabled (locked wheels). Simulations were carried out for initial velocities of 80, 100 and 130 $[{}^{km}/_{h}]$ on the 7 modeled road surfaces. It was shown that the average reduction in braking distance at the three velocities was between 13.4 and 36.7 % depending on the road conditions.

The slip controller was tested experimentally on a single wheel test setup as described in Appendix A. The tests showed unacceptable performance of the slip controller as large oscillations and unstable behavior of the system slip response was observed. The reason for the deviation from the simulations was investigated and it was concluded that a 240 $[ms]$ delay in the data communication between the slip controller and the motor controller was responsible for the oscillatory response. The delay was included in simulations (see Appendix A.5) and it was observed that the delay resulted in instability in simulations as well. It was therefore concluded that the delay should be reduced to permit effective slip control. During the test period it was not possible to reduce the delay as the exact reason for the delay could not be located.

In spite of unsatisfactory test results the slip controller has proven to be a reliable controller through simulations. However even if the data communication delay is reduced to an acceptable extend issues still remain in estimating the vehicle velocity as well as designing a closed-loop brake pressure control system. These issues should be addressed before implementing the slip controller in the QBEAK vehicle. Further testing should be done regarding how roll and pitch motion affects the controller since this was not included in neither simulations nor tests.

The slip controller was designed with the QBEAK as a specific case study but the theory is applicable to EVs in general with the change of a few parameters. As is the proposed torque distribution system and the anti wind-up scheme.

Bibliography

[1] Regulation No 13-H - Uniform provisions concerning the approval of passenger cars with regard to braking, . URL http://eur-lex.europa.eu/LexUriServ/LexUriServ.do?uri=CELEX:42010X0831(02):EN:HTML.

[2] Mathworks - product support, . URL http://www.mathworks.se/support/tech-notes/1500/1510.html.

[3] Global technical regulation no. 8: Agreement concerning the establihment of global technical regulations for wheeled vehicles, equipment and parts which can be fitted and/or be used on wheeled vehicles - electronic stability control systems, .

[4] Council directive 71/320/eec, 06 1971.

[5] Altairnano. Power to innovate. URL http://www.altairnano.com/Profiles/Investor/Investor.asp?BzID=546&from=dl&ID=125082&myID=125082&L=i&Validate=3&I=.

[6] Mads Hellegaard Andersen, Rune Wiben, and Thomas Schmidt. The use of a permanent magnet synchronous motor in an emulated active heave compensated system. Technical report, Aalborg University, 2011.

[7] Advanced Vehicle Testing Activity (AVTA). How do gasoline & electric vehicles compare? URL http://avt.inl.gov/pdf/fsev/compare.pdf.

[8] BMW. Bmw i3 concept - the megacity vehicle, 02 2012. URL http://www.bmw-i.com/en_ww/bmw-i3/.

[9] Carlos Canudas-De-Wit, Panagiotis Tsiotras, Efstathos Velenis, Michel Basset, and Gerard Gissinger. Dynamic friction models for road/tire longitudinal interaction. Technical report, Georgia Institute of Technology, 2002.

[10] Sabri Cetinkunt. *Mechatronics*. John Wiley & Sons, Inc, 2007.

[11] Sergey Drakunov, Ümit Özgüner, Peter Dix, and Behrouz Ashrafi. Abs control using optimum search via sliding modes. *IEEE Transaction on Control Systems*, 3, 1995.

[12] ECOmove. Ecomove vehicles - requirement specification. Technical Report Rev. 18, ECOmove ApS, 2012.

[13] Ford. Be Among The First To Reserve The 2012 Focus Electric, 02 2012. URL http://www.ford.com/electric/focuselectric/2012/.

[14] Jason J. Ford. Introduction to system identification. (4):10, September 2011. Lecture notes for ENN580 at Queensland University of Technology.

[15] Thomas D Gillespie. *Fundamentals of Vehicle Dynamics*. Society of Automotive Engineers Inc., 1992.

[16] Reza N Jazar. *Vehicle Dynamics Theory and Application*. Springer, 2008.

[17] Lasse G Jensen. Se den danske elbil med fire motorer. *Ingeniøren*, 11 2011. URL http://ing.dk/artikel/124046-se-den-danske-elbil-med-fire-motorer.

[18] Tor A Johansen, Idar Petersen, Jens Kalkkuhl, and Jens Lüdemann. Gain-scheduled wheel slip control in automotive brake systems. *IEEE Transaction on Control Systems*, 11, 2003.

[19] Li Junwei and Wang Jian. Design of antilock braking system based on variable structure control. *IEEE Intelligent Computing and Intelligent Systems*, 2009.

[20] Li Junwei and Wang Jian. Research on the automotive ebd system based on fuzzy control. *IEEE Computer Engineering and Technology*, 2010.

[21] Kia. Electric vehicle (ev), 02 2012. URL http://www.kiamotors.com/experience-kia/environment/ev.aspx.

[22] Uwe Kiencke and Lars Nielsen. *Automotive Control Systems For Engine, Driveline and Vehicle*. Springer, 2005.

[23] AECOM Australia Pty Ltd. Economic viability of electric vehicles. Technical report, Department of Environment and Climate Change, 09 2009.

[24] Gong Mingde and Wang Tianxu. Simulation of full power hydraulic brake system for engineering vehicles. *IEEE Consumer Electronics, Communications and Networks*, 2011.

[25] Mitsubishi. Plug into the future today with i-miev, 02 2012. URL http://www.mitsubishi-motors.com.au/vehicles/cars/i-miev.

[26] Nissan. Nissan leaf - 100URL http://www.nissanusa.com/leaf-electric-car/index.

[27] Official Journal of the European Union. Regulation (ec) no 443/2009, 04 2009. URL http://europa.eu/legislation_summaries/transport/transport_energy_environment/mi0046_en.htm.

[28] Official Journal of the European Union. Directive 2009/33/ec, 04 2009. URL http://europa.eu/legislation_summaries/transport/transport_energy_environment/en0011_en.htm.

[29] oilprice.com. Daily OHLC Chart, 02 2012. URL http://oilprice.com/commodity-price-charts.

[30] M Oudghiri, M Chadli, and A El Hajjaji. Robust fuzzy sliding mode control for antilock braking system. *International Journal on Science and Techniques of Automatic Control*, 1, 2007.

[31] Charles L Phillips and Royce D Harbor. *Feedback Control Systems 4th Edition*. Prentice Hall, 2000.

[32] Karl Popp and Werner Schielen. *Ground Vehicle Dynamics*. Springer, 2010.

[33] Rajesh Rajamani. *Vehicle Dynamics and Control*. Springer, 2006.

[34] Renault. The electric vehicle, a global strategy, 02 2012. URL http://www.renault.com/en/capeco2/vehicule-electrique/pages/vehicule-electrique.aspx.

[35] Sergio M. Savaresi and Mara Tanelli. *Active Braking Control Systems Design for Vehicles*, volume 1. Springer, 07 2010.

[36] Li Shoubo, Liao Chenglin, Chen Shanglou, and Wang Lifang. Traction control of hybrid electric vehicle. *IEEE*, 2009.

[37] Howard Slater. Setting up pmac software, 17-09 2009. Gen4 application note.

[38] Jean-Jacques E Slotine and Weiping Li. *Applied Nonlinear Control*. Prentice Hall, 1991.

[39] Trafikstyrelsen. Bekendtgørelse om detailforskrifter for køretøjers indretning og udstyr, 04 2012. URL http://www.trafikstyrelsen.dk/DA/Syn-og-K%C3%B8ret%C3%B8jer/Regler-om-k%C3%B8ret%C3%B8jer/Regler-om-koeretoejer/~/media/B57699F6D29743B9A3713FE30730D422.ashx.

[40] Ming-Ji Yang, Hong-Lin Jhou, Bin-Yen Ma, and Kuo-Kai Shyu. A cost-effective method of electric brake with energy regeneration for electric vehicles. *IEEE Transaction on Industrial Electronics*, 56(6):10, 06 2009.

[41] Kierownik Zakladu. Integral anti-windup for pi controllers. URL http://www.isep.pw.edu.pl/ZakladNapedu/lab-ane/anti-windup.pdf.

[42] Kai Zheng, Tielong Shen, and Yu Yao. A robust nonlinear control approach for the traction problem in electrical vehicles. *IEEE Vehicle Power and Propulsion Conference*, 2006.

A Test Journals

A.1 Test Setup

A series of experiments are conducted on a test setup in the laboratory at ECOmove ApS to determine motor and wheel parameters and test the friction force observer and slip controller designed in Section 5.4 and 5.2 respectively. For this purpose ECOmove has constructed a test setup used to simulate driving situations for a single wheel on the QBEAK vehicle.

The test setup is illustrated in figure A.1 and A.2. It consists of two wheels: A large wheel and one of the front wheels from the QBEAK vehicle. The entire driveline of the QBEAK vehicle is attached to the front wheel so that it corresponds to a real driving situation during longitudinal driving. The front wheel suspension is attached to a plate which is able to move vertically. It is then placed on top of the large wheel - which is named the Road Simulation Wheel (RSW) . The RSW is supported by a rigid axle and has a 3.5 $[cm]$ thick circular iron plate attached to increase its inertia. It is used to simulate the road condition and the equivalent mass of the QBEAK vehicle. The driving wheel acts on the RSW through friction in the contact patch between the wheels, thus simulating the tire-road friction of a real driving or braking situation.

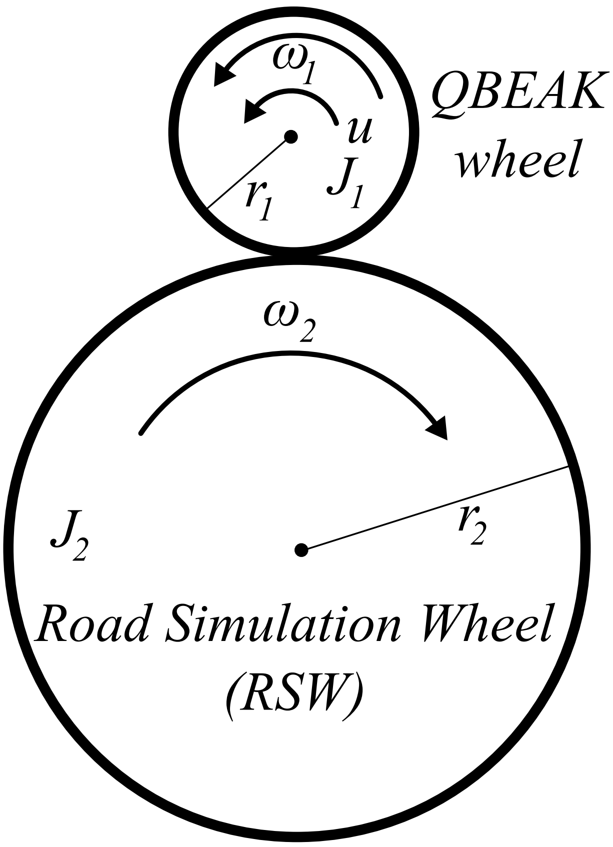

Figure A.1: Sketch of the test wheels.

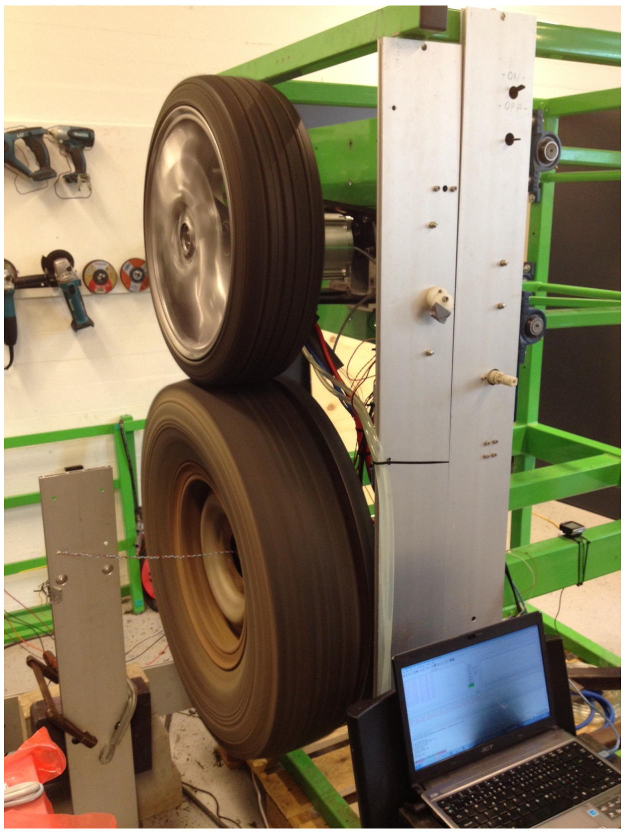

Figure A.2: Picture of the test wheels.

Test diagram

A Sevcon Gen4 motor controller is used to control the torque of the PMSM using a built in PI-controller. A laptop is used to:

- Configure the motor controller through an IXXAT USB-to-CAN interface.
- Receive velocity and torque information through an NI USB-8473 CAN interface.
- Supply torque demands to the motor controller and receive velocity information of the RSW using a NI USB-6215 Data Acquisition (DAQ) box.

The NI USB-8473 and IXXAT USB-to-CAN communicates via CAN-bus using CANopen protocol. The IXXAT USB-to-CAN is used to configure the inputs/outputs and safety limits of the Gen4 motor controller. This is achieved by sending Service Data Objects (SDOs) to the controller. It is only done once to setup the system using the program Shiroko Design Verification Test System (DVT) - software used to configure CANopen devices.
The primary configuration is the mapping of data packages containing torque and velocity measurements of the PMSM as well as a status word indicating the system state. The data is mapped to a Process Data Object (PDO) which is transmitted at a rate determined by the synchronization time and read at every sampling instant using the NI USB-8473.
The torque demands are transmitted with the DAQ box as an analog throttle voltage with the direction controlled by two BC546 Bipolar Junction Transistors (BJTs). The angular velocity of the RSW is measured using an optical switch mounted at the RSW axle and is received by the NI USB-6215.

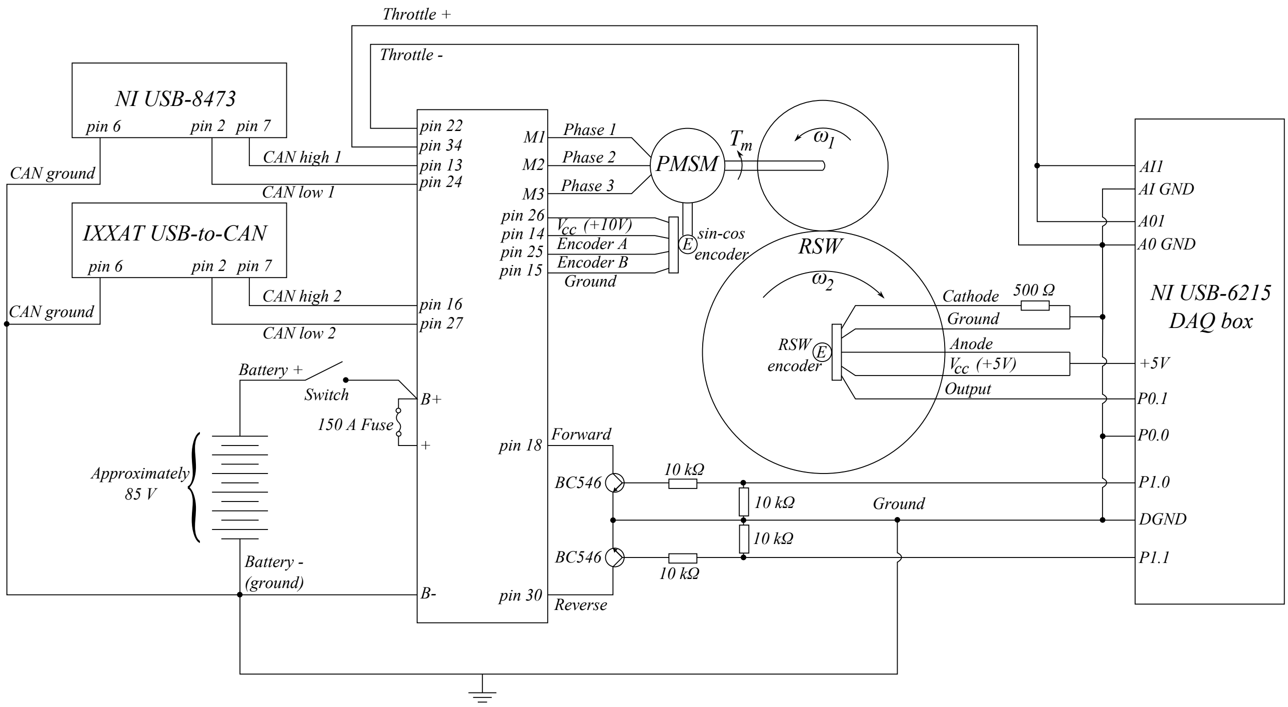

Figure A.3: Schematic of test diagram.

The USB outputs from the NI USB-6215 and NI USB-8473 are read by a LabVIEW program in the laptop. This program has been designed to process the input data and is described in Appendix B. The program is also used to control the outputs of the NI USB-6215 and thereby the reference torque to the Gen4 motor controller. A schematic of the test diagram is seen in figure A.3.

Wheel Dimensions and Masses

Both wheels have been measured and weighed before they are attached to the frame. The wheel dimensions and masses can be seen in table A.1.

	Qbeak front wheel driveline (incl mounting plate)	Road Simulation Wheel (incl circular iron plate)
Mass	93 $[kg]$	$135+35.70=170.7$ $[kg]$
Radius	0.285 $[m]$	0.41 $[m]$

Test Setup vs Vehicle Model

The RSW is - as mentioned above - used to emulate the equivalent mass m_v of the QBEAK vehicle. This mass represents the mass that must be accelerated/decelerated by the actuators during driving. A dynamic model describing the test setup is compared to the simplified longitudinal vehicle dynamics developed in Section 5.1 to highlight the equivalence of the two systems.

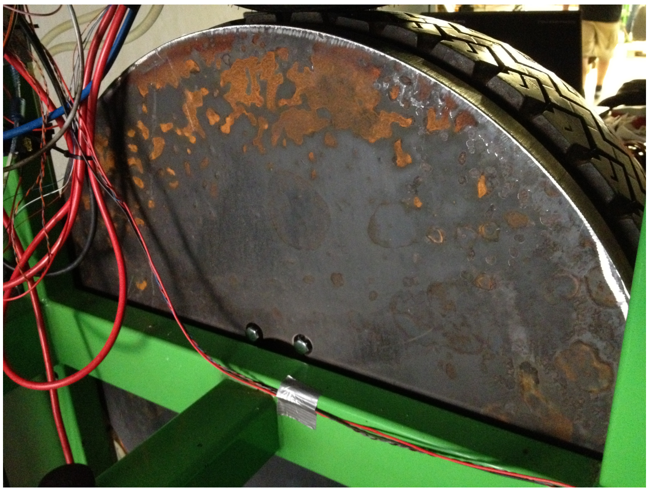

Figure A.4: Road Simulation Wheel as seen from behind the test setup. A circular iron plate is attached to the back of the wheel to increase its inertia. The wheel axle is attached to the green frame.

The simplified vehicle model for purely longitudinal motion is described in equation (5.2) to (5.4). Neglecting roll and drag resistance the equations state:

$$J_{wi} \cdot \dot{\omega}_{ij} = -r \cdot F_{xij} + u_{ij}$$

$$\frac{m}{2} \cdot \ddot{x} = F_{xij} \qquad \text{TCS} \tag{A.1}$$

$$\frac{m}{4} \cdot \ddot{x} = F_{xij} \qquad \text{ABS}$$

These simplified equations are to be compared with the torque balances for the test setup (see figure A.1):

$$\begin{aligned} J_1 \cdot \dot{\omega}_1 &= u - r_1 \cdot m_1 \cdot g \cdot \mu_L \\ J_2 \cdot \dot{\omega}_2 &= r_2 \cdot m_1 \cdot g \cdot \mu_L \end{aligned} \tag{A.2}$$

where J_1 and J_2 are the inertias of the two wheels, r_1 and r_2 are the radii (assumed constant for every test) and ω_1 and ω_2 are the angular velocities.

Equation (A.2) can be rewritten by noting that the circumferential velocity of the RSW is $\dot{x} = r_2 \cdot \omega_2$, thus $\ddot{x} = r_2 \cdot \dot{\omega}_2$ (as r_2 is constant). This yields:

$$\begin{aligned} J_1 \cdot \dot{\omega}_1 &= u - r_1 \cdot m_1 \cdot g \cdot \mu_L \\ \frac{J_2}{r_2^2} \cdot \ddot{x} &= m_1 \cdot g \cdot \mu_L \end{aligned} \tag{A.3}$$

It is seen that equation (A.3) is equal to equation (A.1) with the following substitutions:

Test		Model	
J_2/r_2^2	=	$m/2$	(TCS)
		$m/4$	(ABS)
J_1	=	J_{wi}	
$m_1 \cdot g$	=	F_{zij}	
r_1	=	r	

Thus, in order to represent a realistic driving situation the equalities stated above should be satisfied. Furthermore the friction between the driving wheel and the RSW should match a realistic tire-road friction.

As the driving wheel is a front wheel from the QBEAK vehicle $r = r_1$ is satisfied and $J_w = J_1$ is satisfied for the front wheels.

The normal force F_z acting in the tire-road contact patch during driving has static and dynamic components. The dynamic components are not simulated in the tests but the static part can be changed by adding weights to the driving wheel mounting plate, thereby increasing m_1. However, as no brakes are mounted on the test setup, the available torque at the wheel axle is low compared to a real life driving situation. In order to avoid torque saturation the normal force will be kept at a minimum in the tests as this force acts as a scaling factor on the friction torque that must be balanced by the PMSM.
The resulting normal force acting in the contact patch is $F_z = m_1 \cdot g = 913.26$ $[N]$. For comparison, the static normal force experienced by a front wheel when driving with a total vehicle mass of 600 $[kg]$ is $F_{z,stat,f} = \frac{l_r \cdot m \cdot g}{2 \cdot L} = 1473$ $[N]$.

The equivalent mass m_v is different for driving and braking situations. This is not simulated in the tests. However, the magnitude of $m_v = {}^{J_2}\!/_{r_2^2}$ is very decisive for the validity of the tests. The equivalent mass must be high enough to allow the dynamics of $\dot{x}$ to be neglected. Furthermore, if the equivalent mass is too low, it is difficult to develop slip using the torque developed by the PMSM. Finally, a low equivalent mass results in a fast acceleration/deceleration of the RSW making it difficult to obtain useful test results within the allowable wheel velocities.

Figure A.5: Test setup.

A.2 Determination of Gearing Ratio and Validation of Angular Velocity Measurements of the RSW.

Purpose of the Test

An optical switch is implemented to measure the angular velocity of the RSW. The accuracy of the angular velocity is validated using a stroboscope light sensor, measuring constant angular velocities.
The angular velocity of the QBEAK wheel is also measured using the stroboscope sensor. The gearing ratio between the PMSM and the driving wheel is determined by comparing the output of the sin-cos encoder mounted in the PMSM to the angular velocity of the QBEAK wheel measured using the stroboscope sensor.

Theory

RSW Optical Switch

The output of the optical switch is a pulse train with frequency f_{pulse} proportional to the angular velocity of the wheel. The switch gives 43 pulses pr. revolution (ppr). Thus the angular velocity of the RSW can be calculated as:

$$\omega_2 = \frac{f_{pulse} \cdot 2 \cdot \pi}{ppr} \tag{A.4}$$

In equation (A.4) it is assumed that the encoder ring is exactly centered at the wheel axle. If the ring is misaligned the instantaneous frequency measurement will not be proportional to the angular velocity. This is illustrated in figure A.6 showing a misaligned encoder ring. The ring is divided into 4 quadrants of 90 degrees each. Thus each quadrant corresponds to a 90 degree rotation of the wheel. In this example the figure indicates that quadrant 1 and 2 contains 9 holes each and therefore give 9 pulses per 90 degrees. Quadrant 3 and 4 contains 6 holes and therefore give 6 pulses per 90 degrees. This results in a varying frequency measurement for a constant angular velocity. The average of the frequencies over one revolution will be proportional to the angular velocity.

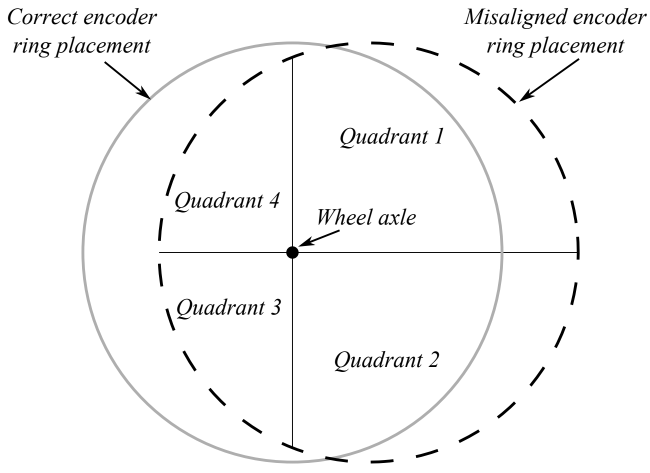

Figure A.6: Illustration of misaligned encoder ring.

A misaligned encoder ring causes measurement disturbances of angular frequency equal to that of the rotating wheel. This low frequency disturbance cannot be eliminated through low-pass filtering without causing severe phase shift of the signal.

Besides the low frequency disturbance caused by encoder ring misalignment, the output is also susceptible to noise caused by the switching of high current signals in the motor controller. This is filtered using two different filters in series. The first filter neglects measurements where the difference between the previous and actual measurement is above a given threshold. This filter does not introduce any phase shift for measurements within the threshold. The second filter is chosen as a 4th order Butterworth low-pass filter. This filter has unity gain through a large port of the passband without amplifying the signal at any frequencies. A filter cut-off frequency of 5 $[Hz]$ has been used in the tests.

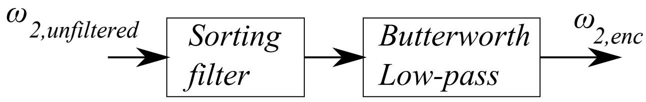

Figure A.7: Block diagram of the filters acting on ω_2.

The angular velocity obtained from the filtered encoder signal $\omega_{2,enc}$ is compared to RPM measurements obtained using a stroboscope $\omega_{2,strob}$. The RPM-signals are converted to angular velocity measurements as:

$$\omega_{2,strob} = \frac{RPM_{strob} \cdot 2 \cdot \pi}{60} \tag{A.5}$$

where RPM_{strob} is the stroboscopic RPM measurement of the RSW.

PMSM Encoder and Gearing Ratio

The gearing ratio of the QBEAK wheel is found by comparing the output of the sin-cos encoder (which is a 32-bit RPM measurement obtained from the motor controller via CAN communication) to a stroboscope RPM measurement. The gearing ratio n is found as:

$$n = \frac{RPM_{PMSM}}{RPM_{strob}} \tag{A.6}$$

where RPM_{PMSM} is the RPM measurement obtained from the sin-cos encoder and RPM_{strob} is the stroboscopic RPM measurement of the driving wheel. RPM_{PMSM} is filtered using the Butterworth low-pass filter with a cut-off frequency of 5 $[Hz]$.

When measuring the angular velocity using a stroboscope light a point on the wheel is marked and the frequency of the light is adjusted until the point seems stationary because the frequency of the light and the wheel rotation is the same. The velocity is constant when the point seems stationary without changing the frequency of the light.

Apparatus used in the test

The components used in the test are listed in table A.1.

Apparatus	Description	Comments
Road Simulation Wheel (RSW)	Large wheel used to simulate the road surface and vehicle inertia	Consist of a rubber tire with a rough tread pattern, an iron rim and a circular iron plate attached to the back of the wheel (see figure A.4)
Encoder Ring	Ring with 43 holes	Attached to the RSW hub.
Optical Switch (OPB917)	Photologic circuit actuated by an Infrared LED	The switch is a 2 state device actuated by the holes in the encoder ring attached to the RSW
IBM Lenovo T61	Laptop	The program LabVIEW is used during test
ATE FS106/100/6	3-phase, PMSM-motor	The peak torque is 19.1 $[Nm]$ and the rated speed is 13000 $[rpm]$
Sevcon Gen4	Motor controller (incl. inverter)	Communicates via CAN-bus
UVW-Encoder	Absolute encoder (Sin-Cos)	Located in the PMSM
Motor-wheel gear	Belt-gear	
Stroboscope RPM sensor	Measures angular velocity using stroboscope light	Precision is 1 [RPM]
NI USB-8473 Interface	High speed USB to CAN interface	The maximum transfer rate is 1000 $[^{kbit}/_{s}]$
NI USB-6210	Data Acquisition Box	The resolution is 16 $[bit]$, the maximum sample rate is 250 $[^{kS}/_{s}]$ for both input and output terminals

Table A.1: Apparatus used to determine the angular velocity of the RSW.

Datasheets of the components listed in the table above can be found on the attached CD (see appendix C).

Test Method

The test setup described in Appendix A.1 is used. The QBEAK wheel is accelerated up to a constant velocity by a step in the torque reference to the PMSM. When the wheel angular velocity is constant, measurements from the sin/cos encoder are compared to stroboscope measurements of the wheel RPM. Based on these measurements the gearing ratio can be determined (see equation (A.6)).
A similar test is carried out for the RSW. Here the RSW is accelerated up to a constant angular velocity by

the QBEAK wheel. Measurements of the constant angular velocity from the RSW encoder is compared to measurements from the stroboscope. Both tests are carried out for different steps in torque reference and thus reaches different constant velocities.
The tests are summarized in table A.2 below.

Test	Description	Logged Data
1	Measurement of the angular velocity of the driving wheel (via CAN)	RPM_{PMSM} $[RPM]$, RPM_{strob} $[RPM]$
2	Measurement of the angular velocity of the driving wheel (via CAN)	RPM_{PMSM} $[RPM]$, RPM_{strob} $[RPM]$
3	Measurement of the angular velocity of the driving wheel (via CAN)	RPM_{PMSM} $[RPM]$, RPM_{strob} $[RPM]$
4	Measurement of the angular velocity of the driving wheel (via CAN)	RPM_{PMSM} $[RPM]$, RPM_{strob} $[RPM]$
5	Measurement of the angular velocity of the RSW (via DAQ box)	$\omega_{2,enc}$ $[^{rad}/_{s}]$, RPM_{strob} $[RPM]$
6	Measurement of the angular velocity of the RSW (via DAQ box)	$\omega_{2,enc}$ $[^{rad}/_{s}]$, RPM_{strob} $[RPM]$

Table A.2: Different tests of the sliding mode friction force observer.

Figure A.8: Picture of the optical switch connected and the encoder ring attached to the wheel.

Data Recording

The logged data is plotted in the figures below. Only selected tests are shown. The neglected tests showed similar results, although it should be noted that in Test 1 and 2 the measured angular velocity did increase slightly - with 5 to 10 $[RPM]$ - during the tests.

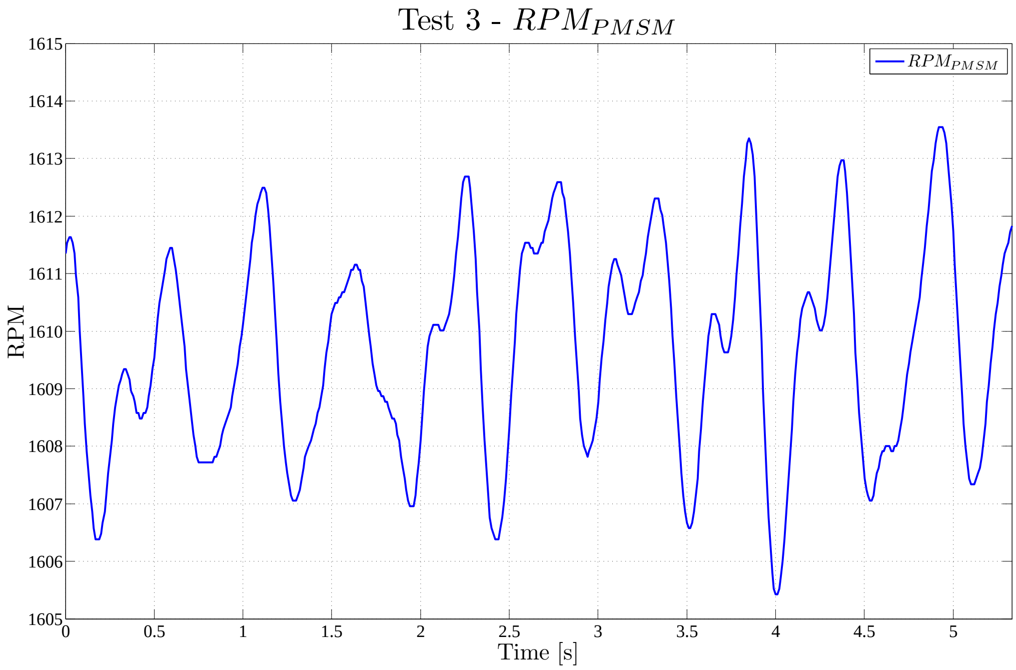

Figure A.9: Test 3: RPM measurements of the PMSM. The stroboscope measurement is $RPM_{strob} = 155.43$ $[RPM]$.

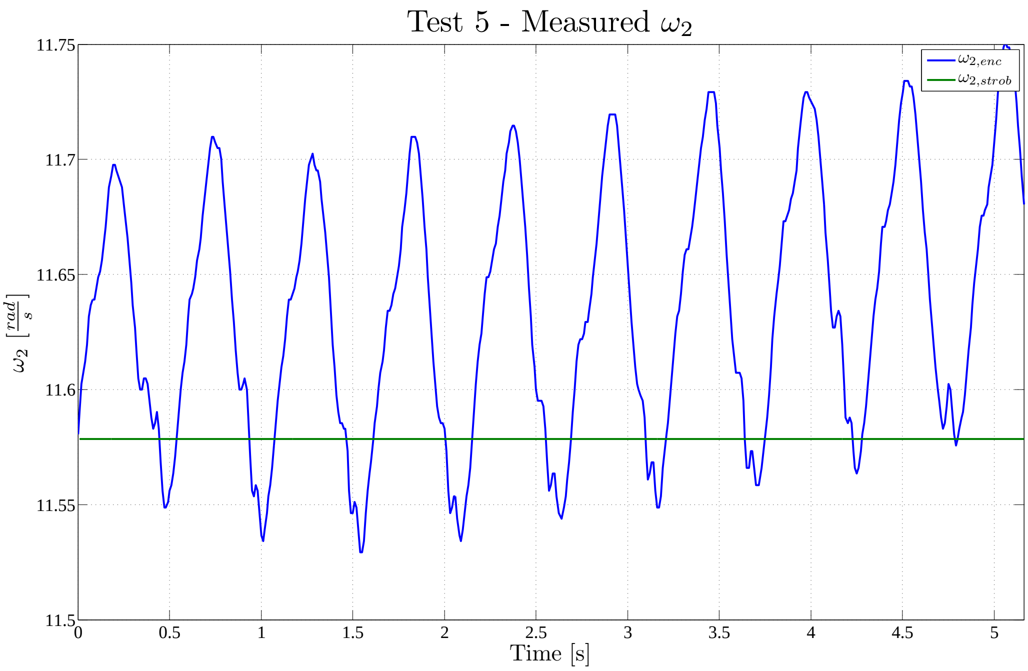

Figure A.10: Test 5: Angular velocity measurements.

Data Processing

The gearing ratio is calculated based on the mean value of the encoder measurements (the stroboscope measurement is a single value for the entire duration of the test). The results are summarized in table A.3.

Test	Mean value of RPM_{PMSM} $[RPM]$	RPM_{strob} $[RPM]$	n $[\cdot]$
1	6127.7	590.5	10.38
2	2623.8	252.5	10.39
3	1609.7	155.4	10.36
4	3094.8	299.3	10.34

Table A.3: Mean value of RPM_{PMSM}, stroboscope measurement of RPM_{strob} and calculated gearing ratio for test 1-4.

The mean value of the calculated gearing ratios is $n = 10.3675$ which will be used throughout the report. The standard deviation of n is $\sigma_n = 0.0222$.

The RSW encoder is validated by comparing the mean value of the angular velocity measurements obtained from the encoder $\omega_{2,enc}$ to the angular velocity measurement obtained from the stroboscope light $\omega_{2,strob}$. The percentage-wise deviation between the two measurements is calculated and used to validate the results.
The maximum percentage-wise deviation of the encoder signal compared to its mean value is used to determine the quality of the measurement. The results are summarized in table A.4.

Test	Mean value of $\omega_{2,enc}$ $[\frac{rad}{s}]$	Maximum deviation of $\omega_{2,enc}$ $[\%]$	$\omega_{2,strob}$ $[\frac{rad}{s}]$	Deviation $[\%]$
5	11.6361	0.9895	11.5785	0.4972
6	43.5756	0.6382	43.5983	0.0520

Table A.4: Mean value of $\omega_{2,enc}$, maximum deviation of $\omega_{2,enc}$ from its mean, stroboscope measurement of $\omega_{2,strob}$ and percentage-wise deviation for test 5-6.

Uncertainty in Measurements

The stroboscopic light sensor has a precision of 1 $[RPM]$.

Source of Error

The stroboscope measurements are dependent on the judgment of the person performing the tests - slight variations in angular velocity during the test interval can be difficult to observe when performing the tests. This was seen in Test 1 and 2 where the velocity did increase with 5-10 RPM during the test.

The calculations of gearing ratio as well as the validation of the RSW encoder are affected by the varying velocities as the mean value of the signals are used in the calculations.

Conclusion

The gearing ratio has been determined with acceptable correspondence of the 4 tests. The mean value of the RSW encoder output has been validated and the results are considered acceptable taking the uncertainty of the stroboscope measurements into account. The maximum deviation of the RSW encoder output signal compared to its mean has been measured to be less than 1 %. This small deviation is assumed to be caused by misalignment of the encoder ring as the variations are periodic with a frequency of approximately 1.818 $[Hz]$ for Test 5 (reading from the graph of figure A.10). In comparison the frequency of the RSW in test 5 is $f_{RSW} = {}^{omega_{2,strob}}/_{2\cdot\pi} = 1.843\ [Hz]$. Thus the low frequency oscillations occur with approximately the same time period as one RSW revoulution.
Observation of the position of the encoder ring within the optical switch indicated a slight misalignment during the tests. This misalignment would cause low-frequency oscillations as it was explained in *Theory*.

The variations in the sin-cos encoder signal (seen in the graph of figure A.9) is assumed to be caused by the rough surface of the RSW. The signal oscillates with a frequency of approximately 1.852 $[Hz]$ for Test 3. As the driving wheel rotates with a frequency of $f_1 = {}^{RPM_{strob}}/_{60} = 2.59\ [Hz]$ one revolution of the driving wheel is not periodic with the signal oscillations. The RSW, on the other hand, rotates with a frequency of $f_{RSW} = f_1 \cdot {}^{r_1}/_{r_2} = 1.80\ [Hz]$. Therefore the signal oscillations could be caused by bumps in the RSW tire surface.
The variations in the two encoder signals might seem negligible but the small variations induce severe variations in the slip calculations. This is most distinctly observed at low slip values where the difference between two nearly identical velocities determine the slip value. Thus the main contributions to the calculated slip are the small variations in the encoder signals. The longitudinal slip calculation for Test 3 can be seen in the graph of figure A.11 below.

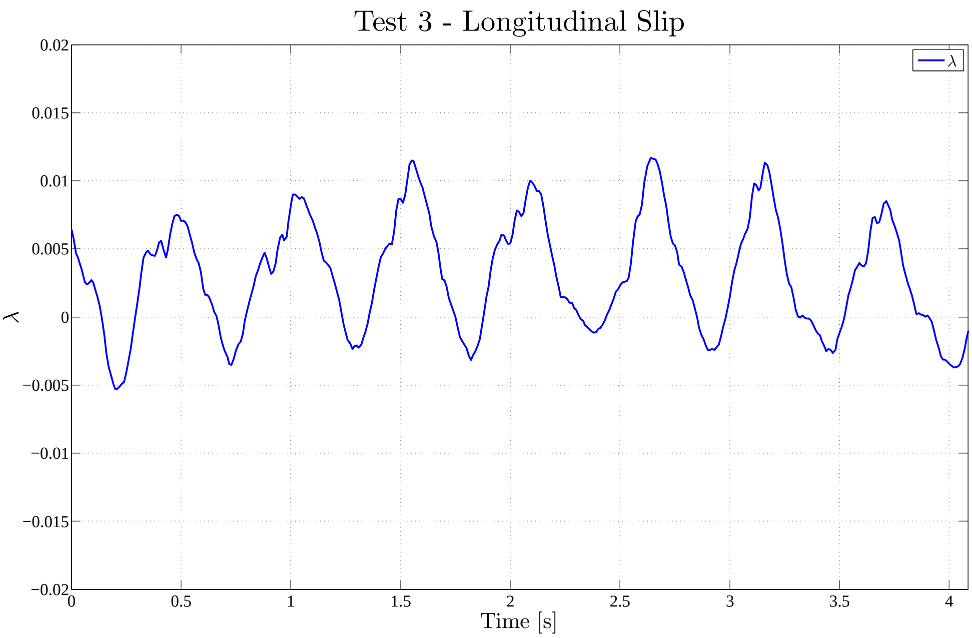

Figure A.11: Test 3: Longitudinal slip vs time.

The slip has a maximum deviation of 0.017 corresponding to a percentage-wise deviation of 1.7 %. In comparison the friction coefficient has peak value at a slip value of 0.06 when the road surface is snow (in the Burckhardt tire model).

The slip controller is tested in a simulation with a noisy slip signal comparable to the measurement seen in figure A.11. The controller is concluded robust to these disturbances - see Section 6.3.3.

A.3 Determination of Wheel Inertia and Viscous Friction Coefficient

Purpose of the Test

The purpose of the test is to determine the total inertia of the QBEAK wheel and the reflected inertia of the PMSM rotor through the gear. The total viscous friction coefficient of the QBEAK wheel and the reflected viscous friction coefficient of the PMSM rotor through the gear is also determined.

Theory

The total inertia, J_1, and viscous friction coefficient, b_1, can be determined from a torque balance around the wheel axle:

$$J_1 \cdot \dot{\omega}_1 = u - b_1 \cdot \omega_1 \tag{A.7}$$

where ω_1 is the angular velocity of the driving wheel and u is the torque developed at the wheel axle by the PMSM (through the gear).

If the input u is chosen as a step input of magnitude u^* the time response of ω_1 can be used to determine J_1 and b_1. The time response is found by rewriting equation (A.7) as:

$$\dot{\omega}_1 + \frac{1}{\tau_1} \cdot \omega_1 = \frac{K_{dc}}{\tau_1} \cdot u \tag{A.8}$$

with $\tau_1 = \frac{J_1}{b_1}$, $K_{dc} = \frac{1}{b_1}$ and for a step input at $t = 0$, $u(t) = \begin{cases} 0 & \text{for } t < 0 \\ u^* & \text{for } t \geq 0 \end{cases}$

The time response for $t \geq 0$ then given as [31, p.116-119]:

$$\omega_1(t) = \omega_1(0) \cdot e^{-t/\tau_1} + K_{dc} \cdot u^* \cdot \left(1 - e^{-t/\tau_1}\right) \tag{A.9}$$

The first term in the right side of the time response equation is the initial condition response, the second term is the steady state response and the third term is the natural response.
By stepping the torque at $\omega_1(0) = 0$ the initial condition response is equal to zero and the response reduces to:

$$\omega_1(t) = c_1 \cdot \left(1 - e^{-c_2 \cdot t}\right) \tag{A.10}$$

where $c_1 = K_{dc} \cdot u^*$ and $c_2 = 1/\tau_1$ can be determined from a curve fit, i.e. the viscous friction coefficient and inertia can be found as:

$$b_1 = \frac{u^*}{c_1} \tag{A.11}$$

$$J_1 = \frac{b_1}{c_2} \tag{A.12}$$

Apparatus used in the test

The components used in the test are listed in table A.5.

Apparatus	**Description**	**Comments**
IBM Lenovo T61	Laptop	The program LabVIEW is used during test
ATE FS106/100/6	3-phase, PMSM-motor	The peak torque is 19.1 $[Nm]$ and the rated speed is 13000 $[rpm]$
Sevcon Gen4	Motor controller (incl. inverter)	Communicates via CAN-bus
Battery pack	6 car batteries	The batteries are series connected. Each battery has a terminal voltage of 15 [V]
NI-USB 8473 Interface	High speed USB to CAN interface	The maximum transfer rate is 1000 $[{}^{kbit}/_{s}]$
NI USB-6210	Data Acquisition Box	The resolution is 16 $[bit]$, the maximum sample rate is 250 $[{}^{kS}/_{s}]$ for both input and output terminals
Motor-wheel gear	Belt-gear	The gearing ratio is $n = 10.3675$
Pulley	Manual pulley	Used to lift the QBEAK wheel from the RSW

Table A.5: Apparatus used to determine wheel inertia and viscous friction coefficient.

Datasheets of the components listed in the table above can be found on the attached CD (see appendix C).

Test Method

The test setup described in Appendix A.1 is modified by removing the RSW and supporting the driving wheel and suspension by a pulley (see figure A.12). As the tire friction force between the two wheels is removed, the equations described in the *Theory* section are valid. The wheel is accelerated to a constant angular velocity by applying a step input torque and the time response of ω_1 is logged. The measured torque is logged as well to ensure, that a constant torque is applied.

Figure A.12: Picture of the test setup with the driving wheel raised to remove the friction between the two tires.

Data Recording

3 tests are carried out to determine the inertia. The torque reference is the same for all the tests as steady-state values of ω_1 was not obtained for other input torques. The motor torque in test 1 is plotted along with the corresponding velocity response in figure A.13 (test 2 and 3 shows similar torque response).

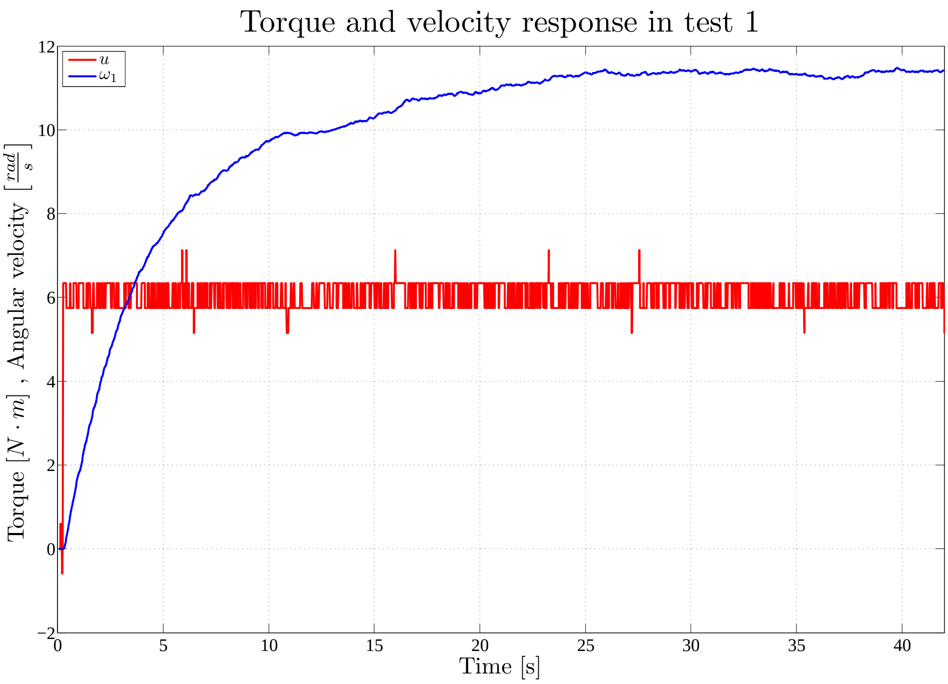

Figure A.13: Torque and angular velocity measurements for test 1.

The angular velocity responses of the 3 tests are seen in figure A.14. An average waveform is also plotted, it is found by calculating the mean of the 3 responses at each sampling instant.

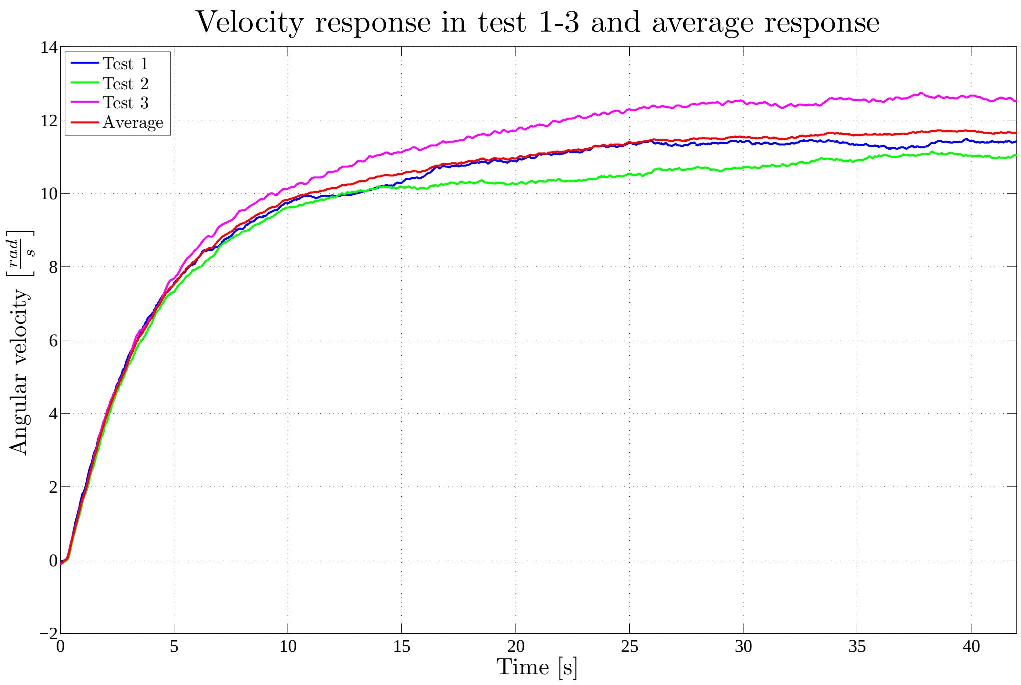

Figure A.14: Angular velocity measurements for test 1-3 and average velocity waveform.

Data Processing

The input torque is averaged over the duration of the step input to find u^* in each test. The results are summarized in table A.6.

Test	u^* $[N \cdot m]$
1	6.0318
2	5.9783
3	5.9204
Mean	5.9768

Table A.6: Calculated u^* for test 1-3 and mean value of the results.

A curve fit is made of the average response (seen in figure A.14) using the model given by equation (A.10). The resulting fitted curve and the average response is seen in figure A.15.

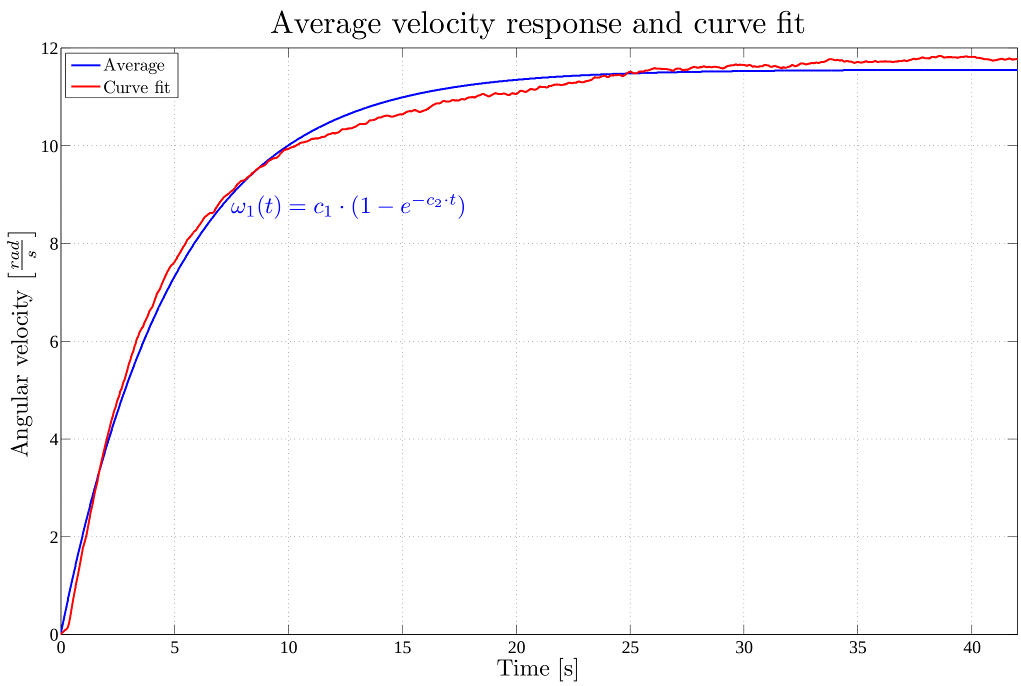

Figure A.15: Average velocity waveform and curve fit.

The result of the curve fitting is summarized in table A.7. The goodness of the curve fit is given in terms of the coefficient of determination $R^2 = 0.9923$.

Parameter	Value	Confidence bounds (using a 95 % confidence interval)
c_1	11.55	[11.54 11.56]
c_2	0.201	[0.2002 0.2018]
b_1	0.5175	[0.5170 0.5179]
J_1	2.5745	[2.5621 2.5870]

Table A.7: Curve fitting results and corresponding values of b_1 and J_1.

The calculations of b_1 and J_1 are based on equation (A.11) and (A.12) using $u^* = 5.9768$ (the mean of the 3 tests).

Source of Error

The angular velocity responses seen in figure A.14 indicate that the friction behavior is not purely viscous as assumed. This deviation from the model reduces the accuracy of the curve fit.
The responses deviate most in their steady state values. In steady state the angular velocity response is given as $\omega_{1,ss} = {}^{u^*}/_{b_1}$. Since the friction coefficient is small, deviations in u^* has a big impact on the steady state value.

Conclusion

The test was concluded successful. The inertia and friction coefficient of the driving wheel are determined with acceptable correspondence in the tests. $J_1 = 2.5745$ $[N \cdot m]$ and $b_1 = 0.5175$ $[{}^{N \cdot m \cdot s}/_{rad}]$.

A.4 Test of Friction Force Observer

Purpose of the Test

The purpose of the test is to investigate the performance of the friction force observer designed in Section 5.4.

Theory

The friction force observer estimates the angular velocity of the QBEAK wheel and calculates the error between the estimated angular velocity and the measured angular velocity from a sin/cos-encoder. The friction force is then estimated based on this error. The magnitude of the velocity estimation error is an indication of the quality of the friction force estimate.

The angular velocity estimation error and its derivative are given as:

$$e_\omega = \omega_1 - \hat{\omega}_1 \tag{A.13}$$

$$\dot{e}_\omega = \dot{\omega}_1 - \dot{\hat{\omega}}_1 = -\frac{r_1}{J_1} \cdot (L(\omega_1, \hat{\omega}_1) + F_x) \tag{A.14}$$

When the error dynamics approach zero the average of the friction force observer signal $L(\omega_1, \hat{\omega}_1)$ approaches the friction force acting between the two tires. The term $L(\omega_1, \hat{\omega}_1)$ is chosen as:

$$L(\omega_1, \hat{\omega}_1) = -M \cdot \text{sign}(e_\omega)$$

where M is a positive constant which must be larger than the magnitude of the friction force.

The average of $L(\omega_1, \hat{\omega}_1)$ can be found by filtering the high frequency components caused by the discontinuity of the observer or by adding a boundary layer around $e_{\omega_1} = 0$ - see Section 5.4. A 4th order low-pass Butterworth filter is proposed in the tests in combination with a boundary layer.

Apparatus used in the test

The components used in the test are listed in table A.8.

Apparatus	Description	Comments
IBM Lenovo T61	Laptop	The program LabVIEW is used during test
ATE FS106/100/6	3-phase, PMSM-motor	The peak torque is 19.1 $[Nm]$ and the rated speed is 13000 $[rpm]$.
Sevcon Gen4	Motor controller (incl. inverter)	Communicates via CAN-bus
Battery pack	6 car batteries	The batteries are series connected. Each battery has a terminal voltage of 15 [V]
NI USB-8473 Interface	High speed USB to CAN interface	The maximum transfer rate is 1000 $[kbit/s]$
NI USB-6210	Data Acquisition Box	The resolution is 16 $[bit]$, the maximum sample rate is 250 $[kS/s]$ for both input and output terminals
Motor-wheel gear	Belt-gear	The gearing ratio is $n = 10.3675$
Road Simulation Wheel	Large wheel used to simulate the road surface and vehicle inertia	Consist of a rubber tire with a rough tread pattern, an iron rim and a circular iron plate attached to the back of the wheel (see figure A.4)
Silicone Spray	Oil based lubrication	

Table A.8: Apparatus used to determine the friction force.

Datasheets of the components listed in the table above can be found on the attached CD (see appendix C).

Test Method

The test setup described in Appendix A.1 is used. The friction force is estimated using measurements of angular wheel velocity and torque input (both obtained using CAN communication with the Gen4 motor controller). The reference torque $T_{m,ref}$ is varied in steps and the dynamic response of the observer is tested by plotting the velocity estimation error, e_ω. As $\dot{e}_\omega$ approaches zero, the estimated friction forces approaches the true value of the friction force. The response of e_ω is therefore used to investigate the dynamic performance of the observer.

Six tests are carried out. In the first two tests the impact of changing the boundary layer width θ_o is investigated. The two tests are made by supplying similar torque references in the beginning of the tests. In the last part of test 2 the torque reference is increased in order to find out if the initial observer gain $M_o = 200$ is sufficiently high as the maximum available friction force is unknown.
After test 2 the observer gain is M_o is increased to 1000. This value is well beyond the theoretical limit of F_x based on the limits of the input torque and the assumption that the viscous friction torque and the inertial torque are negligible compared to the torque caused by F_x. In this case the maximum achievable friction force $F_{x,max}$

is equal to:

$$F_{x,max} = \frac{T_{m,max} \cdot n}{r_1} = 695\ [N]$$

where $T_{m,max} = 19.1\ [N \cdot m]$ is the maximum torque supplied by the PMSM.

Test 3 uses $M_o = 1000$ and $\theta_2 = 2$. The boundary layer is increased to account for the increased observer gain.

A silicone spray is applied at the surface of the RSW to alter the friction characteristics of the surface and a test similar to test 3 is made (test 4).

The tests are summarized in table A.9 below.

Test	**Description**	**Observer Parameters**	**Plotted Data**
1	Dry RSW, $T_{m,ref}$ step-sequence $[N \cdot m]$: $\{0\ ,\ 19.1\ ,\ 0\ ,\ 38.2\ ,\ 0\ \}$	$M_o = 200$, $\theta_o = 2$, $f_c = 30\ [Hz]$	T_m, ω_1, $\hat{\omega}_1$, $\hat{F}_x$, e_ω
2	Dry RSW, $T_{m,ref}$ step-sequence $[N \cdot m]$: $\{0\ ,\ 19.1\ ,\ 0\ ,\ 38.2\ ,\ 0\ ,\ 57.1\ ,\ 0\ ,\ 76.4\ ,\ 0\}$	$M_o = 200$, $\theta_o = 0.2$, $f_c = 30\ [Hz]$	T_m, $\hat{F}_x$, e_ω
3	Dry RSW, $T_{m,ref}$ step-sequence $[N \cdot m]$: $\{0\ ,\ 19.1\ ,\ 0\ ,\ 38.2\ ,\ 0\ \}$	$M_o = 1000$, $\theta_o = 2$, $f_c = 30\ [Hz]$	e_ω
4	Lubricated RSW, $T_{m,ref}$ step-sequence $[N \cdot m]$: $\{0\ ,\ 19.1\ ,\ 0\ ,\ 38.2\ ,\ 0\ \}$	$M_o = 1000$, $\theta_o = 2$, $f_c = 30\ [Hz]$	T_m, $\hat{F}_x$, e_ω

Table A.9: Different tests of the sliding mode friction force observer.

where f_c is the cut-off frequency of the low-pass filter applied to $\hat{F}_x$.

Data Recording

Test 1 Figure A.16 shows a plot of the measured torque T_m, angular velocity ω_1 and the estimated angular velocity $\hat{\omega}_1$ in test 1. Similar responses has been observed for similar torque inputs in the remaining tests with varying estimation errors. Only plots of interest are presented for the following tests.

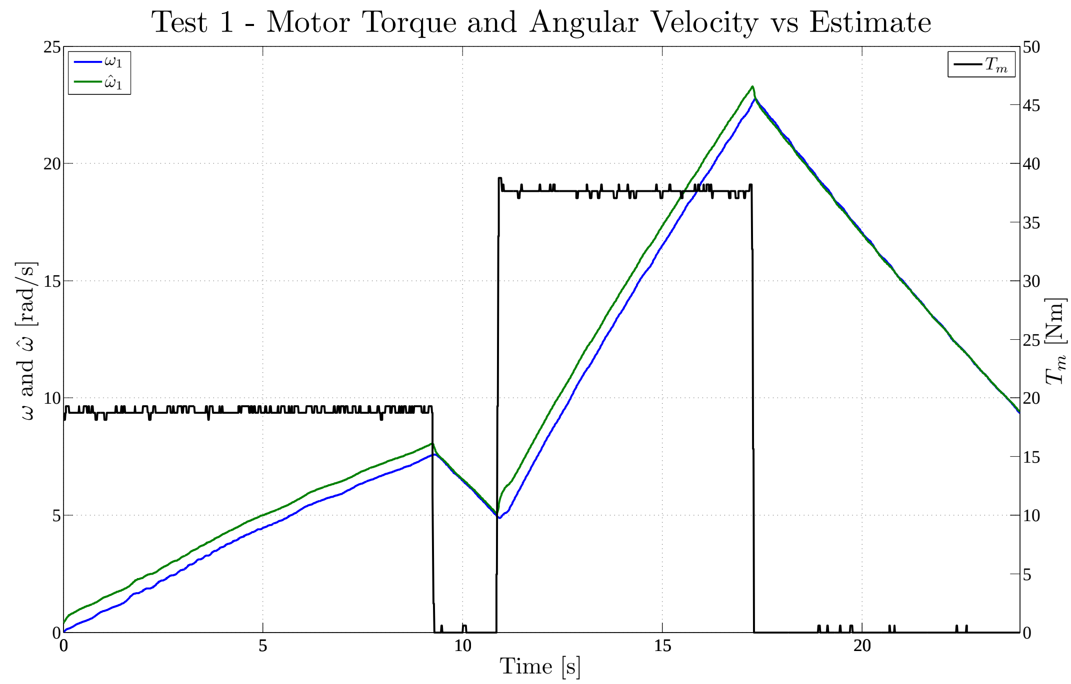

Figure A.16: Torque, angular velocity and estimated angular velocity in test 1.

Figure A.17 shows a plot of the corresponding estimated friction force $\hat{F}_x$ and the measured torque T_m in test 1.

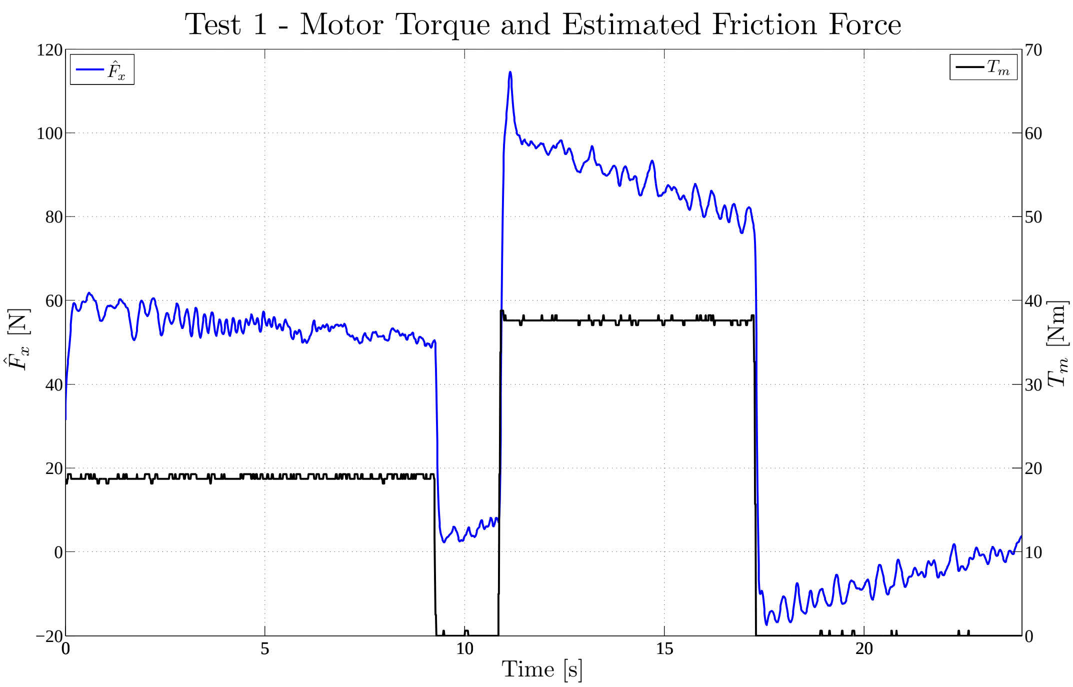

Figure A.17: Torque and estimated friction force in test 1.

The error of the velocity estimate in test 1 is plotted in figure A.18.

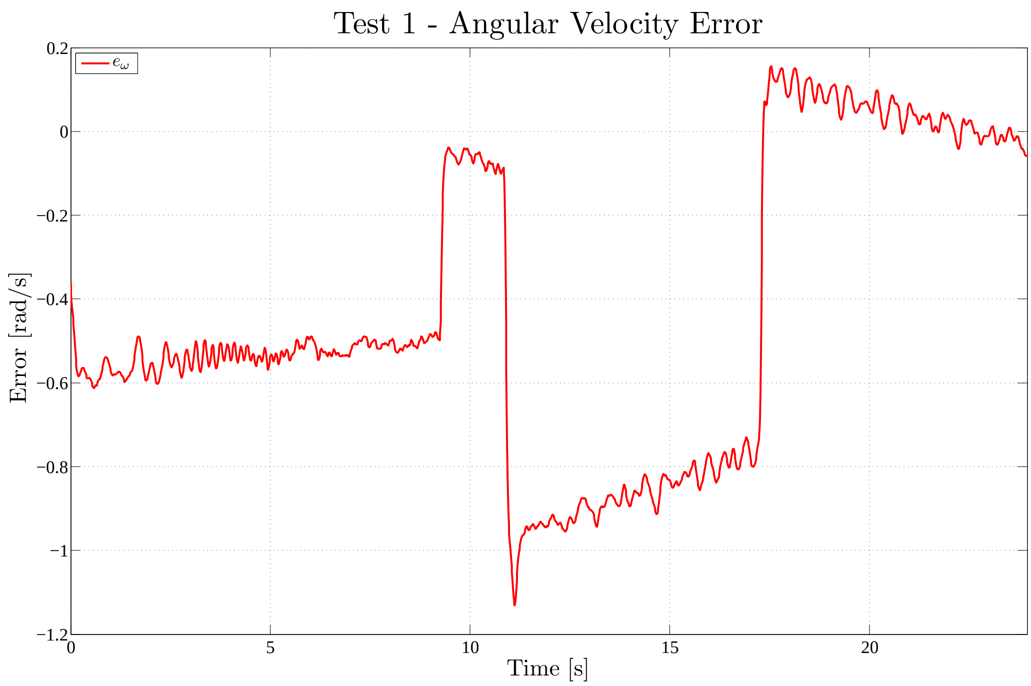

Figure A.18: Error between angular velocity and its estimate in test 1.

Test 2 Figure A.19 shows the estimated friction force $\hat{F}_x$ and the measured torque T_m in test 2.

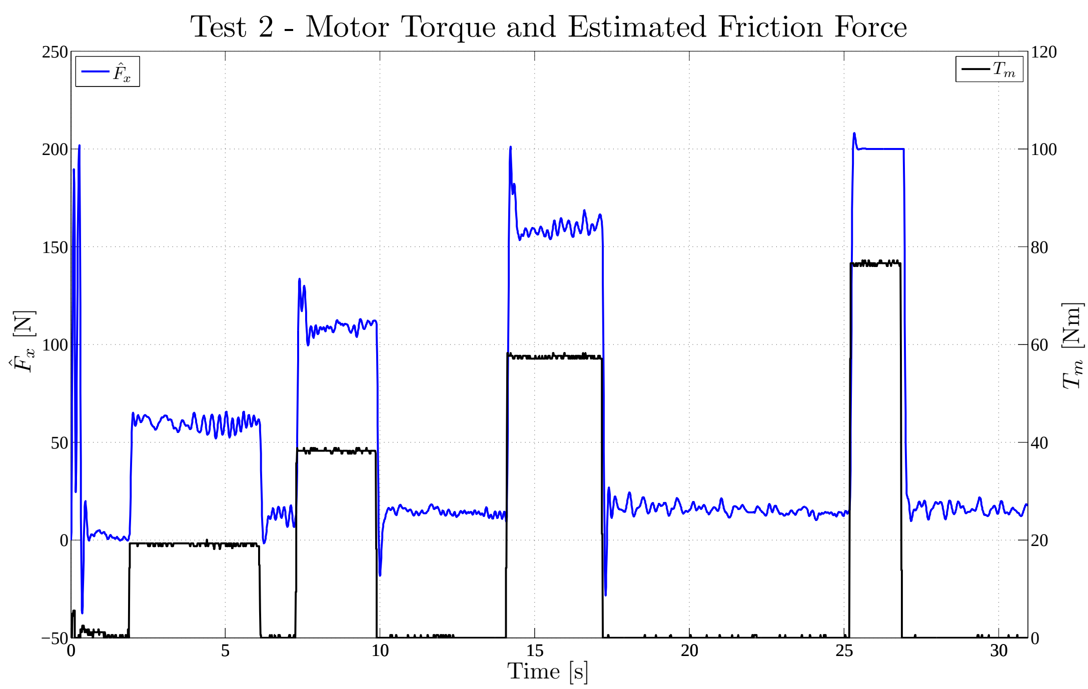

Figure A.19: Torque and estimated friction force in test 2.

The error of the velocity estimate in test 2 is plotted in figure A.20.

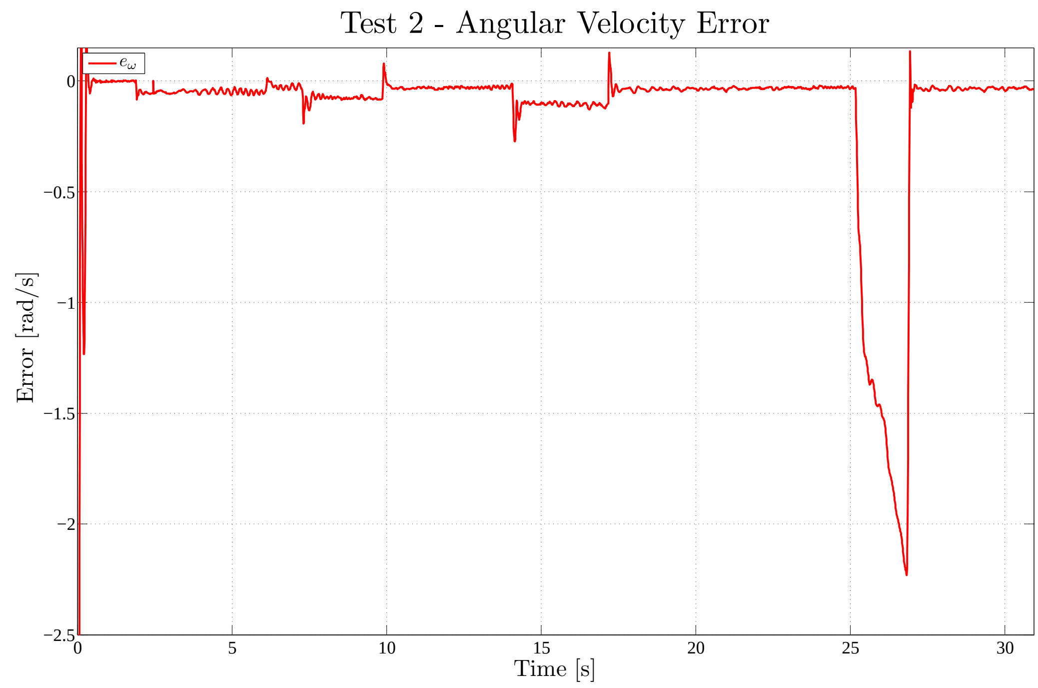

Figure A.20: Error between angular velocity and its estimate in test 2.

Test 3 The error of the velocity estimate in test 3 is plotted in figure A.21.

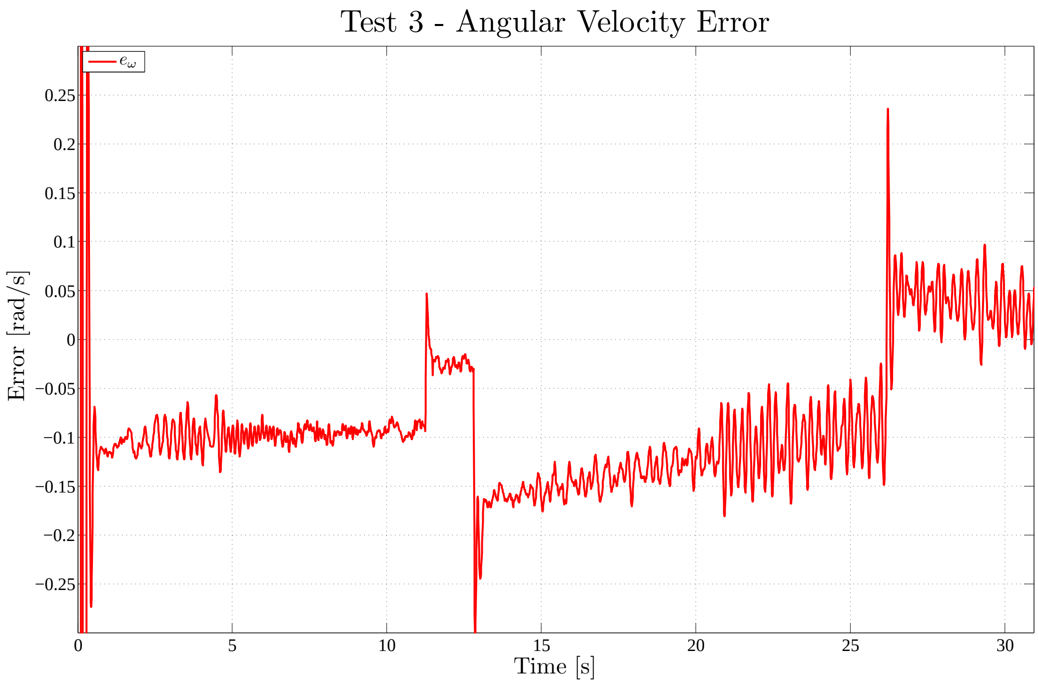

Figure A.21: Error between angular velocity and its estimate in test 3.

Test 4 Figure A.22 shows the estimated friction force $\hat{F}_x$ and the measured torque T_m in test 4.

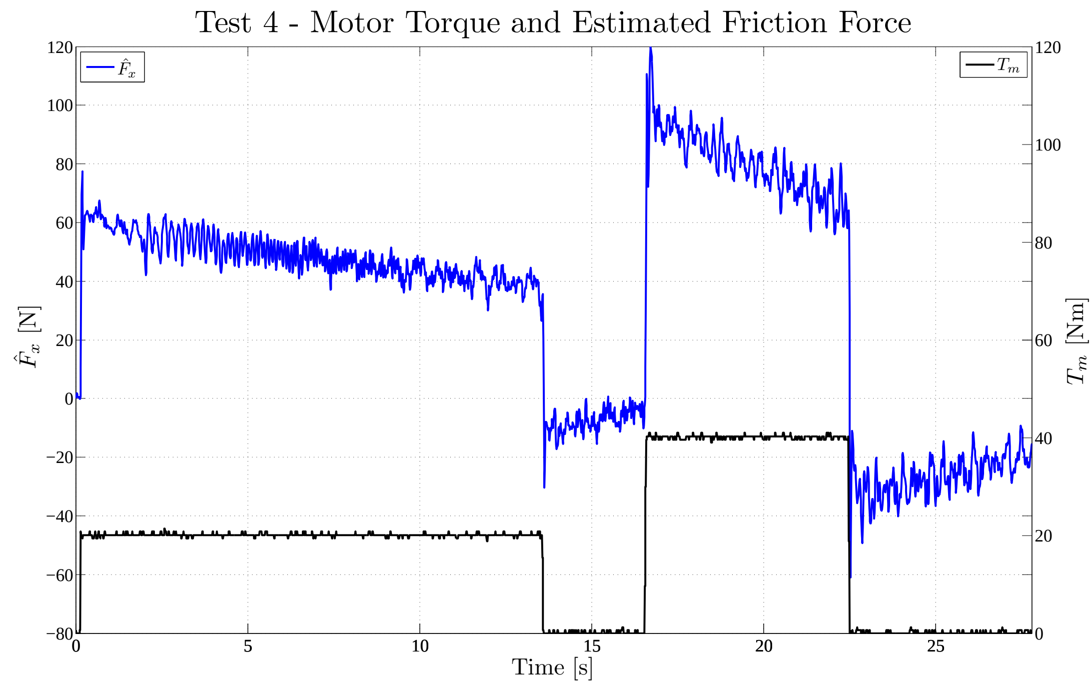

Figure A.22: Torque and estimated friction force in test 4.

The error of the velocity estimate in test 4 is plotted in figure A.23.

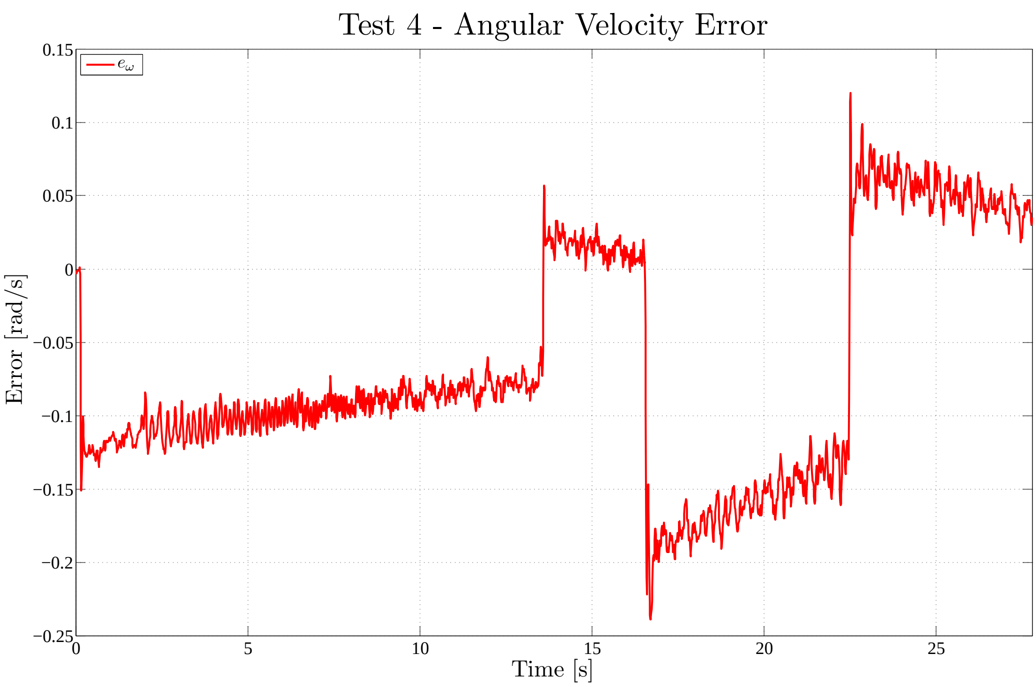

Figure A.23: Error between angular velocity and its estimate in test 4.

Data Processing

Test 1-3 show errors in the velocity estimate as the tests are initialized. This indicates that the integrator within the observer has not been initialized with the right initial condition. The initial condition should equal $\omega_1(0)$ in order to have an initial estimation error of zero. This has been fixed after test 3.

As the torque reference input sequence $T_{m,ref}$ ={0 , 19.1 , 0 , 38.2 , 0} $[N \cdot m]$ is used in test 1-4 the observer performance will be evaluated by comparing the peak velocity estimation error at each step. The initial peak due to wrong initial conditions will be left out of the analysis. The results are summarized in table A.10

Step in $T_{m,ref}$ $[N \cdot m]$	**Peak of e_ω $\frac{rad}{s}$**			
	Test 1	**Test 2**	**Test 3**	**Test 4**
$0 \rightarrow 19.1$	Initialization error	0.085	Initialization error	0.15
$19.1 \rightarrow 0$	0.04	0.012	0.047	0.057
$0 \rightarrow 38.2$	1.13	0.19	0.31	0.24
$38.2 \rightarrow 0$	0.16	0.078	0.24	0.12

Table A.10: Peak velocity estimation errors.

Uncertainty in Measurements

The uncertainties in measurement of the angular velocity of the QBEAK wheel described in Appendix A.2 does also apply to this test.

Source of Error

The angular velocity input to the observer is low-pass filtered using a 4th order Butterworth filter with a cut-off frequency of 5 $[Hz]$ (see Appendix A.2). The phase shift caused by the filtering is assumed to affect the dynamic performance of the friction force estimation as step input torques are applied.

Conclusion

It is seen from the velocity estimation errors (figure A.18, A.20, A.21 and A.23) that the observer is stable except in test 2 (in the interval $t = [25.16;26.82]$ $[s]$). The instability is due to the fact that the friction force increases beyond the observer gain $M_o = 200$ as a torque input of 76.4 $[N\dot{m}]$ is applied. According to Section 5.4 this results in instability of the observer. As a result the estimated friction force saturates at $\hat{F}_x = M_o$ and the estimated angular velocity becomes lower than the actual velocity. As the friction force affects the acceleration of the wheel, the velocity estimation error continues to grow in magnitude. Instability of the observer has not been observed during tests after the observer gain is increased to $M_o = 1000$.
Table A.10 indicates that the tracking accuracy of the velocity estimation is best in test 2 which is to be expected as the width of the boundary layer is decreased. However, as the observer gain is increased (test 3 and 4) a higher boundary layer has been necessary to decrease chattering of the friction force estimate signal.
By close inspection of the estimated friction forces it has been observed that the initial oscillations of the estimates that occur after each step input settle after approximately 0.25 to 0.45 $[s]$. This settling time is partly due to the dynamics of the observer itself but also the low-pass filtering of the velocity input signal. As an

example consider figure A.24 showing a step in T_m from 57.1 to 0 $[N \cdot m]$ and the corresponding estimated friction coefficient $\hat{F}_x$ in test 2.

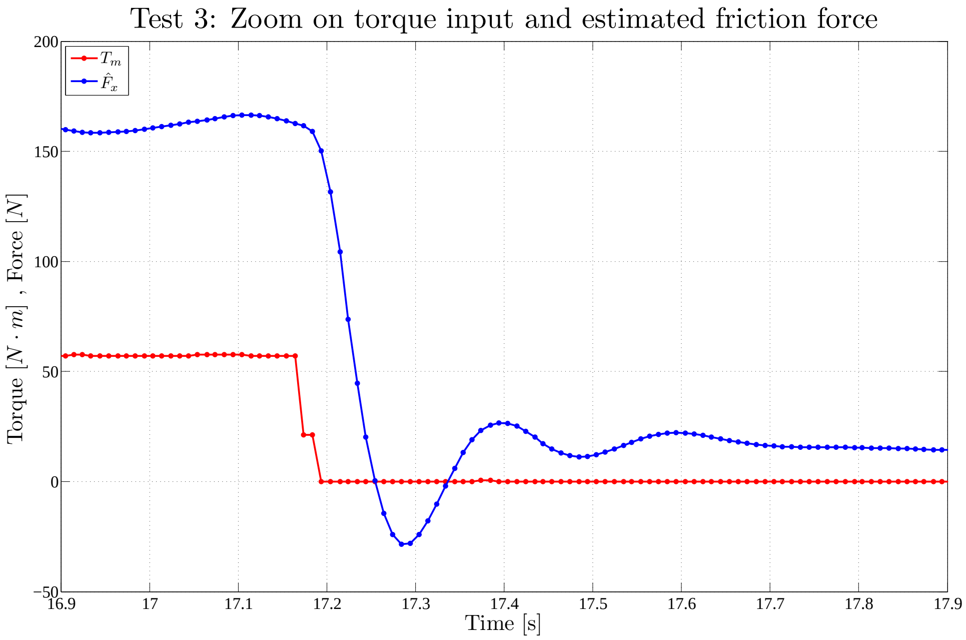

Figure A.24: Test 2: Zoom on T_m and $\hat{F}_x$ near step in input torque.

Figure A.25: Step response of 4th order continuous Butterworth filter with a cut-off frequency of 5 $[Hz]$.

Figure A.24 illustrates that the oscillations settle after approximately 0.45 $[s]$. This is comparable to the settling of the oscillations caused by a step input to the 4th order Butterworth low-pass filter applied to ω_1. Figure A.25

shows a step input of a continuous Butterworth filter with the same characteristics as the one used in the tests.

It is noted from figure A.17 and A.22 that the estimated friction forces are comparable even though the surface friction has been altered by the application of silicone spray. This can be explained by the fact that a constant torque results in different slip values but not different friction forces - refer to Section 5.1.1.1. Thus the system is able to achieve higher slip values with the same motor torque - this is the purpose of adding the silicone spray. The performance of the observer is comparable for both surfaces.

It is concluded that the observer is ready for implementation in a slip-control system.

A.5 Test of Slip Controller

Purpose of the Test

The purpose of the test is to investigate the performance of the sliding mode slip controller developed in Section 5.2.

Theory

The test setup is designed to represent a driving condition. However, the test system is only an approximation of the system for which the sliding mode controller is designed. The equations of motion describing the test system are given in Appendix A.1. Comparing these equations to the simplified longitudinal model of the vehicle (equation (5.2)) shows that the slip dynamics of the test system can be described as:

$$\dot{\lambda}_L = -\frac{F_x}{\dot{x}} \cdot \left(\frac{1-\lambda_L}{m_v} + \frac{r_1^2 \cdot (1-\lambda_L)^2}{J_1} \right) + \frac{r_1 \cdot (1-\lambda_L)^2}{J_1 \cdot \dot{x}} \cdot u \qquad \text{Driving condition}$$

$$\dot{\lambda}_L = -\frac{F_x}{\dot{x}} \left(\frac{1+\lambda_L}{m_v} + \frac{r_1^2}{J_1} \right) + \frac{r_1}{J_1 \cdot \dot{x}} \cdot u \qquad \text{Braking condition}$$

In both models $m_v = {}^{J_2}/_{r_2^2}$ and $\dot{x} = r_2 \cdot \omega_2$. With these substitutions the dynamics are equal to those used in the design of the slip controller, thus the same control topology can be used. However, the uncertainties and disturbances in the test system are different from those treated in Section 5.2. The terms $\hat{f}$, F, $\hat{g}$ and β are therefore slightly different - they are listed in table A.11.

	Driving condition (TCS)	**Braking condition (ABS)**
$\hat{f}$	$-\frac{F_x}{\dot{x}} \cdot \left(\frac{1-\lambda_L}{\hat{m}_v} + \frac{r_1^2 \cdot (1-\lambda_L)^2}{\hat{J}_1} \right)$	$-\frac{F_x}{\dot{x}} \cdot \left(\frac{1+\lambda_L}{\hat{m}_v} + \frac{r_1^2}{\hat{J}_1} \right)$
F	$\frac{\lvert F_x\rvert \cdot \lvert 1-\lambda_L\rvert}{\dot{x}} \cdot \left(\frac{\bar{m}_v}{m_{v,min} \cdot \hat{m}_v} + \frac{\bar{J}_1}{J_{1,min} \cdot \hat{J}_1} \cdot r_1^2 \cdot \lvert 1-\lambda_L\rvert \right)$	$\frac{\lvert \hat{F}_x\rvert}{\dot{x}} \cdot \left(\frac{\bar{m}_v}{m_{v,min} \cdot \hat{m}_v} \cdot \lvert 1+\lambda_L\rvert + \frac{\bar{J}_1}{J_{1,min} \cdot \hat{J}_1} \cdot r_1^2 \right)$
$\hat{g}$	$\frac{1}{\sqrt{J_{1,max} \cdot J_{1,min}}} \cdot \frac{r_1 \cdot (1-\lambda_L)^2}{\dot{x}}$	$\frac{1}{\sqrt{J_{1,max} \cdot J_{1,min}}} \cdot \frac{r_1}{\dot{x}}$
β	$\sqrt{\frac{J_{1,max}}{J_{1,min}}}$	$\sqrt{\frac{J_{1,max}}{J_{1,min}}}$

Table A.11: Controller terms used in the test setup

The inertia of the driving wheel is found experimentally (see Appendix A.3) and the radii r_1 and r_2 are measured. The normal force, F_z, is assumed constant as dynamic load transfer does not apply to the one-wheel test setup considered. The only uncertainty lies in the inertia of the RSW, J_2, and thus in m_v. Furthermore, a small uncertainty bound is applied to J_1 as well.

Apparatus used in the test

The components used in the test are listed in table A.12.

Apparatus	**Description**	**Comments**
IBM Lenovo T61	Laptop	The program LabVIEW is used during test
ATE FS106/100/6	3-phase, PMSM-motor	The peak torque is 19.1 $[Nm]$ and the rated speed is 13000 $[rpm]$.
Sevcon Gen4	Motor controller (incl. inverter)	Communicates via CAN-bus
Battery pack	6 car batteries	The batteries are series connected. Each battery has a terminal voltage of 15 $[V]$
UVW-Encoder	Absolute encoder (Sin-Cos)	Located in the PMSM
NI USB-8473 Interface	High speed USB to CAN interface	The maximum transfer rate is 1000 $[^{kbit}/_{s}]$
NI USB-6210	Data Acquisition (DAQ) Box	The resolution is 16 $[bit]$, the maximum sample rate is 250 $[^{kS}/_{s}]$ for both input and output terminals
Motor-wheel gear	Belt-gear	The gearing ratio is $n = 10.3675$
Road Simulation Wheel (RSW)	Large wheel used to simulate the road surface and vehicle inertia	Consist of a rubber tire with a rough tread pattern, an iron rim and a circular iron plate attached to the back of the wheel (see figure A.4)
Optical Switch (OPB917)	Photologic circuit actuated by an Infrared LED	Rise/fall time of pulse signal $t_{r/f} = 50$ $[ns]$, propagation delay $t_{prop} = 3$ $[\mu s]$
Silicone Spray	Oil based lubrication	
Textronix DPO 2014	Phosphor Oscilloscope	Maximum sample rate 1 $[^{GS}/_{s}]$
APPA 32	Current clamp	Bandwidth 400 $[Hz]$, resolution 10 $[^{mV}/_{A}]$

Table A.12: Apparatus used to test the controller performance.

Datasheets of the components listed in the table above can be found on the attached CD (see appendix C).

Test Method

TCS

The test setup described in Appendix A.1 is used to simulate situations of vehicle acceleration, with m_v representing the equivalent mass of the vehicle.
The slip controller is tested in the following manner. The controller is turned on when the tangential velocity of the RSW is above a predetermined value $\dot{x}_{min}$ and turned off when the velocity is above $\dot{x}_{max}$. The slip controller is tested using different constant longitudinal slip references and tuned in the controller parameters: $\theta_{c,TCS}$ and η. A constant torque of 1 $[N \cdot m]$ is used to accelerate the wheel until it reaches the specified minimum velocity. The first tests are performed without any changes in tire surface of the RSW. Afterwards the controller is tested when the friction between the driving wheel and the RSW is altered. By applying the silicone spray to the RSW tire surface the friction coefficient is lowered. This is done to achieve higher slip values and thereby lower the impact of the periodic measurement noise on the encoder signals (see Appendix A.2).
The controller is implemented using the LabVIEW program described in Appendix B.
During the first tests it is seen that the slip response oscillates significantly and is unstable with both lubricated and non-lubricated RSW. The controller has been tested through simulations prior to the test without showing oscillations of the observed magnitude. The tests are stopped to avoid damaging the test setup and the cause of the oscillations are investigated.
A test comparing the controller output torque reference to the measured torque received via CAN communication is carried out (test 3) to investigate a possible delay in the system.
Afterwards the DAQ box analog output voltage is measured with an oscilloscope, along with the battery output current to the controller (test 4). The battery current is measured using a current clamp and shown on the oscilloscope. These signals are measured to investigate if the delay is caused by the CAN communication, by the motor controller or by both.
The tests are summarized in table A.13 below.

Test	Description	Controller Parameters	Plotted Data	Limits
1	Dry RSW, $\lambda_{ref} = 0.05$	$\eta = 5$, $\theta_{c,TCS} = 0.5$	λ, T_m	$\dot{x}_{min} \approx 10$ $[^{km}/_{h}]$, $\dot{x}_{max} = 80$ $[^{km}/_{h}]$, $T_{m,max} = 130$ $[N \cdot m]$
2	Lubricated RSW, $\lambda_{ref} = 0.1$	$\eta = 5$, $\theta_{c,TCS} = 0.5$	λ, T_m, $T_{m,ref}$	$\dot{x}_{min} \approx 10$ $[^{km}/_{h}]$, $\dot{x}_{max} = 80$ $[^{km}/_{h}]$, $T_{m,max} = 130$ $[N \cdot m]$
3	Lubricated RSW, manual torque	no controller	T_m, $T_{m,ref}$, $T_{m,DAQ}$	$T_{m,max} = 130[N \cdot m]$
4	Oscilloscope measurements, manual torque reference	no controller	V_{DAQ}, i_{bat}	$T_{m,max} = 130[N \cdot m]$

Table A.13: Different tests of the sliding mode TCS slip controller.

ABS

The slip controller used for vehicle braking (ABS) was not tested due to unsatisfactory responses in the TCS tests.

Data Recording

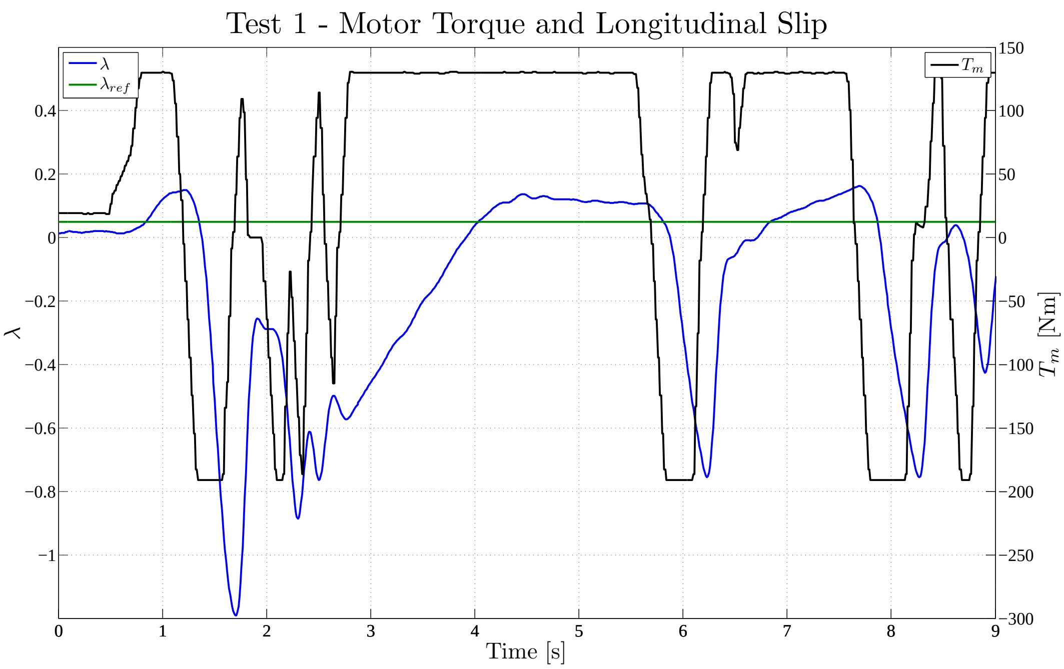

Figure A.26: Motor torque and slip in test 1 (both measurements are obtained via CAN-bus).

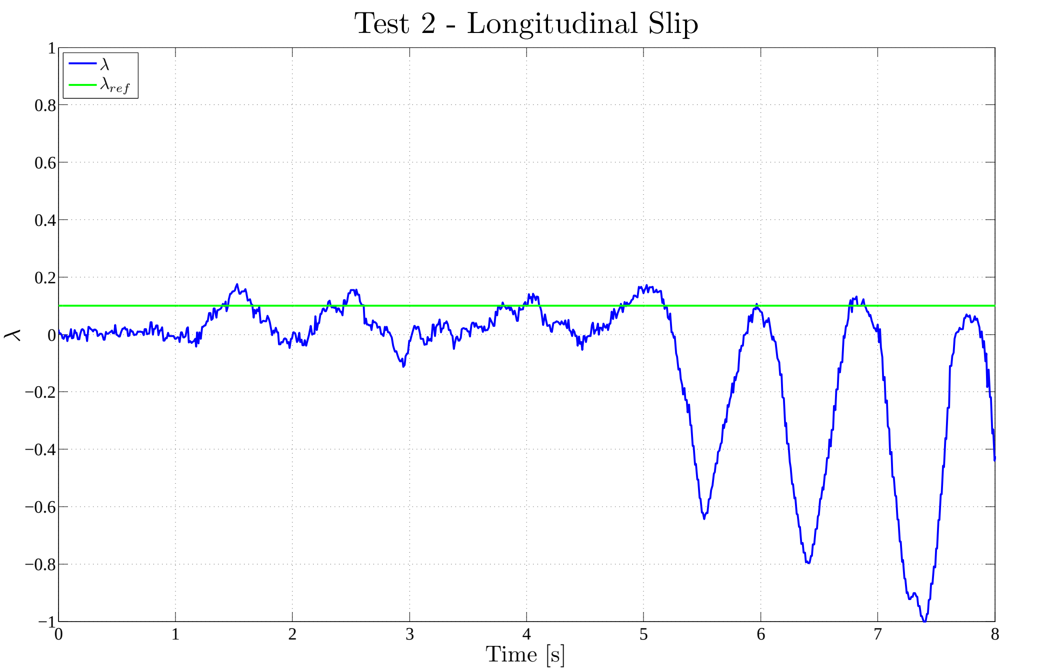

Figure A.27: Longitudinal slip in test 2.

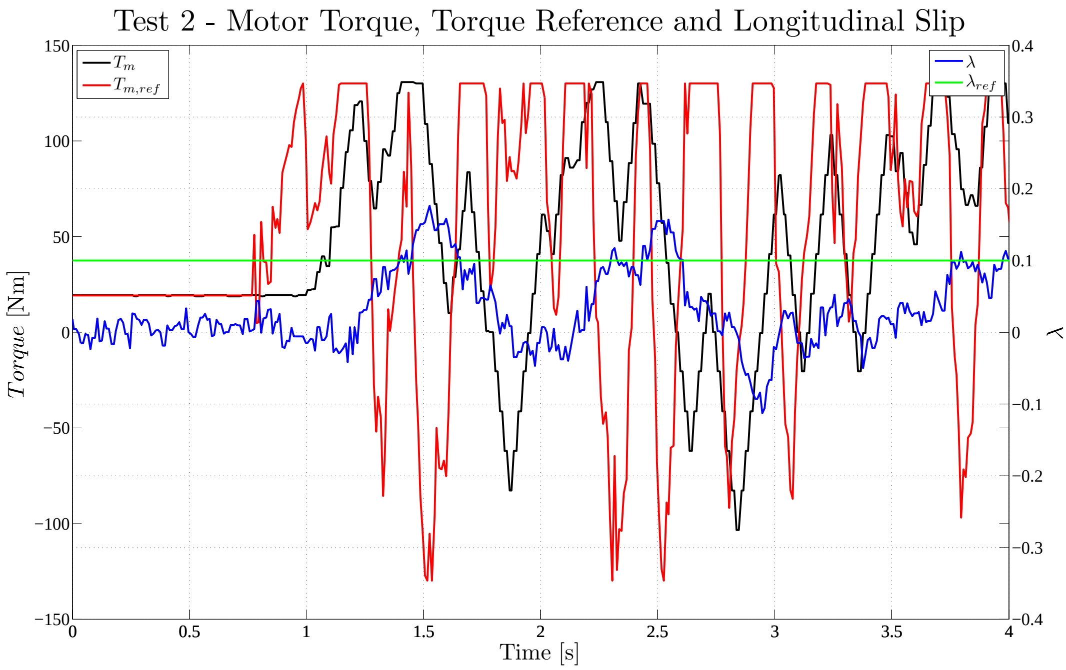

Figure A.28: Motor torque and slip in test 2 (both measurements are obtained via CAN-bus). The red curve is the calculated reference torque. The green line is the chosen slip reference of the slip controller.

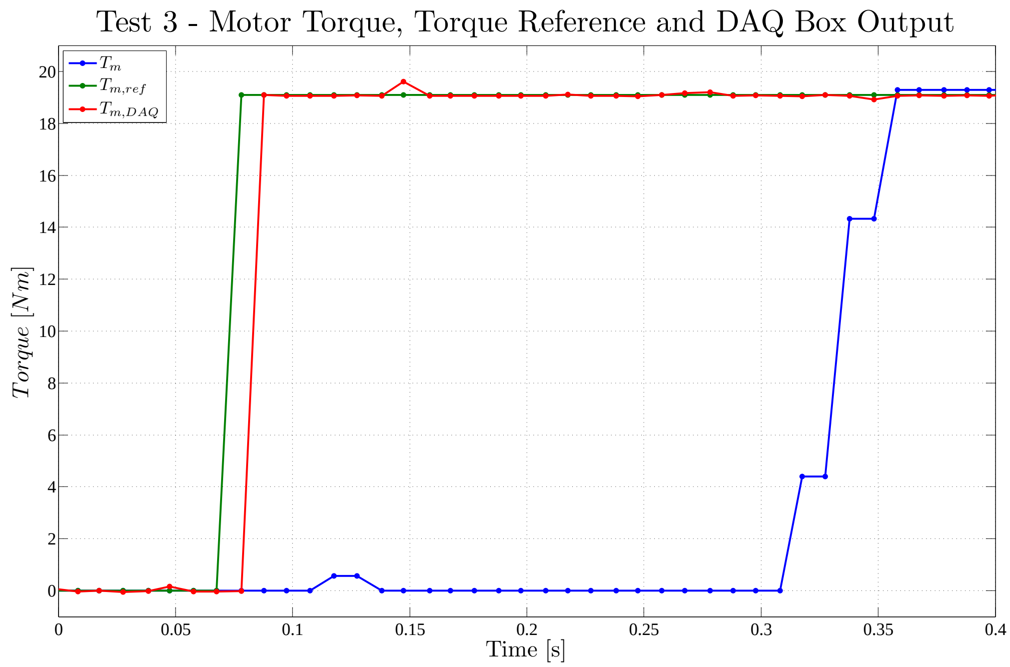

Figure A.29: Measurement of motor torque T_m (obtained via CAN-bus), torque reference $T_{m,ref}$ (demanded by slip controller) and measured torque demand $T_{m,DAQ}$ (calculated from throttle voltage measured by the DAQ box). The dots indicate the sampling instants (sampling time is 10 [ms]). The measurements are from test 3.

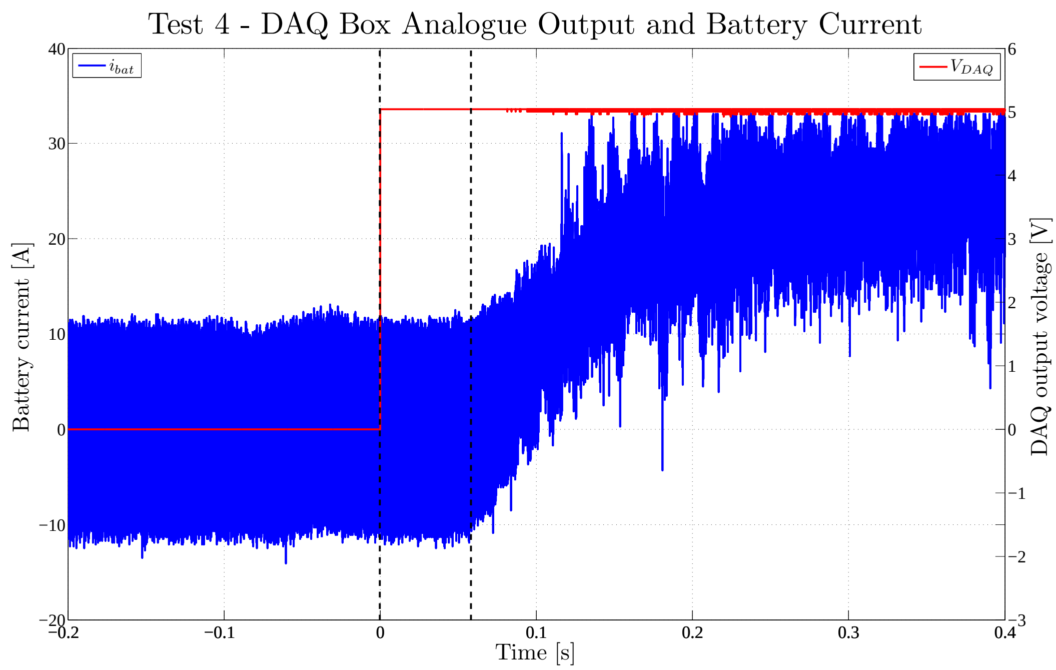

Figure A.30: Oscilloscope measurement of DAQ analog output voltage and battery current in test 4.

Data Processing

As the slip controller showed unsatisfactory response its performance is not evaluated in this section. Instead the system delay will be investigated. The measured delays are listed below.

- The delay between the step in torque reference $T_{m,ref}$ and the measured torque T_m obtained via CAN-bus is approximately 240 [ms] (equal to 24 sampling periods). This is followed by 50 [ms] before the torque has settled at the reference value.
- The delay between the torque reference $T_{m,ref}$ and the measured torque demand $T_{m,DAQ}$ in test 3 is 1 sample (1 [ms]). This is due to the fact that the signal is measured and logged one sample after the output voltage is applied.
- The delay between the applied throttle voltage at the terminals of the Gen4 motor controller and the step in battery current (test 4) is approximately 58 [ms] followed by approximately 100 [ms] before the current response has settled.

Uncertainty in Measurements

The measurement performed with the oscilloscope (seen in figure A.30) shows noise in the measurement of battery current. The noise of ± 1 $[V]$ corresponds to ± 10 $[A]$ when it is scaled. The noise might be caused by the switching of high current signals within the voltage inverter. The same noise is not seen in the DAQ box voltage, as this box is placed further away from the motor. The noise makes it difficult to accurately determine the settling time of the battery current. The time is found by close inspection of the graph.

Source of Error

The slip calculations depends on the accuracy of the velocity measurements described in A.2. The *Source of Error* section therefore applies to this test as well.

In test 1 the slip reaches a minimum value of -1.191 - see figure A.26. This is outside the defined limits of the slip calculations. The reason is that the negative torque applied by the PMSM forces the wheel to rotate in the direction opposite to driving. This should not occur in a well-working slip control system and thus is not accounted for in the slip calculation.

Conclusion

The test was concluded unsuccessful as the slip controller did not yield satisfactory slip responses. The slip did not settle at the reference value and the plots indicated instability - see figure A.26 and A.27. The controller output did not settle at a constant value but kept oscillating from its maximum to its minimum limit - see figure A.26 and A.28. It is concluded that a delay in the torque response and the CAN-bus communication is the reason for the unsatisfactory results.

In the first test the RSW was not lubricated, but the PMSM was able to deliver a torque large enough to force the slip above its reference value. In the graph of figure A.26 the slip measurements reaches values as high as 0.15 several times. Values which are significantly higher than the reference value of 0.05.

Test 2 uses a higher slip reference of 0.1 which still causes the slip response to become unstable - see figure

A.27. The amplitude of the response increases during the test - an indication that the controlled system is unstable.
To further investigate the cause of this response, the controller output reference torque and measured motor torque is plotted on top of the slip response for the same time period. The result is shown in figure A.28. It is noted from this plot that: The measured motor torque is significantly delayed and therefore the actual motor torque could also be delayed. This claim is strengthened by the fact that the slip response follows the measured torque and not the torque reference.

Test 3 is carried out to investigate if the delay is caused by a propagation delay in the NI USB-6215. It is concluded that the response of the NI USB-6215 is satisfactory as the delay in the measurement corresponds to the time period between the output is demanded and measured - see figure A.29.
The plot in figure A.29 indicates that each CAN message is received twice. This is confirmed by inspection of data from the other tests. After consulting the Sevcon support team it is informed that the lower limit of the synchronization time of the Gen4 controller is 20 [ms] (twice the sampling time of the LabVIEW program used for data acquisition). The synchronization time was set to 10 [ms] using DVT, i.e. outside the limits supported by the motor controller. Therefore the controller software has changed the synchronization time to its lower limit without any notification.

As the reason for the delay cannot be concluded to be caused by a propagation delay in the NI USB-6215 test 4 is carried out to investigate if there is a delay between the throttle voltage from the NI USB-6215 and the battery current response to the motor controller. In this test the throttle voltage from the NI USB-6215 and the battery current is plotted and a delay between the two responses of approximately 58 [ms] is observed. This is followed by a settling time of approximately 100 [ms] which is significantly higher than the theoretical settling time of 8.8 [ms] of the current loop - see Section 3.3. The increased settling time might be caused by internal rate limits in the Gen4 controller.
The current through one of the motor phases is measured as well, indicating the same 58 [ms] delay. The settling time was not successfully determined from the noisy AC phase current signal.
After conversation with the Sevcon support team, the 58 [ms] delay is concluded to be caused by the internal error checking software of the Gen4 controller. The cause of the remaining delay of approximately 180 [ms] has not been determined.

The software responsible for the 58 [ms] delay can be bypassed by configuring the Gen4 controller as a pure slave motor which might decrease this delay. This involves error and rate limit checking in the master software (the LabVIEW-program) instead of the on board software of the Gen4 controller. Furthermore, the communication between the LabVIEW-program and the Gen4 controller increases in complexity as a series of CAN-messages must be supplied to the Gen4 controller continuously in order to monitor and control it as a slave.

It has not been possible to successfully configure and control the Gen4 controller as a slave during the test period, and the delay has therefore not been reduced.

Finally to illustrated that the 240 [ms] delay is the cause of the slip response oscillations a test model is designed. The model is build in the MATLAB Simulink environment. It is based on the simplified dynamic equations of the vehicle described in Appendix A.1 equation (A.2). The simulated response of this model with and without the torque delay is shown in figure A.31. The controller parameters have been chosen as in test 2. The simulation uses the Burckhardt Tire model for a road surface covered with snow to emulate the tire-tire friction when silicone is applied.

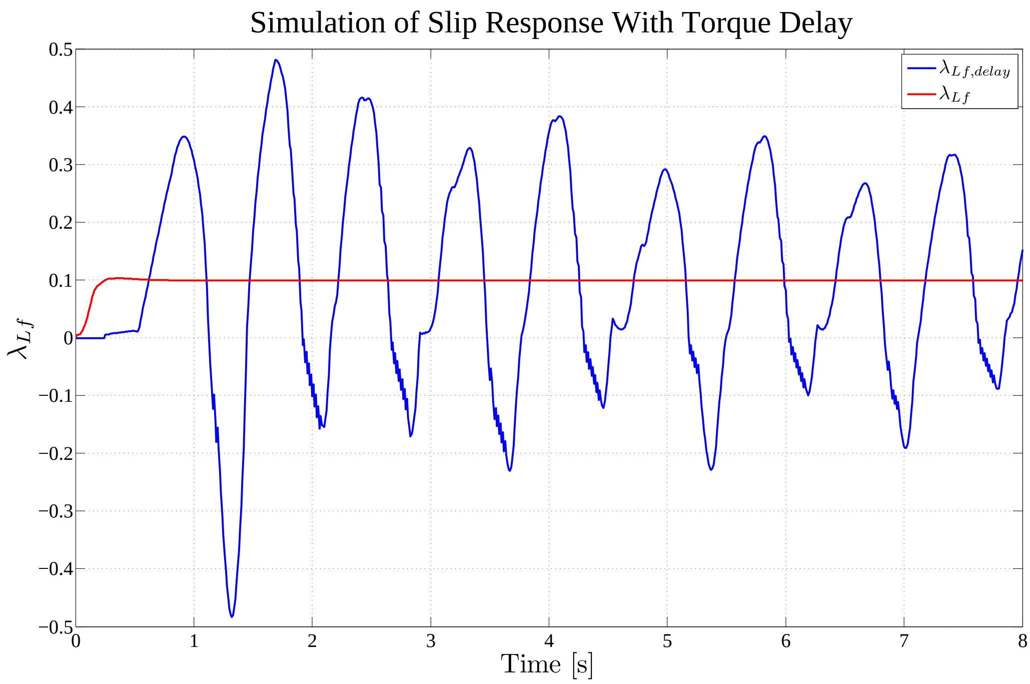

Figure A.31: Simulated slip response of the test system with (blue) and without (red) delay in torque demand.

As the figure shows, the response oscillates significantly as it was seen in test. The response without delay settles at the reference value indicating that the controller will stabilize the system without this delay.

B LabVIEW Code

This appendix presents a brief description of the LabVIEW program used in the tests described in Appendix A. The program communicates with the Gen4 motor controller via CAN-bus and is used to acquire and log data. The program also implements the slip controller described in Section 5.2, the friction force observer described in Section 5.4 and the friction curve estimator described in Section 5.5. The LabVIEW program can be found on the attached CD (see Appendix C).

B.1 Dataflow

The overall dataflow of the program is illustrated in figure B.1. A combination of parallel and sequential programming is utilized as the graphical programming interface of LabVIEW allows both. The data flow within the program is illustrated by black arrows while external inputs and outputs are illustrated by red arrows in figure B.1.
When the program is initiated all necessary parameters are updated, the motor controller is set in neutral and 0 $[V]$ is applied at the throttle input terminals (corresponding to zero torque). After the initialization two timed loops are run in parallel every 10 $[ms]$ until the user terminates them from the user interface (called the *Front Panel* - see figure B.2) or if an error has occurred in the CAN-bus communication. The loop in the left side of the figure uses frequency measures of the pulse train from the RSW encoder to calculate the tangential velocity of the RSW ($\dot{x}$). The loop in the right side steps through the following sequence:

0: Obtain angular velocity and torque measurements from a a CAN PDO message (see Appendix A.1) from the Gen4 controller.
Read analog throttle voltage (this is only used to check the response time of the USB-6215 box (see Appendix A.5).

1: Calculate slip and estimate the instantaneous friction force and friction coefficient using the friction force observer described in Section 5.4.

2: Estimate the friction curve and the slip corresponding to maximum traction using the friction curve estimator described in Section 5.5.

3: Calculate the slip controller output u.

4: Apply analog voltage to the throttle input of the Gen4 controller and apply digital output voltage to direction switch.

5: Update data array.

After the loops are terminated the motor controller is set in neutral again, 0 $[V]$ is applied at the controller throttle input terminals and the logged data is written to a spreadsheet file.

B.1 Dataflow

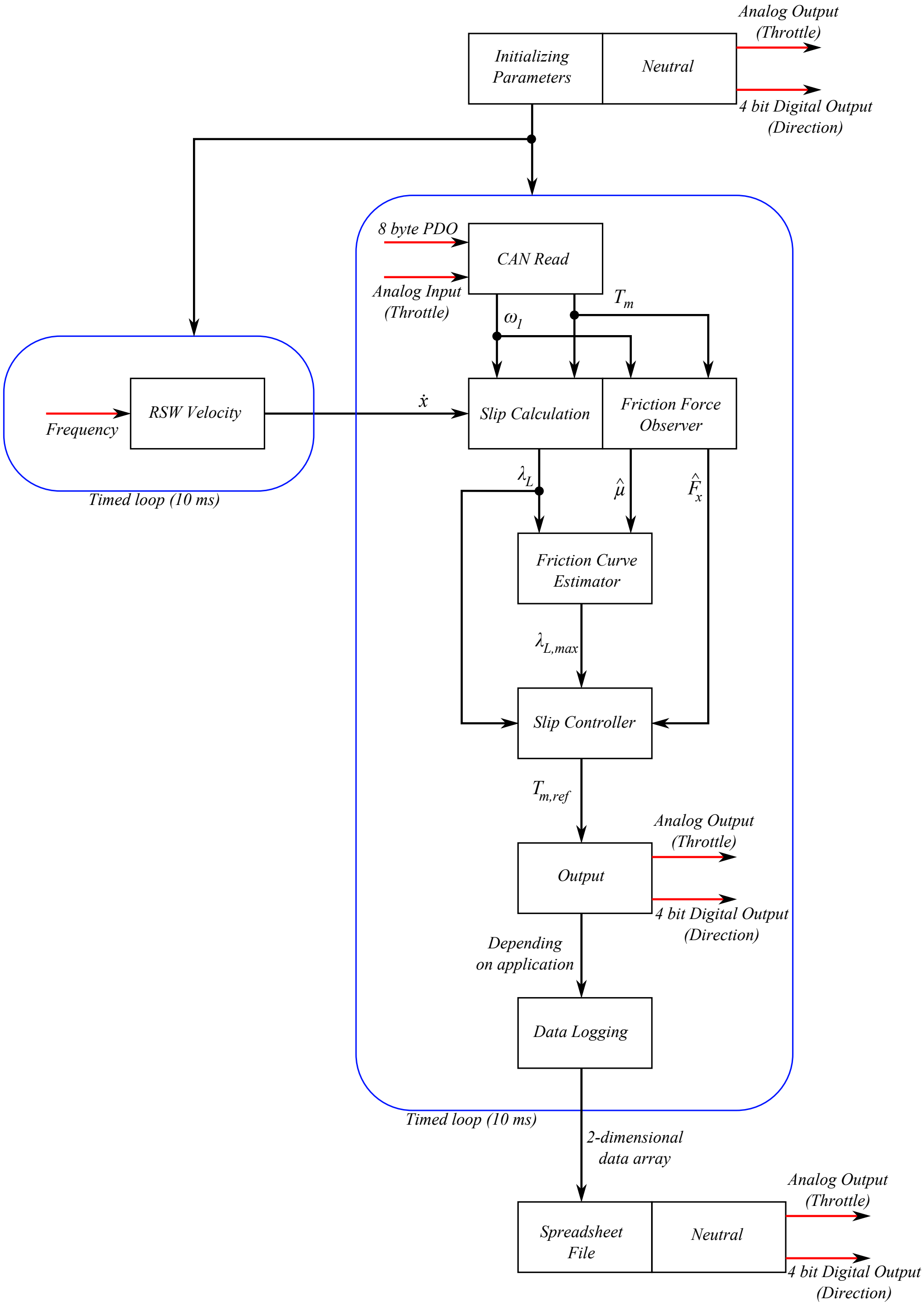

Figure B.1: Illustration of the dataflow in the LabVIEW program.

The reason for running the two loops in parallel is that the period of the pulse train from the RSW encoder is larger than the 10 $[ms]$ (the loop iteration period) at low speeds. The loop containing this measurement does not finish until a new measurement is detected but the previous value is stored as a local variable that can be accessed by the other loop. Thus, by running the loops in parallel, only the update of $\dot{x}$ is delayed (as no new measurement is available) and the delay is not passed on through the sequence described above.

B.2 Front Panel

The front panel seen in figure B.2 acts as a user interface where parameters can be adjusted and the system can be controlled and monitored. Different options can also be chosen from the front panel, i.e. whether the torque should be controlled manually (which is used in some of the tests) or by the slip controller.

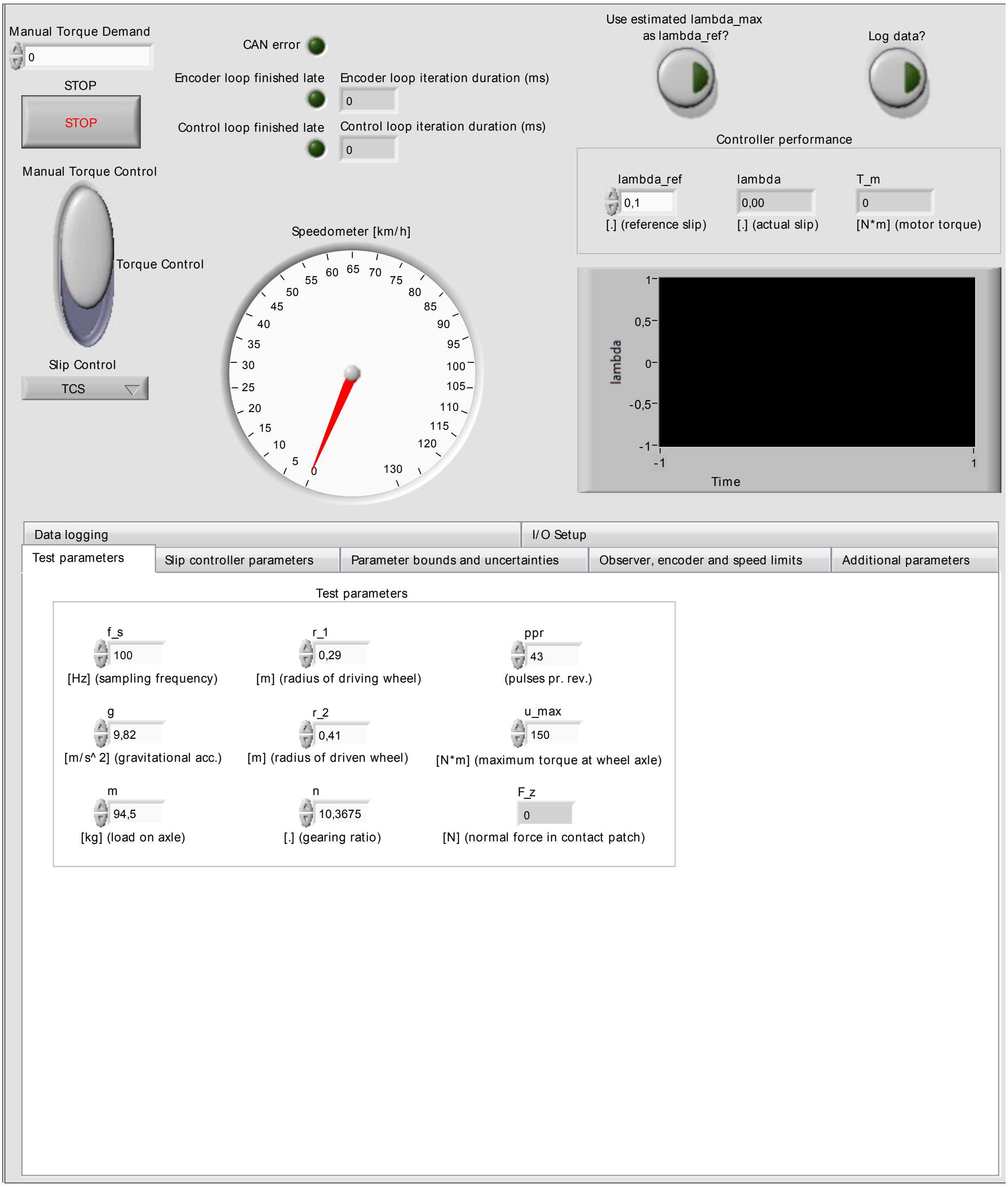

Figure B.2: Screenshot of the front panel of the LabVIEW program.

B.2 Front Panel

C Contents of CD

A CD is included with this report. The contents of the CD is listed below. Every item in the list is the name of a folder with the described content.

1. *Report* - Electronic version of the rapport.
2. *Models* - MATLAB Simulink models of QBEAK dynamics and test system dynamics.
3. *Program* - The Labview program used to log data and communicate with Gen4 motor controller during tests in the laboratories of ECOmove.
4. *Test data* - Logged data from the tests described in Appendix A.
5. *Datasheets* - Documentation of the components described in the report and used during the tests described in Appendix A.
6. *References* - Literature used. Confidential documents and copyrighted material is not included.
7. *Pictures* - Pictures of the test setup.